Molecular growth mechanisms in para-sexiphenyl thin film deposition

by
Dipl.-Ing. Gregor Hlawacek
submitted in fulfillment of the requirements for the degree of
Doktor der montanistischen Wissenschaften
at the Institute of Physics
University of Leoben, Austria

under supervision of
Ao. Univ. Prof. Dr. Christian Teichert

refereed by
Ao. Univ. Prof. Dr. Christian Teichert
and
O. Univ. Prof. Dr. Sedar Sariciftci

for Sophie

Eidesstattliche Erklärung

Abstract

Organic semiconductors based on small conjugated molecules show a high potential for applications in organic light emitting diodes, organic solar cells, and organic thin film transistors. Here, growth morphologies of crystalline para-sexiphenyl (6P) thin films on TiO_2(110)-(1x1), mica(001), Au(111), and SiO_2 have been investigated by Atomic-Force Microscopy (AFM). For TiO_2 a delicate balance between sticking anisotropy and diffusion anisotropy is the reason for the formation of parallel needles at room temperature as well as anisotropic stripes of upright standing molecules in the first monolayer at higher temperatures. On the mica surface, deposition of a layer of carbon or ion bombardment prior to 6P growth changes the orientation of the molecules from lying to upright standing and isotropic islands are formed instead of anisotropic chains of crystallites. The observed mound formation in the growth of upright standing molecules can be explained by the Zeno-Effect that requires a high Ehrlich-Schwöbel Barrier (ESB). For the first time in organic thin film growth, this barrier has been experimentally determined (0.67 eV) and verified for 6P films on SiO_2. In addition, we could also demonstrate that substrate induced changes in the molecular orientation in the first few monolayers lead to a layer dependent ESB, a novel phenomenon characteristic for the growth of anisotropic molecules.

Abstract

Zusammenfassung

Organische Halbleiter aus kleinen konjugierten Molekülen zeigen großes Potential im Bereich der organischen Solarzellen, organischen Leuchtdioden und organischen Dünnfilmtransistoren. Das Wachstum von kristallinem para-Sexiphenyl (6P) wurde mittels Rasterkraftmikroskopie auf $TiO_2(110)$-(1x1), Glimmer(001), SiO_2 und Gold(111) untersucht. Die parallelen Nadeln aus liegenden Molekülen auf TiO_2 sind das Resultat eines empfindlichen Gleichgewichts zwischen anisotroper Oberflächendiffusion und Haftanisotropie. Die Änderung dieses Gleichgewichtes mit steigender Temperatur führt zur Bildung von anisotropen Streifen aus stehenden Molekülen. Das Aufdampfen einer Kohlenstoffschicht oder das bombardieren mit Ionen von Glimmer vor der eigentlichen 6P Deposition führt zu isotropen Schichten aus stehenden Molekülen im Gegensatz zu den üblichen Strukturen aus liegenden Molekülen. Die beobachtete Hügelbildung in Schichten aus stehenden Molekülen kann mit dem Zeno-Effekt, der eine hohe Ehrlich-Schwöbel Barriere (ESB) voraussetzt, erklärt werden. Diese Barriere wurde zum ersten Mal für das Wachstum von organischen Halbleiterdünnschichten aus experimentellen Daten berechnet (0.67eV) und für 6P Filme auf SiO_2 bestätigt. Weiters konnte gezeigt werden, dass es durch eine substratinduzierte Reorientierung der Moleküle in den ersten Moleküllagen zu einer lagenabhängigen Höhe der ESB kommt. Dieses neuartige Phänomen ist charakteristisch für das Wachstum anisotroper Moleküle.

Zusammenfassung

Contents

1 Motivation and Introduction

1.1 Organic Semiconductors

1.1.1 Introduction

Organic Semiconductors cover a wide field of different classes of chemical compounds. The ones most promising for specific applications are charge transfer compounds, conductive polymers, and small aromatic molecules.

A prominent member of the charge transfer compounds are so called Bechgaard salts. They have shown superconducting properties already more than 25 years ago. The first synthesized organic superconductor that could work at ambient pressures was $(TMTSF)_2ClO_4$ and had a critical temperature of 1.4 K [1]. The group of charge transfer salts based on the donator Bisethylendithiolotetrathiofulvalen (BEDT-TTF or ET) could reach values as high as 11.6 K [2].

The biggest market for organic semiconductors is the electronics. Products such as displays, Radio Frequency Identification Tags (RFID), and solar cells based on organic semiconductors are already available on the market. They have either conductive polymers or small organic molecules as active layer.

Organic electronics based on conductive polymers have the big advantage that they are good candidates for solution processing. This can be done by screen printing [3], soft lithographic stamping [4], inkjet printing [5,6] or other methods. The use of these production techniques allows role to role fabrication of devices at extremely low costs. However, the main issue with organic semiconductors but especially conductive polymers is their low charge carrier mobility. So far electronic circuits based on polymers have shown only charge carrier mobilities of up to 0.1 $cm^2V^{-1}s^{-1}$

Our interest will be focused on so called small molecule organic semiconductors. In general, they have an extended delocalized π system that stretches across the whole molecule. They are often formed by a number of phenyl rings (<10) that share a common π system. Small molecules organic semiconductors will be described in more details in the next section.

The common feature in all these materials is the existence of so called π electrons. The main building block is carbon, which is sometimes replaced by very low quantities of nitrogen, sulfur, or oxygen. The important physics results mostly from the carbon atoms forming the backbone of these structures. The electron configuration of a free carbon atom is $1s^22s^22p^2$. However, in the bound state the configuration is changed to $1s^22s2p^3$. A double bond between two carbon atoms is formed by a so called sp^2-hybridization. This hybridization is formed by one s and two p orbitals. There are three

1

degenerate sp^2 orbitals. These three orbitals all lie in one plane and are separated by 120°. The left over p$_z$ orbital is unchanged and sticks vertically out of this plane on both sides. For a double bond two of the degenerate orbitals – one from each atom – form a σ bond. The second bond is formed between the p$_z$ orbitals of the two atoms. This is is the so called π bond. Figure 1.1 displays the situation.

While the two electrons forming the σ bond are localized between the two carbon atoms the electrons forming the much weaker π bond are delocalized above and below the plane of the sp^2-hybridization. The electronic and optical properties of these materials are defined by this π bond. The energy to excite the involved electrons is only a few eV. As a result, these molecules luminesce and absorb in the near UV to infrared. For a molecule, these delocalized states can stretch over several atoms. The most common and representative is benzene. The p$_z$ orbitals of all six carbon atoms are delocalized across the aromatic plane and form a ring of high electron density. However, with increasing size of the delocalized electron system the electronic excitation energy gets smaller.

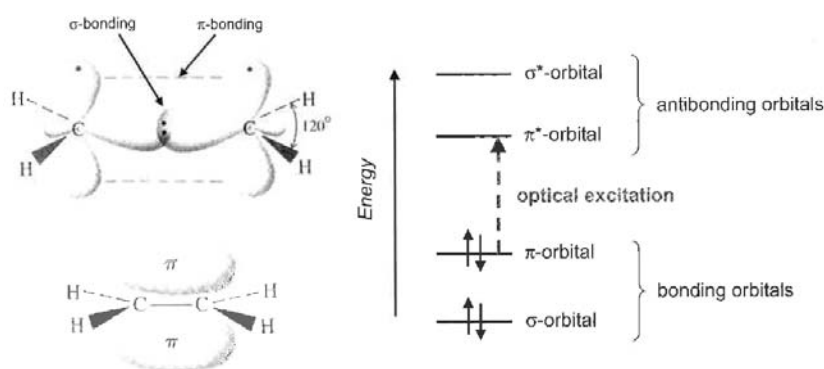The valence and conduction band in inorganic semiconductors correspond to the

Figure 1.1: Left: σ and π orbitals in a C=C bond. The scheme on the right displays the lowest electronic excitation between the bonding and the antibonding π orbitals (taken from [7])
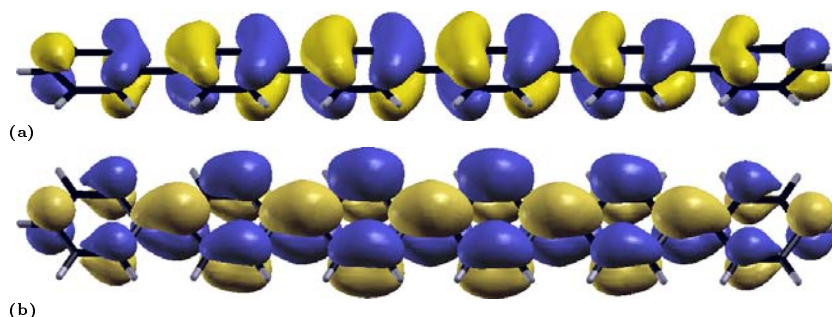.

Figure 1.2: (a) HOMO and (b) LUMO of para-sexiphenyl. The color scale denotes the phase of the wavefunction. (courtesy of P.Puschnig).

highest occupied molecular orbital (HOMO) and the lowest unoccupied molecular orbital (LUMO) in organic semiconductors. Their position and orientation is defining the properties of the resulting organic crystal. However, exact determination although possible [8] is often difficult and mostly done by modeling. The intermolecular forces forming such crystals are small compared to the intramolecular forces. The important thing is that the strength and orientation of these intermolecular forces are also defined by the outermost and weakly bound π electrons. Figure 1.2 shows the HOMO and LUMO for para-sexiphenyl.

1.1.2 Small Molecule organic semiconductors

As already mentioned common building blocks in organic semiconductors are phenyl rings. The building block is a ring of 6 carbon atoms also known as benzene. The physical properties, of course, depend on the number of building blocks. A widely used group is the acene series. For oligoacenes this is presented in table 1.1 for the correlation between molecules length and maximum of absorption. With increasing chain length and size of the delocalized π system the maximum absorption wavelength increases and the energy difference between the HOMO and the LUMO gets smaller.

Other common molecules include but are not limited to metal free (H-Pc) and metal substituted phthalocyanins (e.g. Cu-Pc), tris(8-hydroxyquinoline)aluminium (Alq$_3$), sexithiophene (6T). In this work we will use para-sexiphenyl (6P), a oligophenyl molecule. In contrast to polymers these materials often require high vacuum conditions for processing because they are not soluble.

Both polymers as well as small organic molecules are most commonly used in an organic light emitting diode (OLED) or an organic thin film transistor (OTFT). When growing such structures from small organic molecules the molecular orientation plays an important role. Many of these molecules are one- or two-dimensional or anisotropic

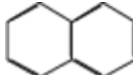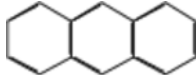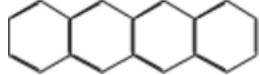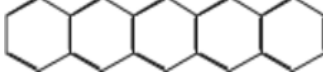| Name	Structure	Absorption Maximum
Benzene		255 nm
Naphthalene		315 nm
Anthracene		380 nm
Tetracene		480 nm
Pentacene		580 nm

Table 1.1: Molecular structure and absorption maximum of the first 5 oligoacenes (from [9]).

in some other way. This leads to the fact that electronic transport in organic semiconductors is highly anisotropic. Many 1D molecules like 5P, 6T and 6P form herringbone layers of close packed molecules. The overlap between the orbitals of the molecules in the layer is sufficient to allow a good electronic transport. However, vertical to the layer plane, the overlap of the electron density is rather small and the mobility in this direction is drastically reduced. When building optical devices one must also pay attention to the fact that the emitted light is not only polarized but also oriented in a direction perpendicular to the molecular plane. Considering these particularities one can define an optimum orientation for the molecules in these devices. Figure 1.3 depicts the two solutions. For an OLED the preferred orientation of the molecules is flat lying. This allows good electronic transport from the back electrode towards the top electrode. The light which is emitted from the molecules is also directed perpendicular to the electrodes and can leave the device at the transparent top electrode. For an OTFT electronic transport occurs parallel to the gate or the substrate. Therefore, the molecules should be oriented as upright as possible. Recent investigations showed that also within the a-b plane where the molecules have a high orbital overlap an anisotropy exists. For Rubrene the mobility changes by a factor of four between the a and the b axis [10].

1.1.3 para-Sexiphenyl

Oligophenyls (nPs) are prototype model systems for linear π conjugated organic semiconductors. Their band gap can be controlled by adding or removing phenyl units from the chain [11] and ranges from 2.5 eV for poly-paraphenyl (PPP) to 3.1 eV for para-sexiphenyl (6P), to 5.1 eV for biphenyl [12, 13]. With exception to the polymer species PPP, they are evaporable under UHV conditions and are emissive depending on their band gap in the blue or UV-vis spectral region. A variety of nPs can be bought from stock their names reflect the number of phenyl rings in the backbone. Widely used are biphenyl (2P), para-terphenyl (3P), para-quaterphenyl (4P), para-quinquephenyl (5P), para-sexiphenyl (6P) and para-heptaphenyl (7P). All of them form ordered crystallites and show a high degree of anisotropy (depending on the chain length of course) in their optical and electrical properties [14–16]. Their electro- and photoluminescence
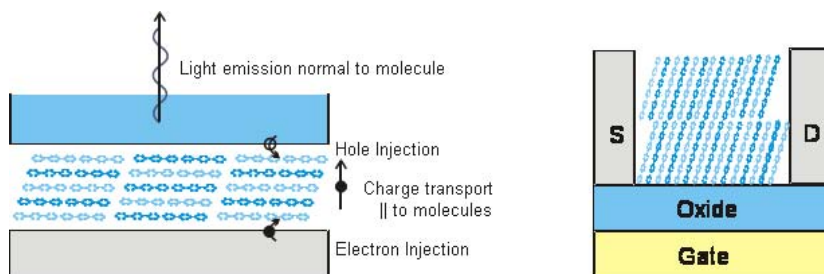

Figure 1.3: Desired molecular orientation in an OLED (left) and an OTFT (right) (courtesy of M. Ramsey).

4

yields are large enough to be used in applications. The electroluminescence light is polarized [17] and they are candidates for wave guiding [15, 18] as well as lasing [19]. Para-sexiphenyl has shown an exceptional high mobility of up to $14\,\mathrm{cm}^2/\mathrm{Vs}$ [20].

1.2 Epitaxial Growth Mechanisms

The things discussed in the preceding sections are related to organic semiconductors. Other important facts controlling the performance of electronic and optoelectronic devices are already well known from inorganic semiconductor growth. However, not always methods and ideas established in inorganic semiconductor growth can be transfered one to one to organic thin film growth. A few examples will be discussed below.

Smooth films are desirable because a rough interface between two different layers in a device will scatter electrons and therefore reduce the device performance. In inorganic thin film growth this gets even more important as the electronic transport is restricted to the first few (even one or two) monolayers. Defects that occur in the first layer will greatly hinder electronic transport as the electrons can not sidestep into higher layers due to the restricted penetration depth of the electric field from the gate.

Diffusion in inorganic semiconductors usually deals with 0-dimensional particles that might diffuse on an anisotropic substrate. However, in our case also the diffusing particles are anisotropic. This has to be considered when growing on oriented surface, because molecules will not only diffuse in one direction but also arrive with a specific orientation.

Sticking can therefore be highly anisotropic. As already discussed many of the anisotropic molecules also show very different terminations of their crystallographic planes. In combination with a diffusion anisotropy this can lead to highly anisotropic morphologies. These morphologies can be desired and for example used as waveguides [18, 21] but will be unwanted in the general case.

In the following sections the fundamentals of thin film growth will be discussed. However, this will be far from complete and concentrate on the parts necessary for the further discussion. For a general overview of thin film growth [22, 23] are a good starting point. A review on organic thin film growth covering many different materials can be found in [7] or [24].

1.2.1 Thermodynamics

This section treats the formation of a nucleus and the subsequent epitaxial growth of the film as a pure thermodynamic process. This classic approach can explain a number of growth morphologies and process often found in crystal growth. It is however limited by the fact that it can only describe processes that happen in or near the thermal equilibrium. In other words temperature, and pressure (which corresponds to flux in

Molecular Beam Epitaxy (MBE)) must be constant and close to the values necessary for the phase transition.

Nucleation

In a homogeneous system near the phase equilibrium between two phases, small fluctuations that are always present will lead to the formation of an aggregate of phase B in phase A. If the chemical potential μ_B is smaller than the initial one, the work of formation of a cluster can be expressed in terms of Gibbs free energy as

$$\Delta G(r) = -\frac{4\pi r^3}{3v_l}\Delta\mu + 4\pi r^2\sigma \tag{1.1}$$

where $\Delta\mu = \mu_A - \mu_B$ is the supersaturation, v_l is the molecular volume of phase B and σ is the surface free energy of the formed cluster. The nucleus will be stable if its size exceeds the critical radius

$$r^* = \frac{2\sigma v_1}{\Delta\mu}. \tag{1.2}$$

If $r \geq r^*$ the energy gain from creating a volume of phase B will be higher as the energy loss due to the creation of an interface between phase A and B. As a consequence, if the formed nucleus is smaller than r^* it will disappear again while a nucleus that is larger than r^* will continue to grow.

This balance can be influenced by additional adsorbed species that are present during growth but not incorporated into the film — so called surfactants. Their influence was initially found by the fact that a bad vacuum sometimes leads to smoother films [25]. Depending on the efficiency of a surfactant the size of the critical nucleus can be increased or – the more desirable case – decreased [23].

However, the more common and for epitaxy also more relevant situation is the heterogeneous nucleation. Here, phase B is formed out of phase A of material 1 (film) in the presence of material 2 (substrate). On an unstructured surface (ignoring effects like strain that would arise from a more realistic substrate) the work of formation will always be smaller or equal to the one necessary in homogeneous nucleation.

Thin film growth

If a nucleus has already formed the film still has to grow. A classical purely thermodynamic description for this is given in this section.

When ever particles are deposited onto a surface this changes the chemical potential

$$\mu = \frac{dG}{dn} \tag{1.3}$$

of that surface. μ is defined by the change of the Gibbs free energy G when n uniform layers are adsorbed. An other important thing to remember is the fact that for a stable situation on a surface the surface free energies of the involved interfaces must be minimum.

The change of the surface free energy

$$\Delta\sigma = \sigma + \sigma_i - \sigma_s \qquad (1.4)$$

will be $\Delta\sigma < 0$ if $d\mu/dn > 0$ [23]. In other words, if the sum of the surface free energy σ_i between substrate and adsorbate, and σ, between adsorbate and vapor, is smaller than the surface free energy of the substrate σ_s wetting will occur.

Three principle situations can be thought of

1. $\Delta\sigma < 0$ for all times. This means it is feasible for the substrate to cover itself with the adsorbate and a film of uniform thickness will grow.

2. $\Delta\sigma < 0$ for small n but $\Delta\sigma > 0$ for large n. The adsorbate film will start to cluster after a thin uniform film has grown.

3. $\Delta\sigma > 0$ for all times and clustering will occur immediately.

This situations correspond to growth mechanisms well known in literature namely Frank-van der Merwe (FM) also called layer by layer growth or two dimensional growth, Stranski-Krastanov (SK) or layer plus island growth, and Vollmer-Weber (VW) growth also called island growth or three dimensional growth. Figure 1.4 shows the resulting morphologies for all three situations. In a real system the situation is more complex due to the fact that the lattice parameters of the substrate and those of the film might differ. This will change the value of σ_i and depending on the actual size of the lattice mismatch it will lead to the formation of dislocations. Lattice mismatch is of special importance for the SK growth mode. However, although mathematical accurate neither the surface free energy σ nor the chemical potential of uniform film of adsorbate is usually known or if known accurate enough. A more practical way of making predictions on the expected growth mode using the enthalpy of evaporation and the desorption energies is given in [23] in chapter 4.3.4.4.
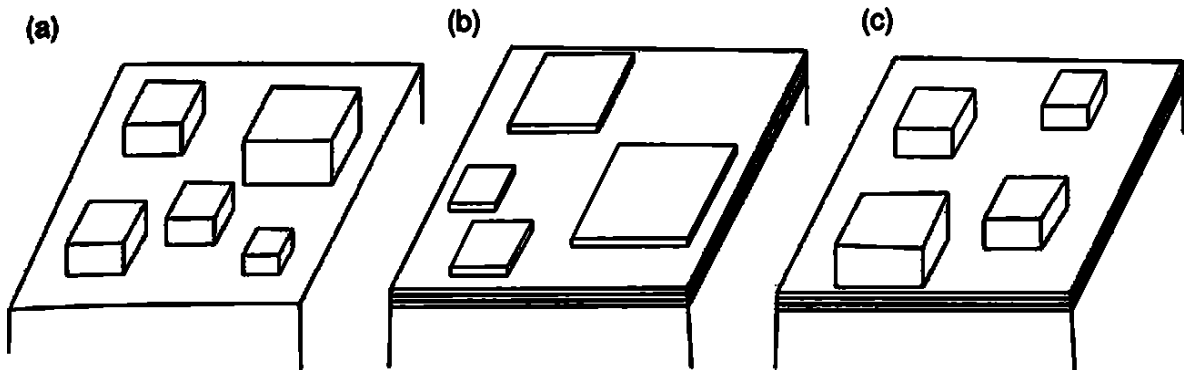

Figure 1.4: Schematic morphology for (a) Volmer-Weber, (b) Frank-van der Merwe, and (c) Stranski-Krastanov growth modes.(from [26])

1.2.2 Kinetic considerations

The situation for nucleation and film formation gets more complex if kinetics of surface diffusion is taken into account. Thermodynamics also includes diffusion. However, all mechanisms are activated thus the resulting morphology wins that leads to the lowest surface energy. This is independent of the actual pathway. Only the starting and the end point are of importance. In a kinetic description the energy of an intermediate step will also be considered. Diffusion is highly sensitive to changes in temperature and will therefore dramatically change the situation described by only a thermodynamic approach. An atomistic view of the processes involved in nucleation as well as thin film growth is necessary to describe and understand the involved processes. Figure 1.5a depicts some of the possible processes. Of special importance for the further discussion will be the incoming flux of atoms F and the two displayed hopping processes on the terrace h and onto the lower terrace h'.

Special attention has to be paid to the way particles are incorporated into already existing features. Figure 1.5b displays the most important lattice sites that can be found in a growing thin film.

Adatoms are found on the surface and can diffuse freely. Their movement is controlled by the intra layer hopping rate ν and the diffusion constant D.

Two dimensional islands of atoms are formed whenever two or more atoms meet on a terrace and create a bond. These clusters can be either mobile or immobile. These clusters have a lifetime that will depend on their size. For our considerations we

(a)   (b)
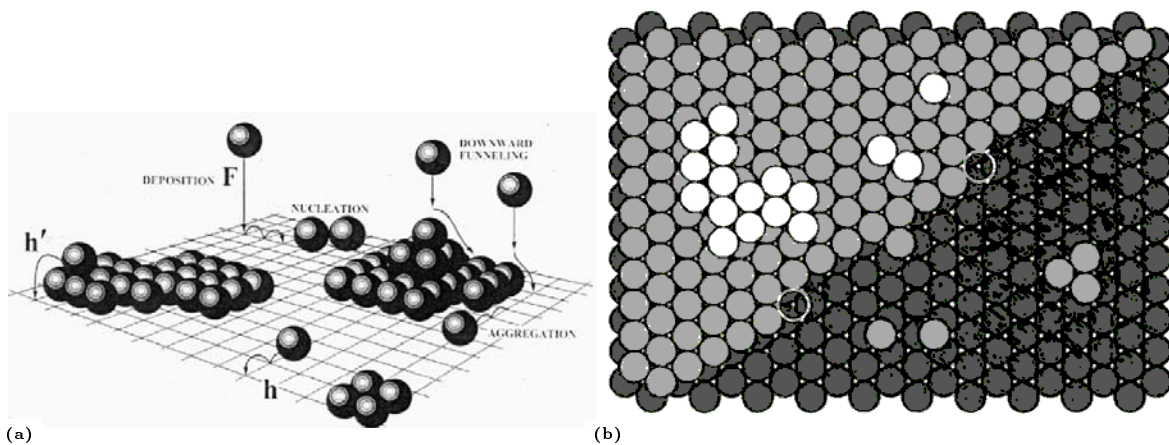
Figure 1.5: (a) Atomistic processes involved in nucleation and formation of layers in thin film growth (from [27]). (b) Lattice sites on the surface of special interest including kink sites (white circle), edge sites, cluster of $i^* = 1$ and $i^* = 2$ adatoms and a second layer (white balls) island. Dark grey balls are used for the substrate (or any other complete layer) and light gray balls for the first incomplete layer (from [28]).

will only distinguish between stable and immobile clusters (formed by more than i^* particles) and those who are not stable (formed by i^* or less particles).

Edge sites are metastable. If an atom is attached to the edge of an terrace it can stay there for a while. However, the chemical potential although lower than in the gas phase will still be higher than that of the bulk. Most likely edge atoms will either detach or move along the edge.

Kink positions or half crystal positions are the work horses of thin film growth. Binding an atom to a kink position will not remove the kink but advance the kink one step along the edge. The chemical potential of the crystal phase is defined by these sites and the actual thin film growth happens in this position. The importance of the half crystal position was already found by Kossel in 1927.

Stable two dimensional clusters are formed from stable clusters. They grow by adding atoms to their kink positions. At which time they form with respect to the completion of the underlying layer is important for the final growth morphology and controlled by the kinetics of the diffusion processes on the terrace (related to cluster formation) and interlayer transport of atoms across the terrace edge. With ongoing deposition they grow in size and start to coalesce, closing the void between them. When all gaps are closed the layer is closed.

The related processes happen at very short time intervals (some ps), so a direct experimental observation is difficult. However, Kinetic-Monte-Carlo simulations [29–31] allow the calculation of the energies involved in detachment/attachment process as well as diffusion on the terrace or over the terrace edge. For a detailed description one has to pay attention to the delicate balance between different pathways for diffusion especially over the terrace edge as the lowest energy path will be the one defining the resulting growth morphology [32].

Again attention has to be paid to the absence or presence of surfactants as they also will influence kinetic aspects of growth, and are not always added intentionally and are then called contamination. Therefore, even if no surfactants are used it is critical to specify and control the vacuum conditions in thin film growth.

Two-dimensional nucleation

Experimental result show that the critical nucleus size in thin film growth is so small (less than 5 particles) that we cannot say if such a nucleus is solid or liquid as no long range order can be observed. Therefore, the thermodynamic approach presented above fails. An atomistic view of nucleation is necessary in order to understand the processes involved. One of the practical results of an atomistic nucleation theory is the following scaling law [33, 34]

$$N \approx \left(\frac{F}{\nu} \right)^{\frac{i^*}{d(i^*+2)}} \tag{1.5}$$

that relates the nucleation density N to the ratio of the flux of incoming particles F and the mobility ν. d is 2 for a two-dimensional diffusion process. This approach is correct under the hypothesis that the smallest stable cluster is formed by two particles ($i^* = 1$) and the islands are not fractal. Furthermore, it is only valid in an initial low coverage regime and completely neglects coalescence of islands [28].

If a barrier exists that controls hopping from a terrace down to a lower terrace this will influence the nucleation probability for the second layer islands. We can use [34]

$$f = 1 - e^{-\left(\frac{L}{L_c}\right)^{k+2}} \tag{1.6}$$

to describe the number fraction of islands that have nucleated a second layer island on top f with the island size L and a critical island size

$$L_c = \left(\frac{7\nu'}{2\alpha^4 F N}\right)^{\frac{1}{7}}. \tag{1.7}$$

For the considered case were an additional energy barrier exists that is larger than $k_B T$, $k = i^* + 4$ [35]. ν' is the rate at which an atom would jump over the edge. $\alpha = A/L^2$ accounts for the fractal shape of the island and is given by the area A and the perimeter length L. Here, parameters like N, A, and L (and all other parameters that are related to a length) are measured in terms of the number of lattice sites. In the following, a lattice site will be assumed to be roughly 0.6 nm for an upright standing molecule.

Kinetic in thin film growth

As already mentioned in the previous section, a barrier might exist that controls adatom diffusion from one terrace onto the lower lying terrace. Such a barrier is normally referred to as Ehrlich-Schwöbel-Barrier (ESB) and was first found by Ehrlich and Hudda in 1966 [36]. The situation is shown in figure 1.6. While for intra layer diffusion only a small energy barrier E_{sd} must be overcome, the barrier for a jump over the edge E_S can be much higher. The difference $E_{ES} = E_S - E_{sd}$ gives the ESB. In contrast to this situation, the presence of a small amount of a second species of adatoms that influence the surface free energy (generally called surfactants) can turn the ESB negative and can introduce an additional barrier for particles moving to the upper terrace. This will result in a promotion of layer-by-layer growth although thermodynamics would suggest a 3D island growth [23].

Assuming an infinitely high barrier, than, from the incoming flux of atoms, only the atoms landing on the terrace $h-1$ can be incorporated into the terrace h. The coverage Θ_h of the layer h therefore follows the linear equation

$$\frac{d\Theta_h}{dt} = F\left(\Theta_{h-1} - \Theta_h\right) \tag{1.8}$$

F is the incoming flux of particles. Solving this equation with $\Theta_{h=0} = 1$ and $\Theta_{h>0}(0) = 0$ gives
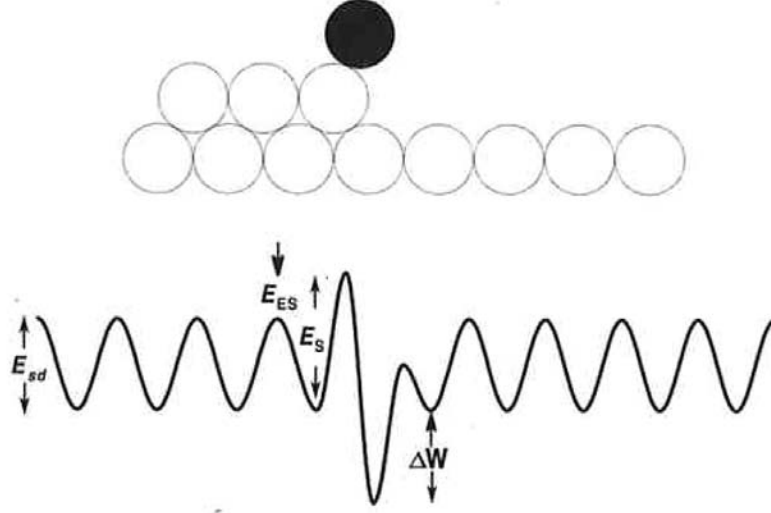
Figure 1.6: Sketch of an ad atom on a step edge and energy landscape it encounters. An additional energy barrier E_{ES} exists for a jump to the lower lying terrace. (adopted from [23])

$$\Theta_h(t) = 1 - e^{-\overline{h}} \sum_{n=0}^{h-1} \frac{\overline{h}^n}{n!} \tag{1.9}$$

with $\overline{h} = Ft$. Because $\Theta_1 = 1 - e^{-\overline{h}}$ will be smaller than 1 for all times the first layer never closes. This is the reason for the deep trenches.

We can see that equation 1.9 has the form of a Poisson distribution

$$f(n, h) = e^{-h} \frac{h^n}{n!}. \tag{1.10}$$

These Poisson shaped mounds were already found by Shea et al. using Auger electron spectroscopy [37]. In the presence of a significant barrier growth hillocks will form by repeated 2D nucleation since interlayer mass transport is hindered. This was observed in real space by Meinel et al. using a gold decoration method in Ag on Ag(111) homoepitaxy [38].

The final morphology will depend on the height of this barrier. This dependence of the final morphology on such a barrier was described by Elkinani and Villain in 1993 [39, 40]. They investigated the effect of an infinitely high step edge barrier on the shape of a growth mound. The resulting shape for their one dimensional simulations is shown in figure 1.7. The shape is characterized by deep trenches between the mounds and a pointed top part of the individual mounds. Also note the changing slope of the mound cross section. They used the Zeno Paradox to explain the theoretically found shape.
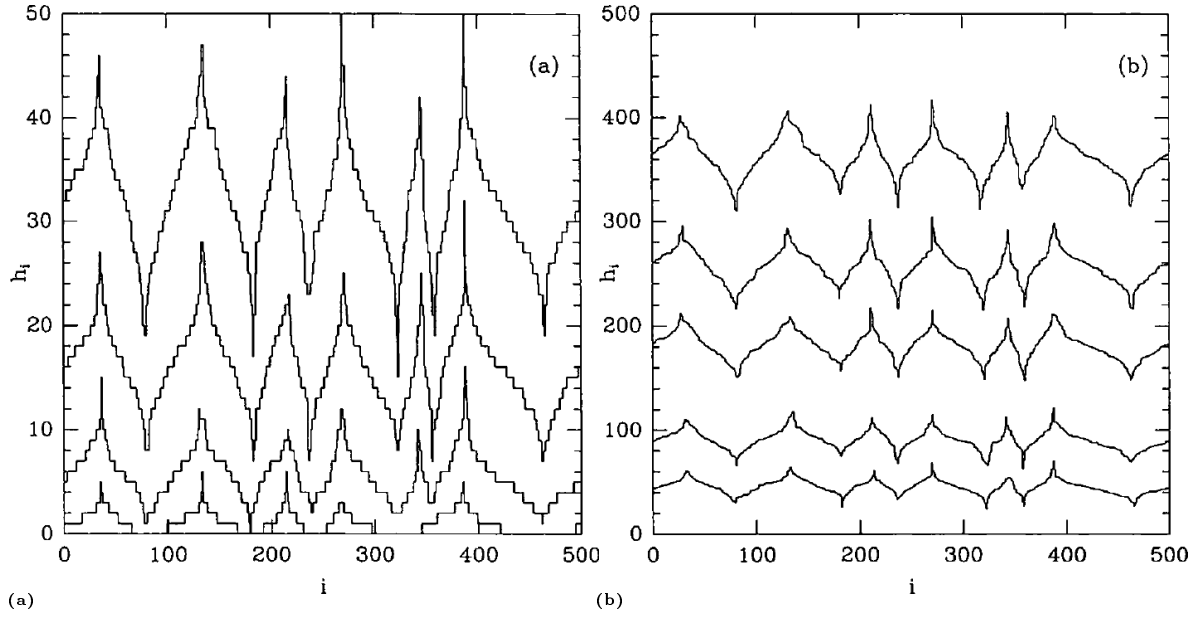
Figure 1.7: Theoretically found mound shape for growth without interlayer transport. (a) (from bottom to top) 1, 5.6, 16, and 32 monolayers (ML), and (b) after 45.25, 90.5, 181, 256, and 362 ML. Note the different height scales for the two diagrams (from [41]).

The Zeno Paradox, found by Greek philosophers, says that the incredible fast Achilles can never catch up with the tortoise, which is given a defined distance ahead. At the shoot of the start gun both start to run as fast as they can. After a short period of time Achilles reaches the point where the tortoise started. However, the tortoise has also made some way while Achilles tried to catch up. So Achilles has to overcome this additional distance just to find out that again the tortoise has moved a little further. It turns out that Achilles when ever he reaches the last position of the tortoise has to overcame an additional small piece of track. Although these pieces get shorter and shorter the tortoise will always be ahead.

In terms of a surface science context, the Zeno Paradox can be interpreted in the following way: The probability for an infinitely small particle to land in the narrow trench is extremely low. However, from time to time a particle will land there but not close the trench due to its infinitely small size. But it will reduce the chance for an other particle to land in the remaining trench. Similar to the distance between Achilles and the tortoise the trench will get smaller and smaller but it will never close completely.

A detailed look at the formation of such mounds reveals a number of interesting characteristics.

Equation (1.10) allows to calculate the uncovered surface of each terrace n for a given nominal film thickness h. However, to get the total area for each layer the cumulative distribution function

$$F(n,h) = \frac{\Gamma\left(\lfloor n+1,h \rfloor\right)}{\lfloor n \rfloor!} \tag{1.11}$$

has to be used. Here $\Gamma(x,y)$ is the incomplete gamma function. However, for most cases (1.11) can be estimated with

$$F(n,h) \approx e^{-h} \sum_1^n \frac{h^n}{n!}. \tag{1.12}$$

This is the sum for $n = 1$ to the given layer n of (1.10). The lower limit for the sum is set to 1 as the substrate gets the index 0.

The mean value of this distribution is $\overline{h}$. For a Poisson distribution the standard deviation is given by the square root of the mean value so that the roughness

$$\sigma = \left(\overline{h^2} - \overline{h}^2\right)^{1/2} \tag{1.13}$$

follows the simple equation

$$\sigma = \overline{h}^{1/2} \tag{1.14}$$

We ca follow the arguments given in [42] and [28] to actually calculate this barrier. The rate for a molecule to jump down over the terrace edge is

$$\nu' = C e^{-\frac{E_S}{k_b T}} = C e^{-\frac{E_{sd} + E_{ES}}{k_b T}}. \tag{1.15}$$

We assume that the prefactor C is constant for all situations. However, it has to be noted that this sometimes is not the case [43]. We can then write (1.15) as

$$\nu' \simeq e^{-\frac{E_{sd}}{k_b T}} e^{-\frac{E_{ES}}{k_b T}}. \tag{1.16}$$

The first term is equivalent to ν. Therefore we can rewrite (1.16) as

$$\nu' = P_s \nu. \tag{1.17}$$

with

$$P_s = e^{-\frac{E_{ES}}{k_B T}}. \tag{1.18}$$

For a film of several monolayers thickness which has obtained the above described mound shape the ratio between the average circumference of the top terrace $\langle L \rangle$ (that is a terrace to small to nucleate a further terrace) and the average circumference of its base terrace $\langle \Lambda \rangle$ is given by [34]

$$\langle \Lambda \rangle = \langle L \rangle * 2/3 \tag{1.19}$$

The size of the base terrace

$$\Lambda = 1.193\alpha^{-\frac{3}{5}} \left(\frac{\nu'}{F}\right)^{\frac{1}{5}} \tag{1.20}$$

then depends on the ratio between the jump rate over the edge and the flux of incoming particles [34]. Combining equations (1.7), (1.20), (1.17), and (1.18) finally gives the desired value ΔE_{ES}. This has been successfully used by Kalff and coworkers to explain the observed mound shape in Pt/Pt(111) homoepitaxy [44].

However, so far this model as well as most of all other growth models have not been adopted to the thin film growth of organic molecules. As will be shown later, the models can be used as they are to describe organic thin film growth in general but can not cover the details involved. The reason is given by the fact that the classical growth models simply ignore the more than zero dimensional nature of the building blocks in organic thin film growth. A *particle* is usually identical with an atom in in inorganic growth, while already the rather simple case of para-sexiphenyl would require at least a one-dimensional particle to describe the obviously more complicated situation when this molecule diffuses over a terrace edge. Other more complicated molecules will require a two- (Phtalocyanins, Porphyrines, and other) or even three-dimensional particle. It is the goal of this thesis to discuss some of the problems resulting from the higher dimensional nature of the building blocks.

2 Experimental

2.1 Para-sexiphenyl

In this work, 6P thin films are created on various substrates by means of different HV and UHV deposition methods. 6P consists of six phenyl rings that are connected in the para position with single bonds. Due to steric hindering between the hydrogen atoms the molecule is twisted in the gas phase. However, when incorporated in a crystal the energy gain is larger than the activation energy for turning all the rings in the energetically unfavored planar configuration [45]. Figure 2.1a shows a single 6P molecule in the planar configuration. The VdW dimension of a single 6P molecule is $0.35x0.67x2.85$ nm^3 [9].

At room temperature, 6P crystallizes monoclinic in the space group P2$_1$/c. The lattice constants of the unit cells are $a =$26.241 Å, $b =$5.568 Å, and $c =$8.091 Å. The monoclinic angle is $\beta =$98.17°. More properties are listed in table 2.1. From figure 2.1b one can see that in the unit cell the center molecules in each plane are turned with respect to the molecules on the corner sites. This results in the so called herringbone packing. Furthermore, one can see that the molecules are not parallel to the long axis but tilted which results in the fact that the molecules have a different tilt angle with respect to the substrate than the unit cell [46].

6P thin films have been investigated on various substrates including but not limited to mica [18, 47–50], Gold [51–54], TiO$_2$ [55, 56], aluminum [57–59], GaAs [60–62], KCl, indium tin oxide (ITO) as well as polymers and heterostrcutures with other organic semiconductors.

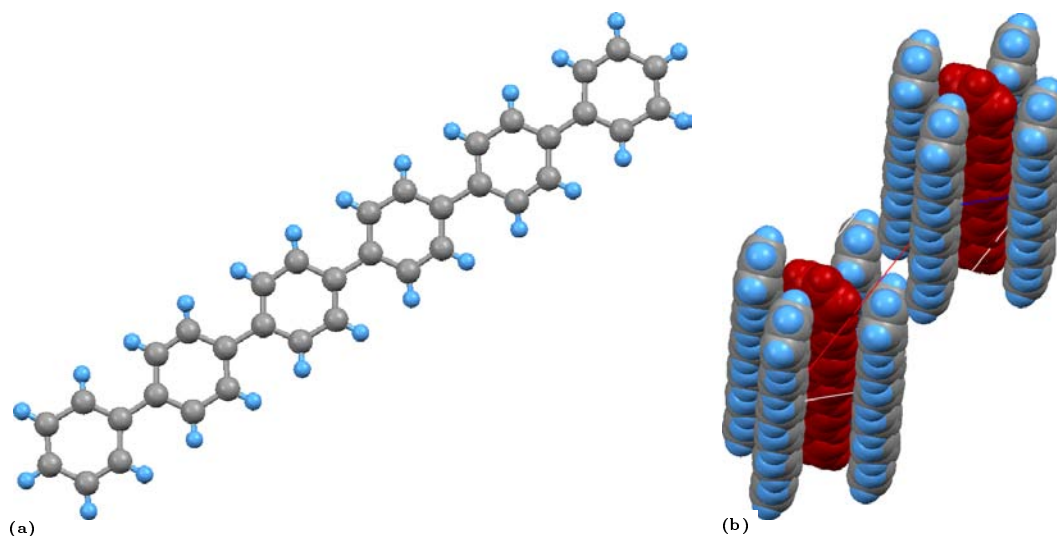| CAS Registry number	4499-83-6
Atomic mass	458.59 amu
Density	1.288 g/cm^3
Melting point	702 K-748 K
Desorption energy	2.0 eV-2.5 eV

Table 2.1: Properties of 6P (taken from [9]).

Figure 2.1: (a) single 6P molecule in the planer conformation as found in crystals. (b) 6P unit cell filled with 10 molecules to show the herringbone arrangement of the molecules in the unit cell. The center molecules are colored red to emphasize the herringbone structure.

2.2 Substrates

2.2.1 TiO$_2$(110)-(1x1)

Titanium dioxide in its rutile form is often used as substrate in surface science because it is one of the best characterized oxide surfaces [63]. For the special case of 6P thin film growth it is interesting for a number of reasons. While stoichiometric TiO$_2$ is an insulator it can be transformed into a conductive material by heating in UHV. The reason is a partial loss of oxygen from the crystal and the newly formed TiO$_{2-X}$ is oxygen vacancy doped. However, during this process the once transparent TiO$_2$ gets more and more opaque. By a precisely controlled sputtering and annealing cycle a (1x1) reconstruction can be created on the TiO$_2$(110) surface. The following procedure was used to prepare the TiO$_2$(110)-(1x1) surface for the LEEM experiments presented in section 3.1 on page 41. After an initial annealing step for 20 min at 700 °C:

- Sputtering with 1 keV for 5 min

- Annealing at 700 °C for 10 min (heating rate 5 K/s)

Usually, this cycle was repeated 4 times.

As can be seen from figure 2.2 the reconstructed surface is characterized by parallel running rows of oxygen atoms in the [001] direction. These rows are separated by 6.5 Å, enough space to accommodate a 6P molecule. In addition, these rows make the TiO$_2$(110)-(1x1) surface an extremely anisotropic surface with only twofold symmetry.
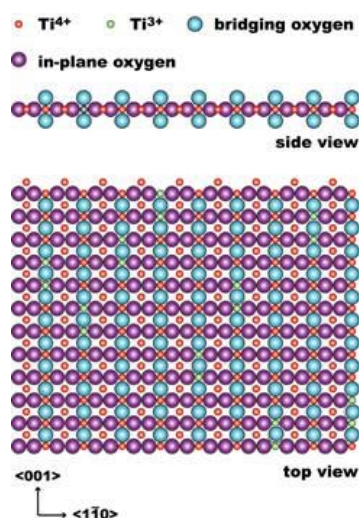
Figure 2.2: Ball model of the $TiO_2(110) - (1x1)$ surface [64].

2.2.2 Mica(001)

Mica is a rock forming mineral with the chemical formula $KAl_2(Si_3Al)O_{10}(OH,F)_2$. It has one perfect cleaving plane which is the (001) plane. The correct crystallographic classification is muscovite-$2M_1$. The lattice constants are $a =5.20$ Å, $b =9.03$ Å, and $c =20.11$ Å. The angles in the unit cell are $\alpha =90.00°$, $\beta =95.78°$, and $\gamma =90.00°$. The unit cell and the stacking of the layers is shown in figure 2.3. The top layer is build from a distorted hexagon of oxygen atoms. The oxygen atoms form tetrahedrons around the silicon atoms. Two mirrored layers of these are separated by the layer containing the aluminum and – in our case – the OH^- groups. One of these OH^- groups changes its position between adjunct layers. However, these anions only take two different positions therefore the original threefold symmetry is reduced to a twofold symmetry. The displacement of the anions is also visible from the top layer by looking through the hexagonal opening in the T (formed by the teragonal arranged oxygen atoms) layer. The two directions are separated by 120°. Ab initio calculations show that these considerations are also correct for the relaxed surface layer [65].

When mica is cleaved along one of the marked I layers (holding the potassium) half of the potassium ions stay on each side. The potassiums ions left on the surface after cleavage where found to form large domains with a step height of roughly 1 Å. However, these initially formed domains disappear after 10 min. [67,68]

Modification of the mica(001) surface

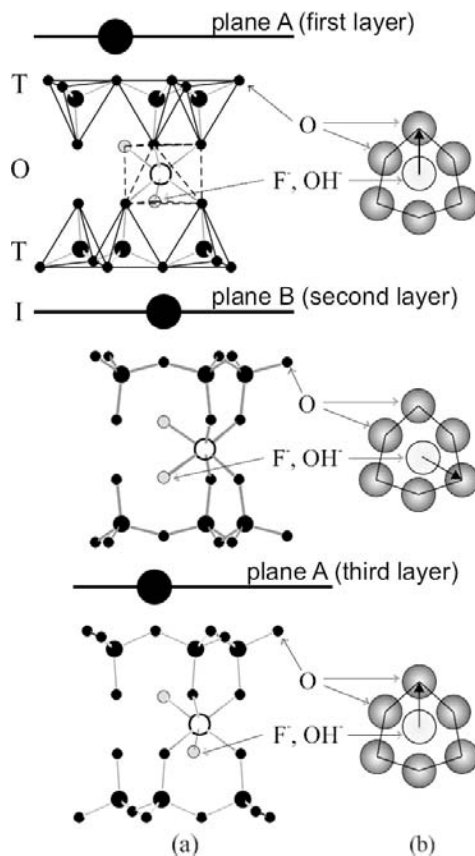Two attempts have been made in this work to break the high anisotropy of the mica(001) surface.

Figure 2.3: Crystal structure of mica. (a) side view, (b) top view. The displayed atoms are potassium (large filled circle), silicon (medium filled circles), oxygen (small filled circles), aluminum (large open circles), and $(OH, F)^-$ anions (light gray circles) [66].

Surfactants can be used to modify the growth of thin films as has been briefly discussed in section 1.2 on pages 6 and 10. Here, two methods have been used to investigate the influence of surfactants on the growth of organic thin films. The effect of sample cleanness has been investigated by exposing the cleaved samples for several days to ambient conditions. A short heat treatment in UHV followed. However, that heat treatment is not efficient enough to remove all absorbed carbonaceous residues. In addition an increased amount of water and gases like CO might be left on the surface.

To create controlled carbon pre deposits a relatively thick 6P film (10 nm) was grown at low temperature (110 K). The film is then exposed to MgK_α radiation for up to 2 h from an x-ray gun. After a final temperature flash to desorb cracking products and the remaining 6P only carbon is left on the sample surface. The carbon coverage is given in fractions of the saturation coverage (for details see [9, 69]).

Ion bombardment of crystalline surfaces is often used to clean the sample surface. However, the use of ion beams changes also the structure of the sample surface. Several examples of surface structures regular and irregular can be found in the literature [70–

72]. Bombarding mica with ions at low energies ($\approx$500 eV) for only short periods of time will already lead to an unrepairable destruction of the top layer of the crystal. This natural mineral is formed under high geological pressures and high temperatures common in geological processes. Normal annealing under UHV conditions can not recover the crystalline nature of the sample surface, and a amorphous surface layer is the result of such a treatment.

Figure 2.4 shows the morphology of a mica(001) surface after about 30 min of ion bombardment with 500 eV Ar$^+$. The surface is characterized by two typical features, deep holes with a depth of roughly 5 nm and hills with a height between 10 nm and 20 nm. The hills might be the result of changes in the structure due to ion damage. A possible scenario is the formation of H_2O when the OH groups are broken out of the crystal structure. The water can easily diffuse between the sheets and form bubbles that press the surface layers upwards. This structural change leads to a change in volume of the crystal lattice and results in the surface bumps. Furthermore, a ripple structure extending over the whole sample surface can be seen.

A cross section (fig: 2.4a) through the two dimensional Fast Fourier Transform (not shown) of the image reveals two satellite peaks. Taking half of the distance between them in the frequency domain and transforming it back to a real space distance gives a wave length of the ripple structure of 180 nm. The height of the ripples, obtained from cross sections through various images, is measured between 3 Å to 5 Å. The rms roughness of the surface has a value of 1.1 nm$\pm$0.3 nm and neglecting the craters and hills on the surface a value of 0.6 nm$\pm$0.2 nm. Both values are significantly higher than the rms roughness of a freshly cleaved mica(001) surface of 0.1 nm. As a consequence
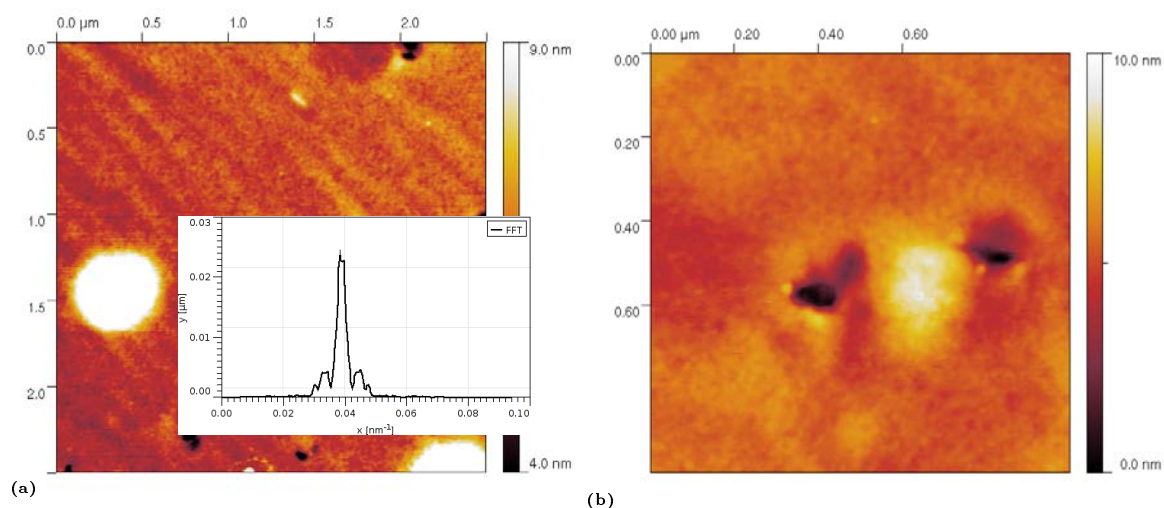

Figure 2.4: AFM images of a sputtered mica(001) surface. (a) shows 2.5 µm image of the surface after long time sputtering. A ripple structure and holes are characteristic for this surface. The inset shows a cross section through the 2D-FFT. (b) enlarged view of two holes in the mica(001) surface.

the following samples where sputtered only for times between 60 s and 250 s where no morphological modification could be observed. These times were long enough so that no LEED pattern could be observed from the bombarded surfaces, therefore at least the top most layer is amorphous.

2.2.3 Gold(111)

Gold has a face centered cubic (fcc) bulk structure with a lattice constant of 4.079 Å. The top most layer of the (111) surface is six fold symmetric. When also the second layer is taken into account the symmetry is reduced to three fold. The Au(111) surface is well investigated because of its $(22x\sqrt{3})$ reconstruction at room temperature [73]. The reconstruction is the result of the relaxation of the top most surface layer which then accommodates 23 atoms along the $<1\bar{1}0>$ while the substrates holds only 22 atoms on the same distance. This leads to a deformation of the atomic rows in $<11\bar{2}>$ direction and also in the z-direction. Due too the threefold symmetry of the surface also three domains exist. However, on one surface terrace only two of these domains occur at the same time and result in the well known herringbone reconstruction [74]. On a crystal surface all domains can be found due to steps. Figure 2.5 shows the reconstruction imaged by STM.

The influence of this reconstruction on the growth of organic thin films is not completely clear. Recent STM results show that the reconstruction is not lifted upon 6P deposition [51]. This is also true for PTCDA on Au(111)-$(22x\sqrt{3})$ deposition [76]. There it is important to consider the reconstruction to successfully explain the mono layer structure of PTCDA [77]. For 6P it was shown that depending on growth tem-
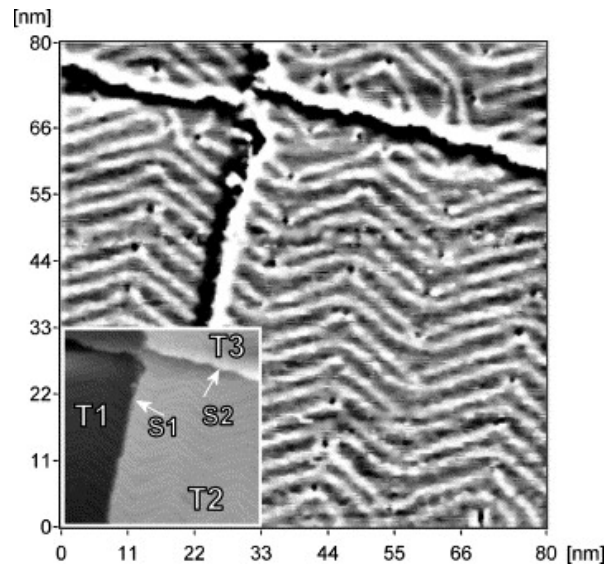

Figure 2.5: 80 nm by 80 nm large Laplace filtered STM image of the herringbone reconstruction found on Au(111) (the inset shows the unfiltered image) [75].

perature and film thickness the molecules are sometimes aligned along the valleys of the reconstructed surface [78].

2.2.4 Amorphous SiO$_2$

SiO$_2$ wafers are probably the most common substrate in surface science. They are easy to get and well characterized. The semiconductor industry has put a lot of effort into the optimization of the production process of SiO$_2$ as it is one of the key components in all thin film transistors. There, it is used to separated different conducting parts from each other but gains special attention when used as the gate oxide to separate the gate electrode from the conductive channel between source and drain.

Here, a thermally grown SiO$_2$ was used because it is an isotrop surface of high relevance for the semiconductor industry. The high control on the roughness of SiO$_2$ wafers is crucial for good device performance. A smooth substrate surface is a prerequisite for efficient organic devices [79].

2.3 Growth techniques

2.3.1 Hot Wall Epitaxy

The main part of a Hot Wall Epitaxy (HWE) System [22,80] is an inert tube containing the deposition material. This tube – made from quartz or some other inert material – is placed inside a High Vacuum (HV) system. Figure 2.6 depicts the principle outline of the vacuum chamber used and the tube containing the source. This tube is closed either by the substrate or a shutter on top. Different heating zones along the tube wall allow to create nearly uniform and isotropic flux of material towards the substrate surface. The HV chamber containing the HWE reactor also contains a preheating oven and a computer controlled manipulator for sample transfer.

Choosing the wall temperature slightly higher than the source temperature but still below the dissociation temperature of the source material and keeping the substrate temperature below all other temperatures allows deposition of material only on to the substrate. This is one of the advantages of HWE compared to other techniques – there is no source material loss, as all the material is either deposited onto the substrate or stays inside the reactor tube for the next experiment. No Ultra High Vacuum (UHV) is needed because the tube is closed with the substrate. Therefore the environment inside the tube is cleaner as compared to the rest of the HV system. Different heating zones allow an individual control of the temperatures in different areas of the tube and the formation of a high partial pressure of source material and a low super-saturation in the vicinity of the substrate surface. As a result HWE allows the growth of epitaxial layers close to the thermodynamic equilibrium [22,80]. Together with the fact that, in contrast to conventional MBE, the very uniform near field distribution of the beam flux is used, the large 6P molecules are allowed to find the best configuration on the surface [81]. This leads to an highly ordered structure in the deposited film. Furthermore, the
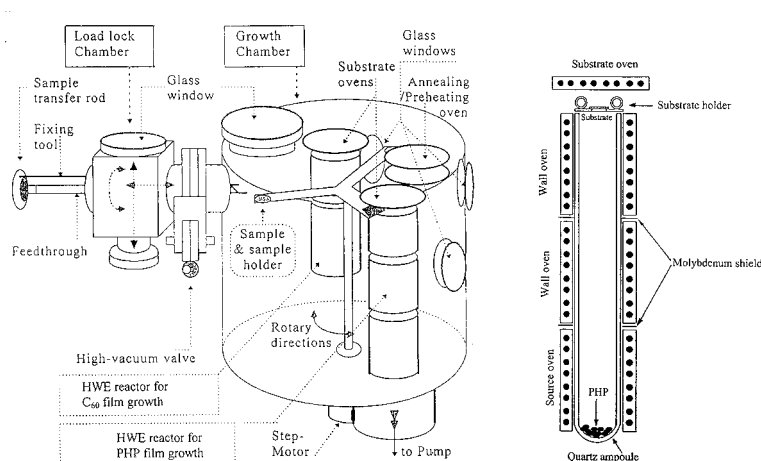
Figure 2.6: Sketch showing the outline of a HWE similar to the one used in the presented study. A detailed drawing of the tube containing the source material is shown on the right side (taken from [22]).

sticking probability goes to one as each molecule has an unlimited number of retries to attach to the surface.

One of the major drawbacks in HWE is the lack of possibility for in situ measurements of film thickness and growth rate. However, if the used HWE system was operated with it's typical parameters (given in tab. 2.2) a growth rate of 2 nm/s is a good estimate [82].

2.3.2 Organic Molecular Beam Epitaxy

MBE is a versatile technique for growing thin epitaxial structures made of semiconductors, metals or insulators. In MBE, thin films crystallize via reactions between thermal-energy molecular or atomic beams of the constituent elements and a substrate surface which is maintained at an elevated temperature in UHV [22].

Organic Molecular Beam Epitaxy (OMBE) is an MBE variant that uses small organic molecules as source material. Although normal evaporation cells employed in conventional MBE can also be used here this is not necessary as the sublimation temperature for organic materials is between room temperature (or even below) and a few hundred degree Celsius. However care has to be taken not to deposit large amounts of material on hot filaments or other active components inside the chamber as the high temperatures used in various devices can lead to crack products that make controlled studies

6P source temperature	240 °C
Wall temperature	260 °C
Substrate temperature	90 °C
Pressure during growth	$6 \cdot 10^{-6}$ mbar

Table 2.2: Typical HWE growth conditions used here.

difficult. Figure 2.7 shows the UHV system at the Institute of Physics, University of Leoben, Leoben, Austria used for the preparation of some of the films in this work.

MBE allows a number of in situ monitoring and characterization techniques. To measure film thickness Quartz Crystal Microbalance (QCM) technique is used in most OMBE systems. QCM devices use a gold covered piezoelectric quartz crystal which is oscillating with its resonance frequency f_0. Correlation between mass uptake during evaporation and the shift in resonance frequency can be achieved by means of the Sauerbrey equation

$$\Delta f = -\frac{2f_0^2}{A\rho_q v_q}\Delta m \tag{2.1}$$

where Δf is the observed frequency shift, A is the active area of the crystal, ρ_q is the density of quartz and v_q is the shear wave velocity in quartz. Δm is the mass added to the crystal. If the density of the film material is known this allows to calculate the film thickness.

Figure 2.7: UHV system at the Institute of Physics, University of Leoben, Leoben, Austria used in this work.

2.4 Characterization

This section will describe the characterization methods used. In particular atomic-force microscopy (section 2.4.1), X-ray diffraction (section 2.4.3 on page 33) and LEEM (section 2.4.4 on page 35). For additional methods useful for the complete understanding but not directly part of this investigation, the reader is referred to other publications when ever necessary.

2.4.1 Atomic-Force Microscopy

Atomic Force Microscopy (AFM) [83] is a Scanning Probe Microscopy (SPM) method that allows quantitative measurements of surface topography at resolutions down to the atomic length scale [84]. It is using a small tip mounted on a cantilever which is moved across the surface by a piezoelectric motor. The deflection of the cantilever is then detected and converted into a z(x,y) information. The most common method for detecting the cantilever movement utilizes a laser beam which is reflected by the cantilever and detected by a position sensitive photo diode array. Due to the long path of the laser beam a high amplification of the tip movement is achieved. Figure 2.8 shows the principle layout of an AFM.

The AFM which was used for this work is a *Digital Instruments NanoScope IIIa Scanning Probe Microscope* (see figure 2.9) equipped with a *AS-130 (J)* piezo scanner. It allows a maximum image size of 100 μm² and a maximum vertical deflection of 4.7 μm.

Contact Mode

The most obvious way to scan a tip across a surface is called contact mode. In this mode the tip touches the surface, while it is moved laterally. Pauli and Coulomb forces
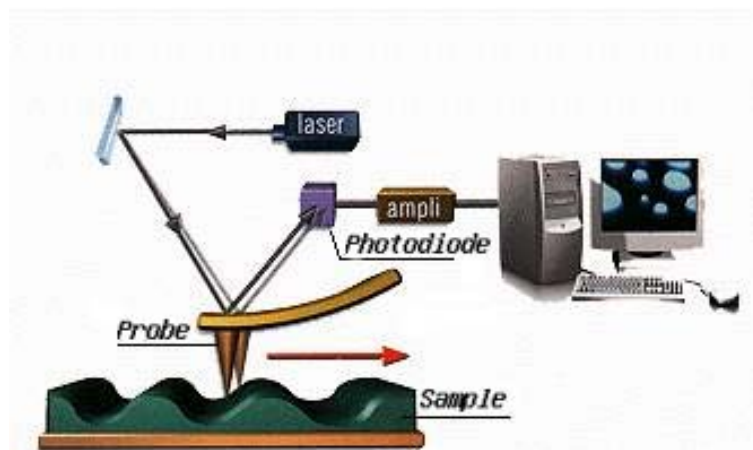

Figure 2.8: Principle of AFM measurement. Including the path of the laser beam, photo sensor, tip and sample. (from [85])

Figure 2.9: *Digital Instruments NanoScope IIIa Scanning Probe Microscope* used for this work, including an optical microscope for positioning the sample underneath the tip.

lead to a repulsive force on the tip in the nN range. These forces lead to a bending of the cantilever that can be detect by the above described detection system and give rise to the name of the method. The feedback loop tries to keep the bending and therefore the force between tip and sample constant. This is achieved by keeping a constant cantilever deflection by adjusting the z-position of the sample with respect to the tip. This mode is called *constant force mode*. The resulting image represents the sample morphology. In principle also *constant height mode* is possible, the image can then be interpreted as a map of the forces between tip and sample

Friction Force Microscopy

For Friction Force Microscopy (FFM) or Lateral Force Microscopy (LFM) [86, 87] the tip is scanned in constant force mode perpendicular to its long axis. Due to friction forces between the substrate surface and the tip, the cantilever twists and the laser beam is deflected horizontally. However, being a contact mode method one has to carefully select the applied normal force. High normal forces will lead to a clearer LFM image but at the same time more wear is generated. The measurement principle is depicted in figure 2.10.

The method allows to distinguish materials with different friction constants. For the investigated film/substrate combinations different friction constants can be assumed due to the different chemical termination of the surface.

Tapping Mode

Most measurements where done using Tapping Mode (TM)-AFM also called intermittant contact. In tapping mode, the cantilever oscillates at or close to it's resonance frequency (for topography imaging typical between 200 kHz and 400 kHz). The amplitude of this oscillation is typically between 20 nm and 40 nm. During scanning the tip lightly *taps* the surface at the bottom of its swing. When the tip moves across the
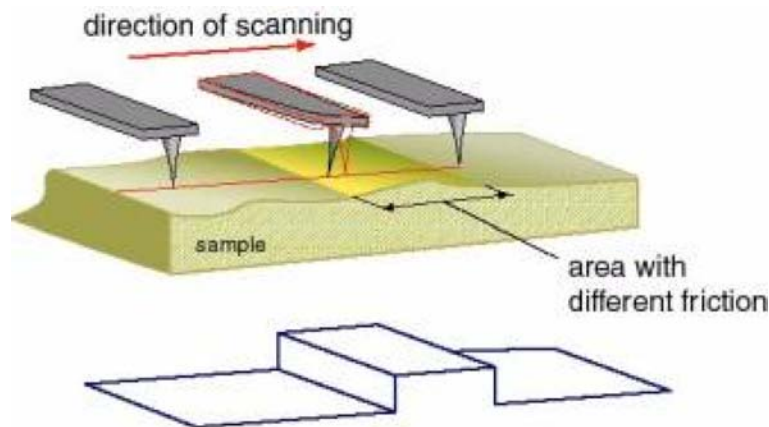

Figure 2.10: Measurement principle of LFM [88]

surface, the feedback loop maintains a constant oscillation amplitude obtained from the rms signal of the cantilever oscillation at the split photo diode by varying the sample tip position. The vertical position of the scanner – to maintain a preset rms signal (the *setpoint*) – for each data point is recorded as the height image. Figure 2.11 outlines the principle.

Tapping mode allows to follow the surface morphology at a constant very low tip-sample interaction. Lateral forces in contact mode can dull the tip or damage the sample surface, are no problem here as the tip touches the surface only for very short periods of time. The typical oscillation amplitude is also larger than the thickness of the surface water film when imaging under ambient conditions.

Phase Imaging

Phase imaging allows to map the viscoelastic properties of the scanned surface parallel to the morphology [90]. Quantitative interpretation of the results is hard but the qualitative information that can be obtained allows the identification of materials with different mechanical properties (e.g. film and substrate) and even a relative "hard"/"soft" characterization of the different materials.

The phase image is obtained by recording the phase shift between the excitation oscillation and the resulting cantilever oscillation. This phase shift can be related to the energy that is dissipated from the cantilever oscillation into the sample surface, which in turn is related to the viscoelastic properties of the surface material. For organic thin films the difference in mechanical properties between film and substrate is high. So usually clear images can be obtained without great effort. However, the technique is capable to distinguish between between much smaller difference in material properties (e.g. between the crystals and the amorphous matrix of a semi-crystalline polymer [91]). One problem in phase imaging of soft materials on hard substrates is tip contamination due to pick up of parts of the soft layer. This changes the interaction of the tip with the substrate and can lead to a change or even a complete loss of contrast in the phase image.
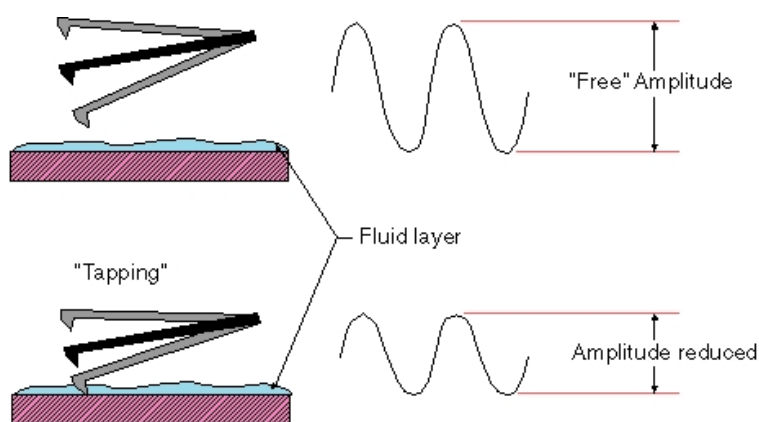

Figure 2.11: Principle of tapping mode. (from [89])

AFM-tips

Cantilever and tip selection has a large influence on the quality of the obtained images. Different probes exist for the different modes. However, also certain sample properties like morphology and conductivity can influence the choice.

Tapping mode tips used here were fabricated from Si. Generally, these cantilevers are coated with Al on the detector side (e.g. Nanosensors PPP-NCHR type) to increase reflectivity and therefore increase signal to noise ratio as well as the achievable scan speed. However, especially for the films prepared by HWE on mica(001) Pt coated tips were used (e.g. Nanosensors PPP-NCHPt). Having the same reflectivity as Al coated cantilevers, the lower resistivity and inertness of the material allowed to achieve better results with easily charged mica substrates.

For some measurements high density carbon (HDC) [92] (e.g. NanoTools U1s) tips were used. These tips with guaranteed tip radii below 5 nm and half opening angles of less then 4° allow to image steepest structures. Most of the high-detail images presented have been obtained with these very sleek tips. The typical specifications for all these tips are given in table 2.3.

Contact mode tips have a lower force constant compared to tapping mode tips. This is necessary to protect sample and tip from damage. Again normally cantilevers with an Al coating on the detector side have been used to increase reflectivity. For LFM tips like Nanosensors PPP-LFMR have been used. The relevant parameters are given in table 2.4.

2.4.2 Quantitative analysis of AFM images

Although three-dimensional real space images on the μm- or nm-scale are pretty and informative by them self, quantitative methods are required to access all the information hidden in such files. However, an important prerequisite are high quality images without

cantilever length	125 μm
force constant	42 N/m
resonance frequency	300 kHz

Table 2.3: Typical specifications of tapping mode tips

beam length	$225 - 450$ μm
force constant	0.2 N/m
resonance frequency	$25 - 13$ kHz

Table 2.4: Typical specifications of LFM and contact mode tips

noise or any other tip or scanner generated artefacts. It is left to the operator to decide if a structure is real or an artefact created for example by a dull tip or a to high scan speed.

Roughness characterization

The first and most often calculated value that describes a random rough surface (like the substrate) is the root mean square (rms) roughness σ. For a area of size LI that consists of MN points

$$\langle\, \sigma\, \rangle = \sqrt{\frac{1}{LI} \int\limits_{-\frac{L}{2}}^{\frac{L}{2}} \int\limits_{-\frac{I}{2}}^{\frac{I}{2}} \left[z(x,y) - \langle\, z\, \rangle_{LI} \right]^2 dx dy}, \tag{2.2}$$

or

$$\langle\, \sigma\, \rangle_M N = \sqrt{\frac{1}{MN} \sum_{j=1}^{M} \sum_{i=1}^{N} \left[z(i,j) - \langle\, z\, \rangle_{MN} \right]^2}. \tag{2.3}$$

It can be used to describe the vertical fluctuations of a surface. For most situations the obtained value will depend on the field of view that was used and the resolution (the size of pixels). However, describing a surface only by its vertical roughness is not sufficient. The shape of the mounds and the lateral arrangement of them will also change the roughness but can not be expressed in terms of the rms-roughness.

To access the values describing these features one has to calculate second order statistical functions which are explained in the following. They are usually calculated along the fast scan axis of AFM images and then averaged over all scan lines. However, doing so one can only extract information along the (usually) x-axis of the image. This is of importance when the interesting structures are under an arbitrary angle in the image.

The one dimensional Height height correlation function (HHCF) is given by

$$\langle\, G(x)\, \rangle_L = \frac{1}{L} \int\limits_{-\frac{L}{2}}^{\frac{L}{2}} (z(x_0) - \langle\, z\, \rangle)(z(x_0 + x) - \langle\, z\, \rangle) dx_0 \tag{2.4}$$

with $0 \leq x \leq L$, or

$$\langle\, G(md)\, \rangle_N = \frac{1}{N - m} \sum_{i=1}^{N-m} (z_i - \langle\, z\, \rangle)(z_{i+m} - \langle\, z\, \rangle). \tag{2.5}$$

In the later case m is the index of the current point and d the real space distance between the individual points.

Closely related to G is the Height difference function (HDF) H. As for G, the best method to obtain this function is along the fast scan axis. H can than be estimated as

$$\langle\, H(x)\,\rangle_L = \frac{1}{L} \int\limits_{-\frac{L}{2}}^{\frac{L}{2}} [z(x_0 + x) - z(x_0)]^2 \, dx_0 \tag{2.6}$$

with $0 \le x \le L$, or

$$\langle\, H(md)\,\rangle_N = \frac{1}{N - m} \sum_{i=1}^{N-m} [z_{i+m} - z_i]^2 . \tag{2.7}$$

Comparing the integrals or sums of (2.4) and (2.5) with (2.6) and (2.7) makes clear why the one is called height-height correlation function (G) while the other is called height difference function (H). These values are usually computed for each line (normally horizontally along the fast scan direction) in the image and than averaged. The obtained values are therefore only correct for features running perpendicular to that direction.

For a self-affine surface with a cutoff these functions can be fitted with [93, 94]

$$G(x) = \sigma^2 e^{-\left(\frac{x}{\xi}\right)^{2\alpha}} \tag{2.8}$$

and

$$H(x) = 2\sigma^2 \left[1 - e^{-\left(\frac{x}{\xi}\right)^{2\alpha}}\right] . \tag{2.9}$$

Three parameters describing the surface can be obtained this way. σ the rms-roughness already given by (2.3), ξ the lateral correlation length and the roughness exponent α. ξ is the average distance on the surface between the two points x and $x + \xi$ were they are still correlated to each other. α is a measure how wiggly the surface is. Generally, small α values mean a more jagged surface morphology while higher values correspond to a smoother surface profile.

However, for mounded surfaces different forms of H and G are proposed [95]. This is necessary as (2.8) and (2.9) can not follow the oscillatory behaviour of H and G if there are regular spaced mounds on the surface. To fit G

$$G(x) = \sigma^2 e^{-\left(\frac{x}{\zeta}\right)^{2\alpha}} \cos\left(\frac{2\pi x}{\lambda}\right) \tag{2.10}$$

can be used and

$$H(x) = \sigma^2 \left[1 - e^{-\left(\frac{x}{\zeta}\right)^{2\alpha}} \cos\left(\frac{2\pi x}{\lambda}\right)\right] \tag{2.11}$$

for the height difference function.

As a result, in addition to σ and α, the average mound separation λ and the system correlation length ζ can be obtained. ζ determines how randomly the mounds are distributed on the surface. A smaller value of ζ means a more random distribution. Figure 2.12 gives an example for the HHCF of a mounded surface (for details see 3.2.3). The difference between the two fit functions (2.8) and (2.10) is obvious. Although the

data is obtained from a 1 μm image only the first 200 nm of the resulting curves are shown. The reason is that for larger m the data points used for an average in (2.5) are fewer. When $m = N - 1$, there is only one data point and the accuracy of the estimation is bad. Therefore we always show about a fifth of the total data and also only this fifth is used for the calculation of the fits.

Analysis of the feature size

Non random surfaces which include regular structures with distinct sizes require a more detailed analysis. To get quantitative numbers from structured surfaces one can of course use section analysis or similar tools. However, to get an statistical average particle analysis or grain analysis routines have to be used. The most common approach to identify a grain on a surface is thresholding. A certain height limit is defined and surface points above this limit are used for further processing. Image pixel that build a continuous region can than be identified as a *grain*. The prerequisite for this method is a smooth background with a surface roughness much smaller than the feature size. This is usually fulfilled for the samples in this investigation. But, also the long range flatness of the surface has to be much smaller than the grain height to be able to separate background from interesting features. This method also fails if the grains touch each other and no reference background can be identified.

Water shedding algorithms can than be used to identify the individual grains on the surface [96, 97]. The process implemented in the used software [98] is as follows

1. The surface is inverted so that $z(x, y) = -z(x, y)$.
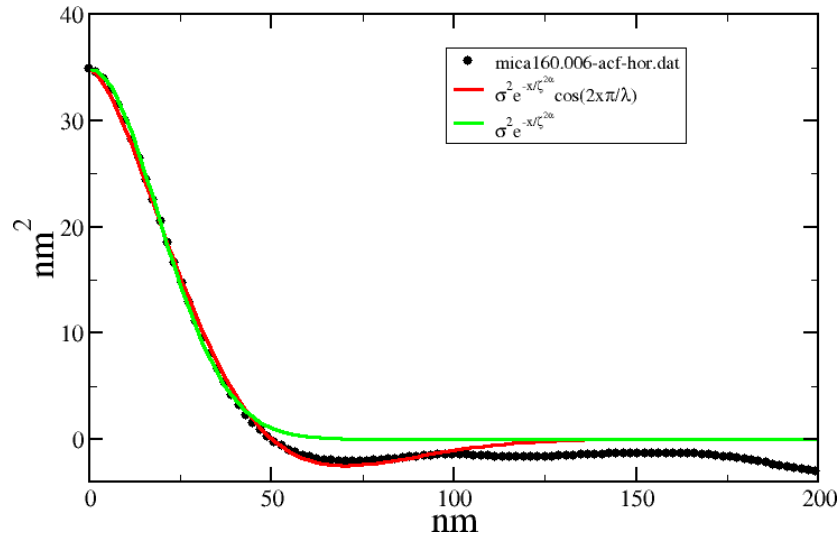
Figure 2.12: HHCF G for a 6P thin film grown mica(001) at $-160\,°C$ (for details see section 3.2.3). Black dots show the data obtained from the AFM image. The green curve is obtained from (2.8) while the red curve is obtained from (2.10).

2. On each pixel on the inverted surface a virtual water drop is placed. If the droplet sits in a local minimum the position is recorded, if not the droplet will follow the steepest pathway to the next minimum. This way the droplets start to create a system of small lakes of different size on the surface. After this step has been repeated several times the smallest lakes were removed under the assumption that they have been created in minima resulting from noise.

3. The position of the created lakes is recorded and more water is rained on the surface. Now different situations can arise:

   a) The drop falls into an already existing lake, then the droplet is merged with the grain.

   b) The droplet falls on the surface outside an existing lake, but there is a particular lake in the nearest neighborhood. In this situation the position of the droplet is added to the existing lake. As a result the grain gets bigger

   c) The droplet lands outside a lake and there is no lake nearby. In this case the droplet is ignored.

   d) The droplet lands outside a lake and there are two or more grains in the nearest neighborhood. In this case the position of the droplet is marked as a grain boundary.

   e) The droplet falls on position marked as grain boundary. Than the droplet is also marked as grain boundary.

If drop size, number of steps in the first part, the minimum grain size after the first part as well as the size of the droplets in the second part and the number of steps is chosen appropriately, the result are grains touching each other by grain boundaries and filling the image area. The strength of this method is that no uniform background is needed and also connected grains can be separated.

Independent of the algorithm used for identifying the grains, one can than calculate properties like grain width and length, grain area and grain height.

Integral properties can also be gained from the roughness analysis presented above. From (2.10) and (2.11) one can obtain λ. The mound separation gives the distance between individual features or if the features touch each other it gives the feature size. However, often the particles on the surface are not oriented horizontal or vertical and the methods for obtaining 1D-HHCF and 1D-HDF presented above fail. In this case the 2D Fast Fourier Transformation (FFT) of the image can help to access these properties. Figure 2.13 shows a typical result. Figure 2.13a a 7 nm thick 6P film grown at 90 °C on mica(001) (for details see sec. 3.2.3 on page 60). The morphology is characterized by parallel running features. This is also reflected in the 2D-FFT, by a long small feature perpendicular to the direction of the structures. A cross section (presented in fig. 2.13b) along the main axis of the FFT feature reveals the internal structure in more detail. The distance of the two peaks from the center of the plot is indirect proportional to the feature-feature distance in real space. From 2.13b a value of 7 μm^{-1} can be obtained. This results in a average feature distance in real space of 140 nm.
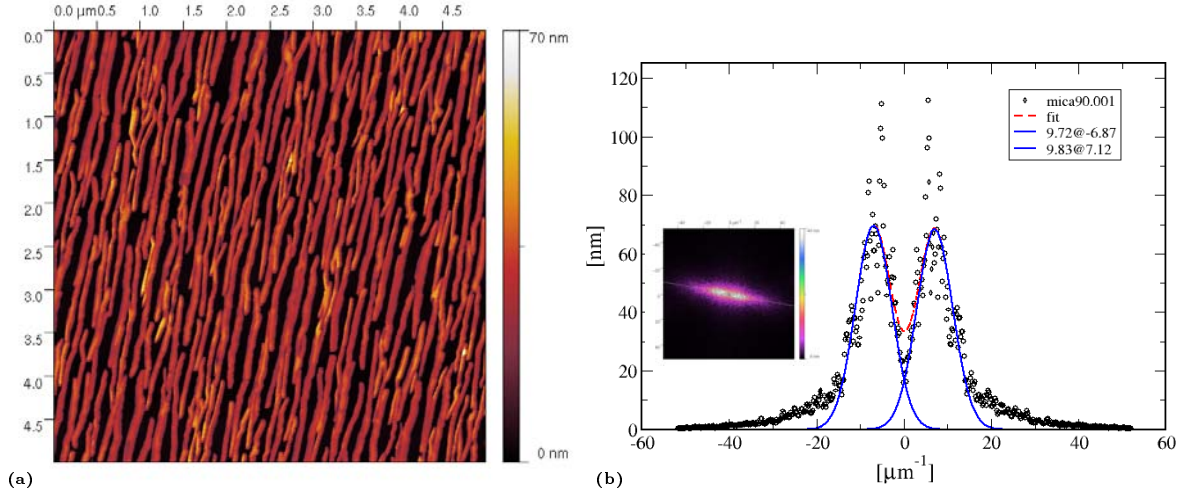
Figure 2.13: (a) 5 μm by 5 μm AFM image of a 7 nm thick 6P film grown on mica(001) at 90 °C. (b) Cross section through the 2D FFT (shown in the inset) along the main feature, revealing two peaks. The peaks were fitted by a Gaussian to obtain the position and FWHM given in the graph.

However, a FFT treats data as being infinite which is not the case for images obtained by AFM. Therefore, some cyclic boundary conditions have to be implemented and the data has to be windowed to allow a smooth transition across the boundaries. For the FFTs presented in this work a Hamming function

$$w_{Hamming}(x) = 0.54 - 0.46 \cos 2\pi x \qquad (2.12)$$

has been used [98].

Often filters or presentation modes are used to display data to underline a certain feature in the image and suppressing other unwanted structures. A huge number of mathematical methods is available to render data in every possible way. Besides the smoothing filters like median filtering for the production of nice 3D graphs, edge enhancement filters are used in this work. The routine visualizes the square root of the difference between the 2/3 and 1/3 quantiles of the data values in a circular neighbourhood of radius 2.5 pixels centered around the sample. If applied to a morphology image of a stepped surface, the resulting image will include the steps but nothing else. An important feature of this filter is that it is relatively insensitive to noise that could be misinterpreted as a step. An example is given in figure 3.53.

2.4.3 X-ray diffraction

X-ray diffraction is a powerful method to determine the crystal structure of organic thin films. To get constructive interference of a diffracted beam the Laue-Equation (2.13) has to be fulfilled for all three lattice vectors ($\boldsymbol{a}$, $\boldsymbol{b}$ and $\boldsymbol{c}$)

$$\boldsymbol{a} \cdot \boldsymbol{q} = 2\pi\hat{h} \tag{2.13a}$$

$$\boldsymbol{b} \cdot \boldsymbol{q} = 2\pi\hat{k} \tag{2.13b}$$

$$\boldsymbol{c} \cdot \boldsymbol{q} = 2\pi\hat{l} \tag{2.13c}$$

$\boldsymbol{q}$, the scattering vector is defined as the difference between the outgoing $\boldsymbol{k}$ and the incoming $\boldsymbol{k_0}$ wave vectors: $\boldsymbol{q} = \boldsymbol{k} - \boldsymbol{k_0}$. $\hat{h}$, $\hat{k}$ and $\hat{l}$ are the Laue indices. Starting from (2.13) one can deduce the Bragg equation

$$2d_{hkl}\sin\left(\frac{2\Theta}{2}\right) = n\lambda \tag{2.14}$$

Here 2Θ is the angle of beam deflection, n an integer, λ is the used wavelength and d_{hkl} is the distance of the scattering lattice planes defined by the Miller indices (hkl) which are connected to the Laue indices by $(\hat{h}\hat{k}\hat{l}) = n(hkl)$. Furthermore, the scattering vector $\boldsymbol{q}$ has to be parallel to the normal vector $\boldsymbol{n}$ of the scattering lattice plane.

$$\boldsymbol{n}\|\boldsymbol{q} \tag{2.15}$$

Two different methods have been used here to obtain information on the crystallographic structure and the orientation of the molecules.

Specular Scans

This method is also known as $\Theta/2\Theta$, L-scan, or q_z-scan. The setup is chosen in such a way that the incident angle and the detection angle are the same with respect to the sample surface (see figure 2.14). In this symmetric setup the scattering vector $\boldsymbol{q}$ is always perpendicular to the sample surface. Therefore, only net planes parallel to the surface can fulfill equations (2.14) and (2.15) and give sharp Bragg reflections. The resulting spectrum is than compared to calculated spectra from already well-established crystal structure data.

Rocking curves

Rocking curves give information on the crystalline quality of the investigated sample. If there are small deviations from the perfect alignment of different crystallites these leads to a broadening of the lattice points in reciprocal space. This broadening is called mosaicity. Smaller mosaicity means better alignment in the sample. To obtain rocking curves for a specific reflection the x-ray source as well as the detector are fixed while the sample is tilted (rocked) forth and back around the ideal position (see figure 2.15). If the net planes probed is perfectly aligned through out the sample a sharp reflex while be obtained. Rocking curves are usually characterized by their Full Width at Half Maximum (FWHM). The smaller the FWHM, the narrower the peak the better the crystalline quality. However, in addition to that also finitte size effects can be observed.
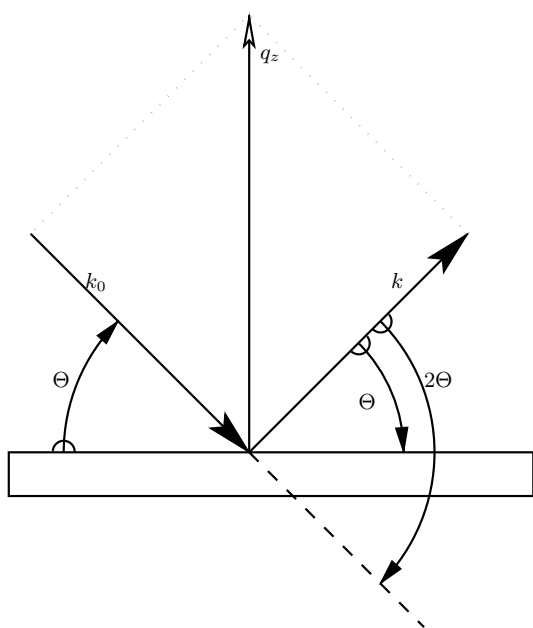
Figure 2.14: Scheme of the $\Theta/2\Theta$ scan. Θ: angle between incoming beam and sample surface. 2Θ angle between incoming and outgoing beam.
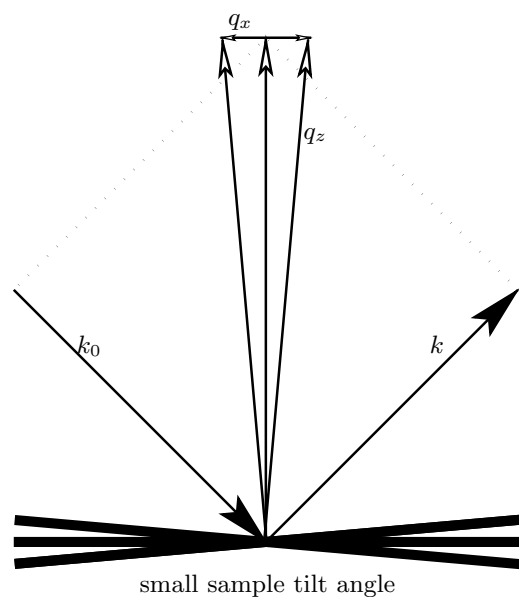
Figure 2.15: Scheme of a rocking curve scan. The sample is tilted by a small angle, while k and k_0 are kept constant.

X-ray setup

The crystallographic data presented in 3.2.2 and 3.2.4 have been obtained at the G2 beamline at CHESS, Cornell University. This beamline is equipped with a κ-goniometer, 1D gas detector, and a Soller collimator [99]. This setup (see figure 2.16) allows to obtain specular scans and gracing incident diffraction data.

2.4.4 Low Energy Electron Microscopy

In a Low Energy Electron Microscope (LEEM) a high energy (typical 20 keV) electron beam is decelerated by a *cathode* lens close to the sample surface. The electrons reach the sample with a very low energy (typical 5 eV to 20 eV) where they can interact only with the outermost layers of the surface. The electrons diffracted from the surface are collected by the same lens and are then reaccelerated. The principle device of modern LEEMs is the beam splitter which deflects the incoming electrons towards the sample but the reflected ones into the imaging column. In the imaging columns the electrons can either be observed in the back focal plane with the help of an intermediate lens (Low Energy Electron Diffraction (LEED) mode) or with the help of an aperture and leaving out the intermediate lens to create an image on the fluorescence screen. Figure 2.17 shows the principle setup.

The achievable resolution can be as low as several nm (better than 8 nm on the used

Figure 2.16: κ-goniometer at the G2 beamline at CHESS.
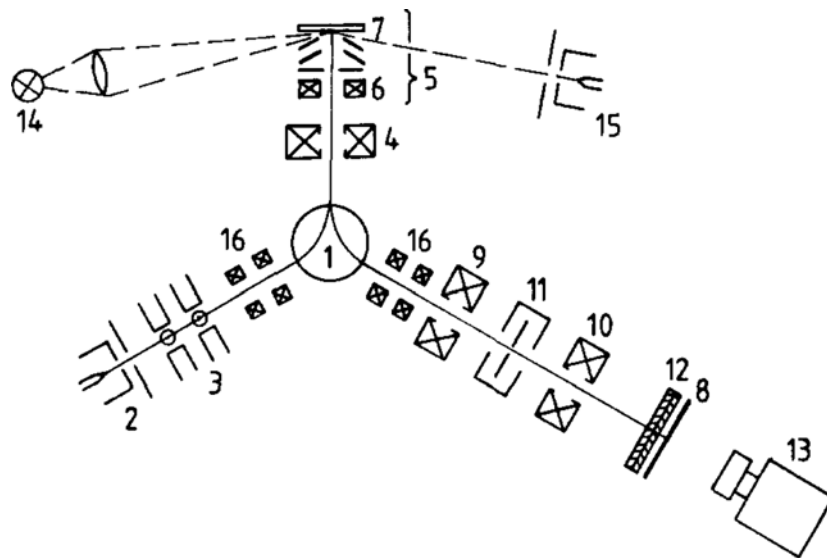
Figure 2.17: Principle LEEM setup. (1) Magnetic separator, (2) field emission gun, (3) quadrupoles, (4) objective lens, (6) magnetic stigmator, (7) specimen, (8) screen, (9) and (10) magnetic lenses, (11) electrostatic filter lens, (12) multichannel plates, (13) camera, (14) Hg lamp, (15) auxiliary electron gun, (16) deflection coils. From [100].

microscope), while aberration corrected microscopes have a theoretical resolution in the sub-nm regime [101]. Most often, contrast is achieved by utilizing the fact that the reflectivity for electrons is highly sensitive to difference in the crystal orientation, surface reconstructions, material etc. A famous examples is the contrast of Si(111)-(7x7) vs. Si(111)-(1x1) surface [100, 102]. An other contrast mechanism relies on the fact that there will be a phase shift between plane waves reflected by different terraces on a stepped surface [103]. Among other contrast mechanisms there is of course topographic contrast. It is related to the circumstance that any surface protrusion will distort the electric field. However, the obtained image doesn't reflect the geometry of the surface, although in principle it should be possible to calculate the real morphology from the obtained images. The distortion of the image can be reduced by using higher energies for imaging.

The LEEM setup can aso be used to realize Photo Electron Emission Microscopy (PEEM), were instead of electrons photons are used to excite the sample [104–106]. If the used photons have enough energy they will generate electrons that can overcome the work function and are than imaged with the imaging column of the LEEM. This method is sensitive to the workfunction and gives a chemical contrast.

Using electrons with organic thin films as in this work brings in the problem of beam damage. Although the energy of the incident beam is very small it is in the same region as the band gap of the organic semiconductor, and can therefore lead to desorption or at least degradation of the film. In this study the energy of the beam was therefore carefully selected to be lower than the band gap of 6P. This also explains why at least so far our attempts to obtain PEEM images failed. However, other group have been successful in obtaining PEEM images, by using a shutter in front of the UV lamp that is synchronized with the imaging electronics [107].

Results presented in this work were done in cooperation with the Institute for Solid State Physics, University of Twente, Enschede, The Netherlands. For this studies an Elmitec LEEM III has been used (see figure 2.18).

2.4.5 Thermal desorption spectroscopy

Thermal Desorption Spectroscopy (TDS) allows the investigation of the energetics and kinetics of adsorbed materials on surfaces. For this purpose the adsorbed film is subject to a well defined heating cycle. The desorption rate versus temperature is measured in a UHv system with a Quadrupol Mass Spectrometer (QMS).

TDS was performed by desorbing the adsorbed 6P molecules into a line-of-sight mass spectrometer (QMS 400 quadrupole mass spectrometer (Pfeiffer Inc.) equipped with a magnetic field enhanced cross-beam ion source), which was tuned to the most relevant masses, m = 458 amu (original mass) and m = 61 amu (mass of a cracking product). The latter mass has a much better signal/noise ratio and was therefore used for TDS at small coverages. It has been carefully checked that the m = 61 amu is indeed proportional to the original mass [52]. All TD experiments were done at a linear heating rate of 1 K/s.

The procedure described here is for mica samples. Obtaining TDS spectra from other
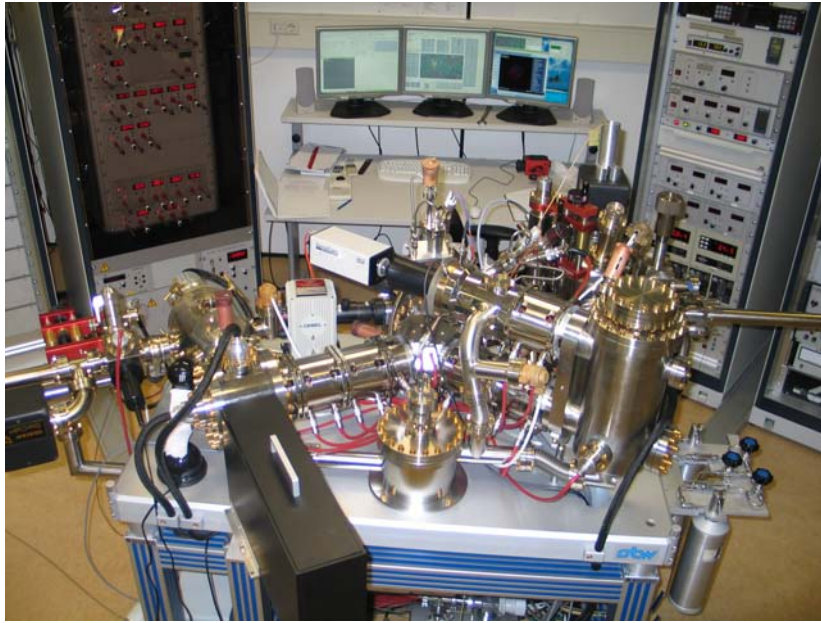
Figure 2.18: Elmitec LEEM III in Enschede.

more conductive materials (like gold) follows the same principle, for details the appropriate literature will be pointed out in the relevant sections. The thin mica sample (10 mm x 10 mm, < 100 µm thick) was attached to a steel plate (10 mm x 10 mm, < 1 mm thick) with tantalum wires (0.25 mm in diameter). The steel plate could be heated via the tantalum wires by resistive heating. The temperature was measured on the backside of the steel plate by a Ni/NiCr thermocouple (see insert in figure 2.19). Because of the poor thermal conductivity of mica, the measured temperature on the backside of the steel plate did not represent the temperature on the mica surface properly and therefore the temperature scale had to be corrected. An uncorrected TD spectrum for a 6P film with 30 nm thickness is shown in figure 2.19. There exist two desorption peaks, one due to the desorption of 6P from the tantalum wires, which were used to fix the sample to the steel plate (see again inset in figure 2.19), and one due to the desorption of 6P from mica. As a first approximation, it is assumed that the multilayer desorption peak should be independent of the substrate and hence desorption from tantalum should occur in the same temperature range as desorption from mica. Therefore the temperature scale was corrected utilizing a linear regression between two characteristic temperatures.

At the adsorption temperature of 300 K both materials will be at the same temperature. When heating up, the mica sample temperature will increase more slowly than that of the steel plate and this will result in a deviation which increases with time. The second characteristic temperature is the starting point of the multilayer desorption of 6P from mica. Keeping in mind the assumption above, the measured 625 K (where desorption from mica starts) can be assigned to 450 K (where desorption from the tan-
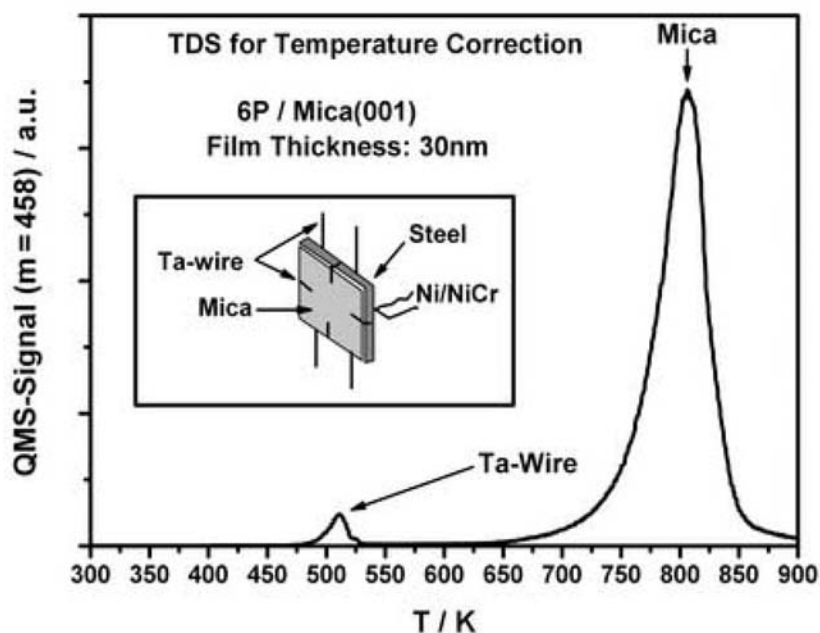
Figure 2.19: Uncorrected TD spectra for a 30 nm thick 6P film on mica(001). The insert shows the setup of the mica samples in the UHV system (from [69]).

talum wires starts). This fits quite well to 6P multilayer desorption from another metal surface, namely Au(111) [52, 78]. All TD spectra shown in the following are displayed with the corrected temperature scale.

All TDS measurements were performed at the Inst. for Solid State Physics, TU Graz, Austria by Stefan Mülleger, Paul Frank and Adolf Winkler.

2.4.6 Photoluminescence spectroscopy

Measurements have been done with a spectroscopic set-up for time-resolved photoluminescence (PL). Excitation was performed with a nitrogen laser ($\lambda_{exc} = 337$ nm, 4 ns pulse duration, and repetition rate of 10 Hz). The emission spectra were recorded using a 300 mm triple-grating monochromator (SpectraPro 2356 from Acton Research Co.) coupled to a highly-sensitive getable intensified CCD camera (PI-MAX (Gen II) from Princeton Instruments) (also called Optical Multichannel Analyzer (OMA), which was synchronized by the electrical trigger of the laser. To increase the signal-to-noise ratio, spectra were accumulated by averaging typically over 300 pulses. Samples under investigation were placed in optical temperature-regulated nitrogen-bath cryostat allowing temperature regulation from 80 K to 350 K. Figure 2.20 shows the principle setup used for these measurements.

All PL measurements were performed by A. Kadashchuk Academy of Science, Kiev, Ukraine at IMEC, Belgium.
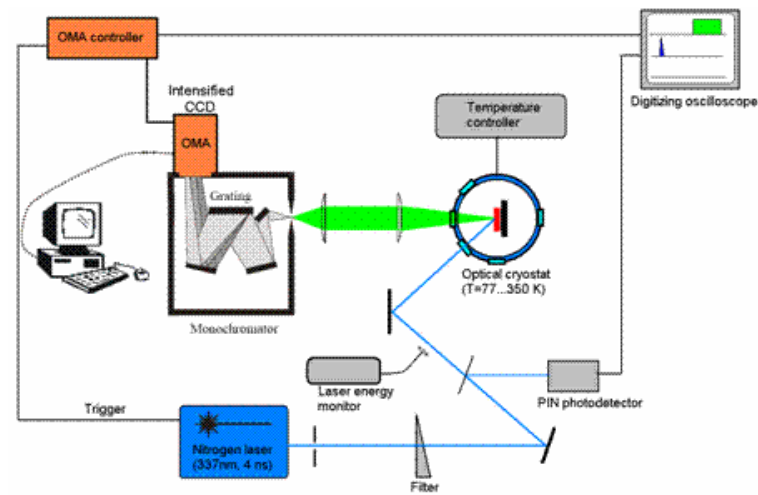
Figure 2.20: Setup used to for photoluminescence measurements (courtesy of A. Kadashchuk).

3 Results

3.1 Para-sexiphenyl on TiO$_2$(110)-(1x1)

This section describes the results obtained for the growth of 6P on TiO$_2$(110)-(1x1). The morphology obtained for room temperature growth will be compared to the morphology obtained at an elevated temperature of 145 °C. LEEM was used to follow in situ the formation of both morphologies as well as the transition from one morphology to the other. The samples for morphological characterization were grown at the Institute of Experimental Physics, University of Graz, Austria in the group of M. Ramsey. The LEEM experiments were performed together with R. van Gastel at the Institute of Solid State Physics, University of Twente, The Netherlands.

3.1.1 Room temperature growth of para-sexiphenyl on TiO$_2$(110)-(1x1)

Figure 3.1a shows AFM results of a 3 nm thick 6P film grown on TiO$_2$(110)-(1x1) at RT. The morphology is characterized by parallel running needles. A cross section (fig. 3.1b) along the main feature in the 2D-FFT reveals a strong peak at 4 µm^{-1}. This
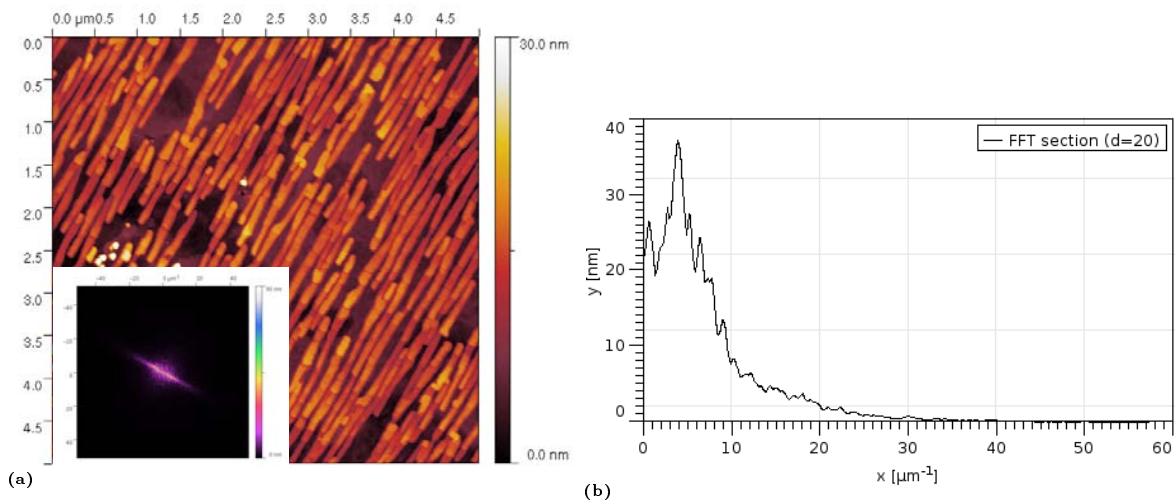
Figure 3.1: (a) 5 µm by 5 µm AFM image of a 3 nm thick 6P film grown on TiO$_2$(110)-(1x1). The inset shows the 2D-FFT. (b) cross section along the main feature in the 2D-FFT. The peak position reveals a distance from needle axis to needle axis of ≈250 nm.

can be interpreted as the mean distance between the needle centers of 250 nm.

The needles are parallel to each other and run along [1$\bar{1}$0] which is perpendicular to the orientation of the oxygen rows on the TiO$_2$(110)-(1x1) surface. The molecules inside the crystals are parallel to the oxygen rows ([001]) and perpendicular to the long needle axis [56].

Figure 3.2 presents a detailed image of individual needles. The cross section in figure 3.2b shows that the chains have a typical height of 14 nm±0.5 nm and a width between 100 nm and 130 nm. The needles are broken into individual segments of 100 nm to 1 μm in length. These segments are most likely of single crystalline nature as can be seen from the section line parallel to the needle. Each segment shows a different but uniform height.

LEEM was used to follow the process of needle formation. Figure 3.3 shows three stages during needle formation. In figure 3.3a the clean TiO$_2$(110)-(1x1) surface can be seen together with some small crystallites (marked green). After 90 s of deposition several parallel needles can be found on the surface. Finally after132 s, a large number of needles can be found on the surface. In figure 3.4 the needle length as well as needle width are plotted versus the deposition time. It is not surprising that the needle width only increases slowly while the length increases rapidly with ongoing deposition. The oscillations in the length but especially the width evolution can be attributed to minute changes in the imaging conditions that will immediately influence the contrast. The reason could be related to changes in the electron optics. But it is more likely related to the fact that the 3D nature of the chains influences the path of the reflected electrons (see also section 2.4.4 for a short explanation of contrast mechanisms in LEEM).

In a different experiment, more material was deposited. The needles continue to grow and start to tile the whole surface. Figure 3.5 shows the resulting AFM image
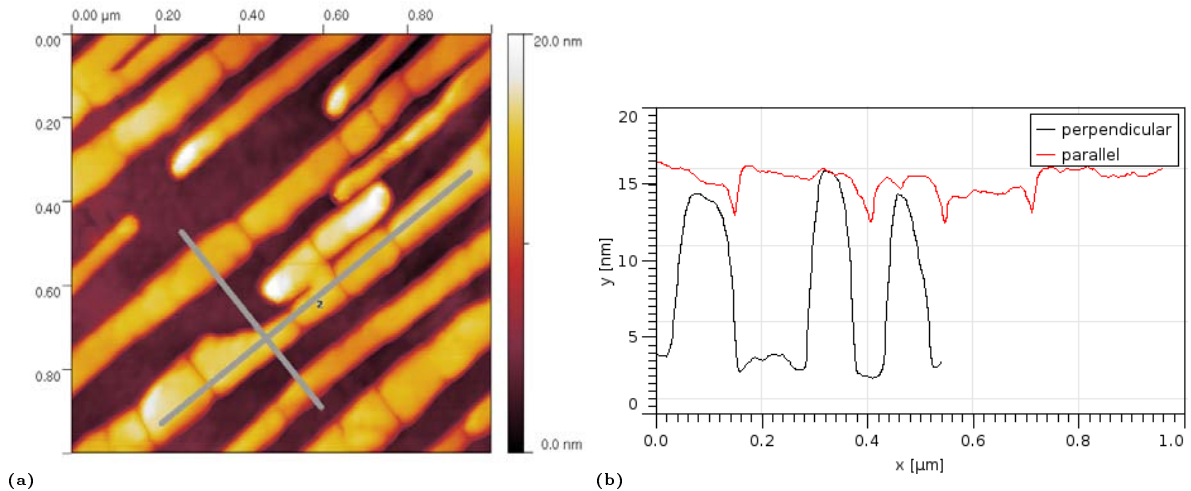
Figure 3.2: (a) 1 μm by 1 μm AFM image. The individual single crystalline segments forming the needle can be identified. (b) cross section perpendicular (black) and parallel (red) to the long needle axis.
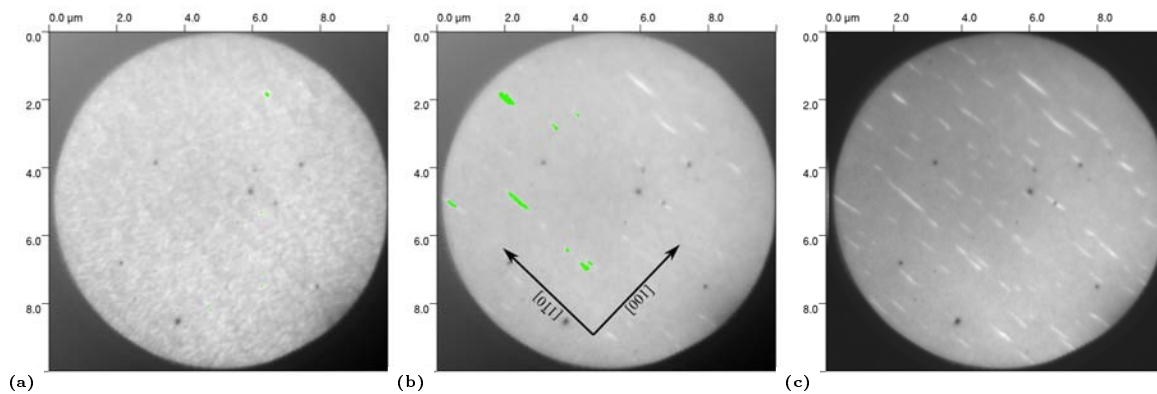
Figure 3.3: 6P needle formation on TiO$_2$(110)-(1x1). (a) first chains appear and are marked with a green mask. (b) after 90 s (the mask is shown for the left half of the image) and (c) after 132 s. (FOV=10 μm)
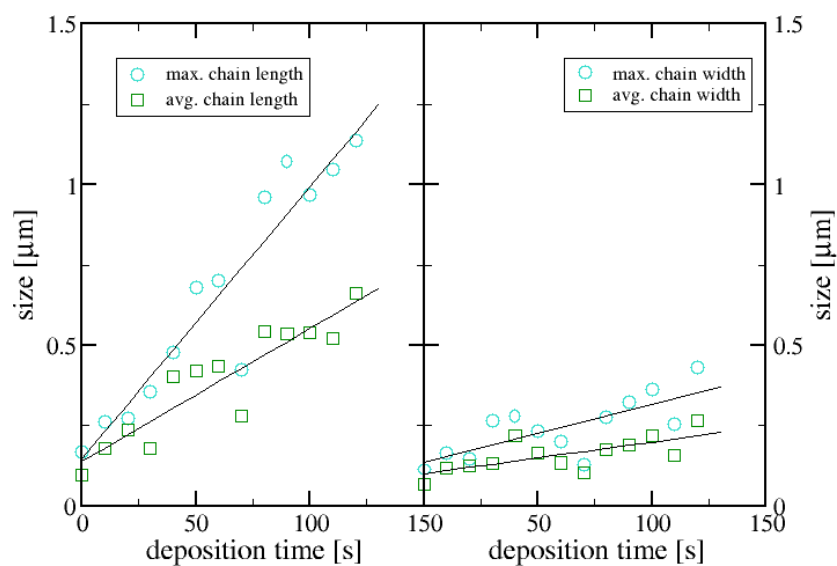
Figure 3.4: Evolution of the lateral 6P needle size during deposition in the LEEM.

after deposition of 35 nm of 6P. The surface is tiled with large interlocked needles. Analysing the 2D-FFT with a cross section reveals a main feature distance in [001] direction (equivalent to the feature size in this case) of 500 nm. A closer look at the morphology shows that these 500 nm wide blocks are made up of two or three highly interlocked needles. The near horizontal stripes in the image result from poor sample handling during the preceding x-ray investigation.

The reason for this highly anisotropic growth lies in a delicate balance between sticking and diffusion anisotropy [55,108]. Due to the near perfect match of the oxygen row distance with the width of a single 6P molecule a high diffusion anisotropy will exist on the surface. The oxygen rows will act as guides for the 6P molecules and allow them to diffuse easily along [001] direction. However, to diffuse along any other direction, especially along [1$\bar{1}$0], the molecules will have to climb over the oxygen rows. This will significantly reduce the diffusion coefficient for this direction. This circumstance alone would promote growth parallel to the oxygen rows. The reason for growth along the oxygen rows is related to a sticking anisotropy. Molecules diffusing along the channels can only interact one with each other with their terminal hydrogen atoms. This will result in a rather weak bond between two molecules. Two molecules diffusing in adjunct oxygen rows can interact with their π-electron system allowing a very strong bond. Figure 3.6 sketches the situation when a molecule will be integrated into an existing chain. The molecule can diffuse quickly towards a chain but the sticking probability on the hydrogen terminated side wall is low. The weakly bond molecules now has enough
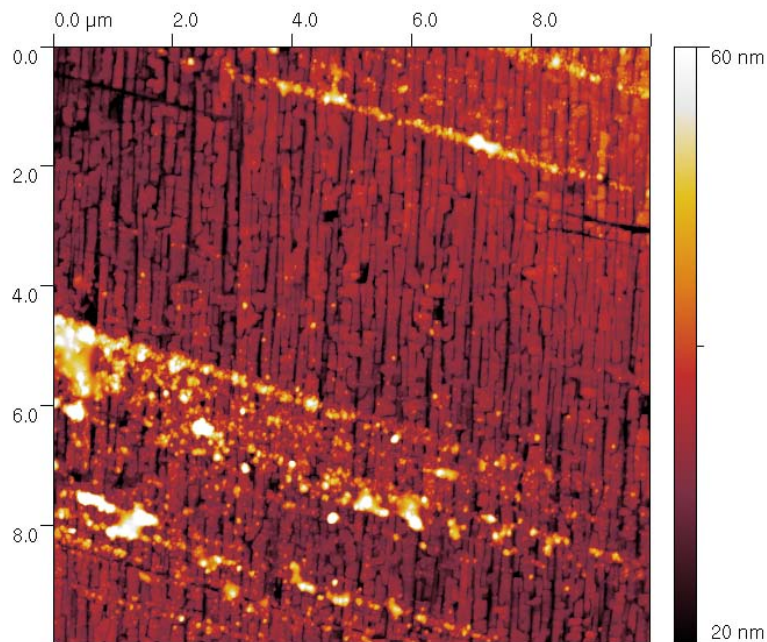
Figure 3.5: 35 nm thick 6P film grown on TiO$_2$(110)-(1x1).

time to diffuse perpendicular to the oxygen rows along the needle and finally reaches the small end of the needle. There it can be easily incorporated into the needle due to strong interaction of the π-electron system with that of the 6P molecules terminating the needle [55, 108].

The single crystalline nature of the building blocks can also be seen in a further LEEM experiment. 6P has been deposited in situ on a clean TiO$_2$(110)-(1x1) surface. Subsequently, the sample was slowly heated while imaging with the LEEM. Figure 3.7 shows a 10 s long sequence taken at 115 °C (image size 2.3 µm). One can see that the marked chain, build from at least three segments, suddenly starts to breakup in two pieces. While the right fragment stays unchanged, the left one gets shorter rapidly. However, after 7 s the process comes to an halt. The middle segment has dissolved and the remaining two parts belong to different crystallite segments of the needle.

Furthermore, it is interesting to observe that the molecules seem to be solely removed from the small end of the chain. No direct information can be obtained if molecules are also removed from the top of the chain as LEEM gives only 2D information. However, as the chain width stays unchanged during the event one can assume that no molecules are removed from the side walls. Looking at the orientation of the molecules inside the chains this is obvious, as one would have to pull a single 6P molecule out of the herringbone structure of the crystallite. On the small side and probably also on the top of the crystallite the molecules have a weaker bond as one of their two π-systems is exposed to the vacuum or is at least partially unsaturated if the molecule is not coplanar with the surface.

3.1.2 High temperature growth of para-sexiphenyl on TiO$_2$(110)-(1x1)

Figure 3.8 shows the stripe pattern that appears after increasing the temperature to 160 °C. The orientation of the stripes is perpendicular to the orientation of the needles, i.e. parallel to the oxygen rows on the substrate. Figure 3.9 shows an AFM image of a
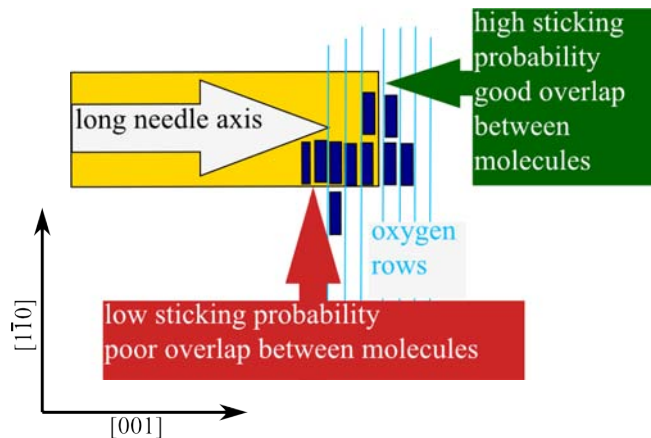
Figure 3.6: Sketch outlining the formation of 6P needles on TiO$_2$(110)-(1x1).
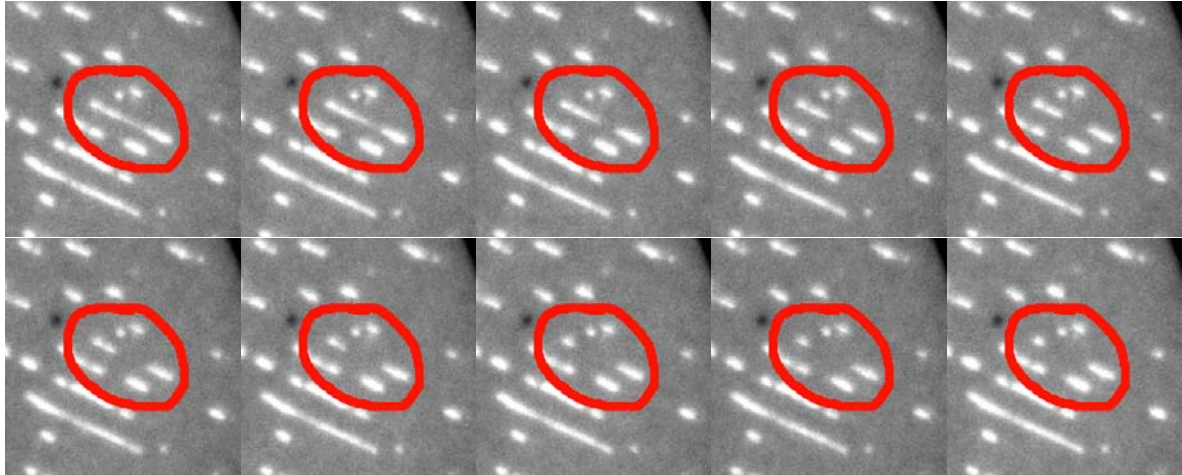
Figure 3.7: 10 s long sequence taken at 115 °C during the heating of 6P needles grown on TiO$_2$(110)-(1x1) at RT. The marked chain is formed by at least three individual crystallites. The middle part disappears in 7 s while the reaming parts of the chain stay unchanged during this event. The long axis of the needles is parallel to the [1$\bar{1}$0] direction. Image size 2.3 μm by 2.3 μm.
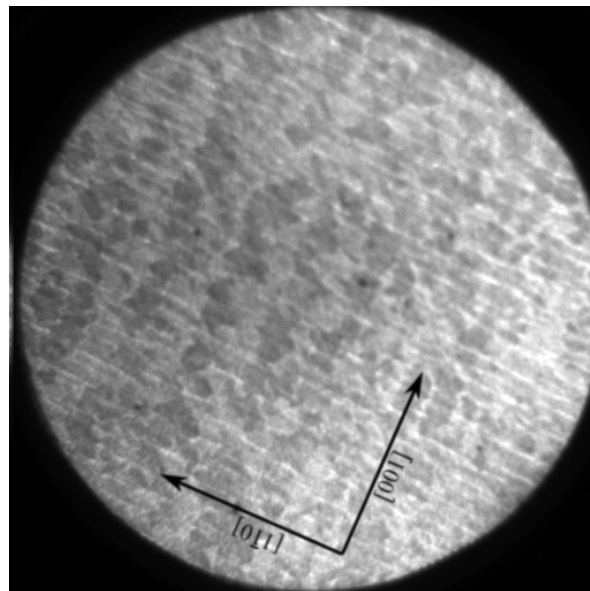
Figure 3.8: LEEM image (FOV 20 μm) of the remaining stripe pattern after heating a film deposited at room temperature to 160 °C. Only a stripe pattern running perpendicular to the direction of the needles is left on the surface.

3 nm thick 6P film grown on TiO$_2$(110)-(1x1) at 145 °C. The morphology shown in 3.9a is characterized by parallel running stripes comparable to the one observed with LEEM. Stripes formed by a continuous layer of 6P with some second and third layer nucleation on top are alternating with stripes of small crystallites. The cross section shown in 3.9b reveals that the continuous stripes are formed by upright standing molecules. The height analysis of the image shows a very uniform height of 2.57 nm±0.02 nm for the individual stripes which is in good agreement with the expected layer height of 2.63 nm for upright standing 6P molecules. The length of the stripes could not be measured with the AFM but together with the LEEM images and the fact that in all obtained AFM images no dead end could be found they seem to extend over at least several 10 μm along the whole crystal surface. The width of the continuous stripes varies between 2 nm and 8 nm.

The continuous stripes are separated by areas covered by small crystallites. Analysing only the height of these parts of the image, the height distribution shown in figure 3.10a can be obtained. The histogram is characterized by peaks at 2.7 nm, 5.4 nm, 8.1 nm, and 10.8 nm. These heights correspond to islands of 1 ML, 2 ML, 3 ML, and 4 ML height they are formed by upright standing molecules. In 3.10b the lateral size of the crystallites for two different data sets is plotted versus the height of the crystallites. One can see that the crystals are always twice as long as they are wide. As can be seen from figure 3.12 the elongation is along mainly the [1$\bar{1}$0] direction.
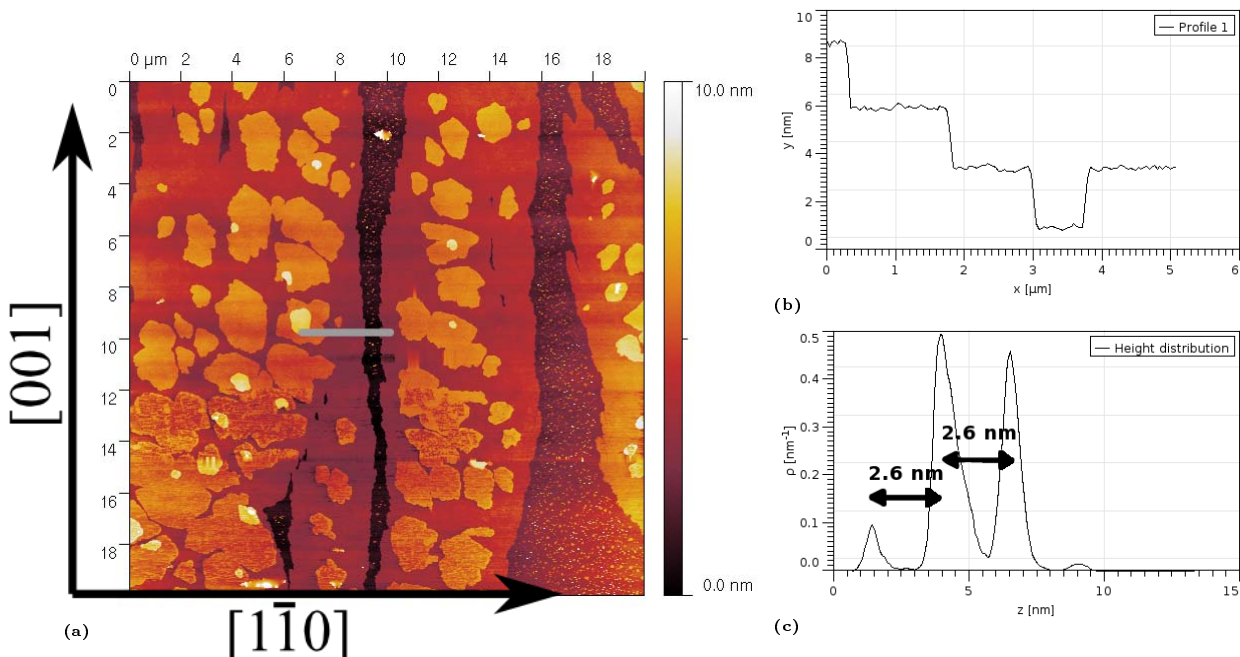
Figure 3.9: 3 nm thick 6P thin film grown on TiO$_2$(110)-(1x1) at 145 °C. (a) 20 μm AFM image. The stripes are parallel to the [001] orientation of the surface. (b) cross section revealing up to three layers of 6P formed by upright standing molecules. (c) height distribution of (a) showing the uniform height of the individual layers of 2.57 nm±0.02 nm.
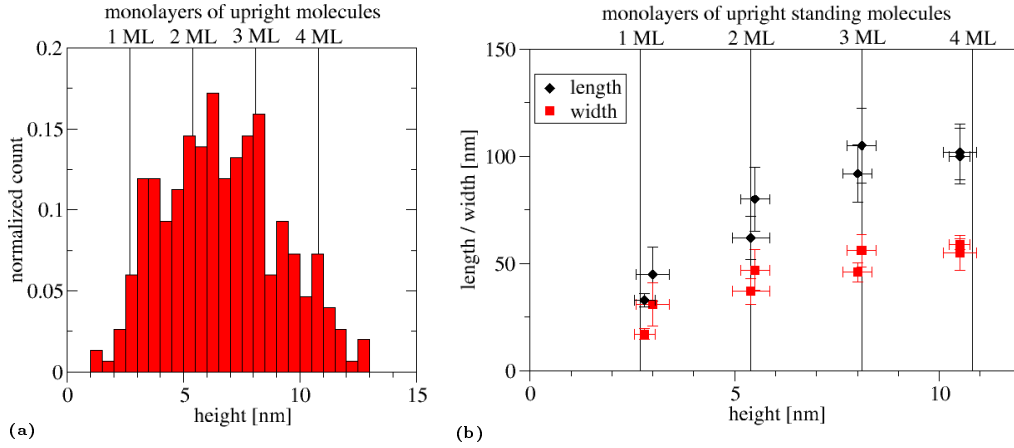
Figure 3.10: (a) height distribution of the crystallites found in one set of the stripes. (b) lateral size of the crystallites plotted versus the height.

Figure 3.11 shows a topographic and the corresponding phase image together with cross sections. In the topographic image the stripes and the islands formed by second layer nucleation are clearly visible. Also the crystallites in the trenches between the continuous stripes are observable. In the corresponding cross section (fig. 3.11c) the steps are clearly visible. The red arrow marks a step between substrate and film whereas the blue arrow marks a step between the first and the second layer of 6P. In the simultaneously recorded phase image only two shadings are visible. While the substrate has a high phase shift, less phase shift is recorded in all areas covered by 6P. In the cross section shown in figure 3.11d, the red arrow marks the position of the topographic step between substrate and the first layer of 6P. The viscoelastic properties of the 6P thin film are different from the properties of the substrate and a strong change in phase shift is the result. The blue arrow marks the position of the morphological step between the first and the second layer of 6P. At this position only a small spike due to the morphological step is visible. The amount of phase shift for the first and the second layer of 6P is the same. This clearly shows that there is no wetting layer between the crystallites [55].

One could argue that a wetting layer of for example lying down 6P molecules would have different viscoelastic properties as the film formed by upright standing molecules and would therefore lead to the same result. However, we never observed phase contrast on samples that had a wetting layer (like the ones presented in section 3.2.1) whereas we observed a strong phase contrast for 6P on other substrates [109]. X-ray investigations also showed no indications for a layer of lying molecules below the film of upright standing 6P. The same study by R. Resel et al. [110] also revealed a number of other interesting facts about the structure of the films. The grazing incidence investigation indicated that the small crystallites are indeed formed by upright standing molecules, and exist only for thin films but disappear for thicker films. In contrast to the large stripes which are formed by four domains with the [20$\overline{3}$] direction azimuthally oriented

(a)

(b)

(c)

(d)
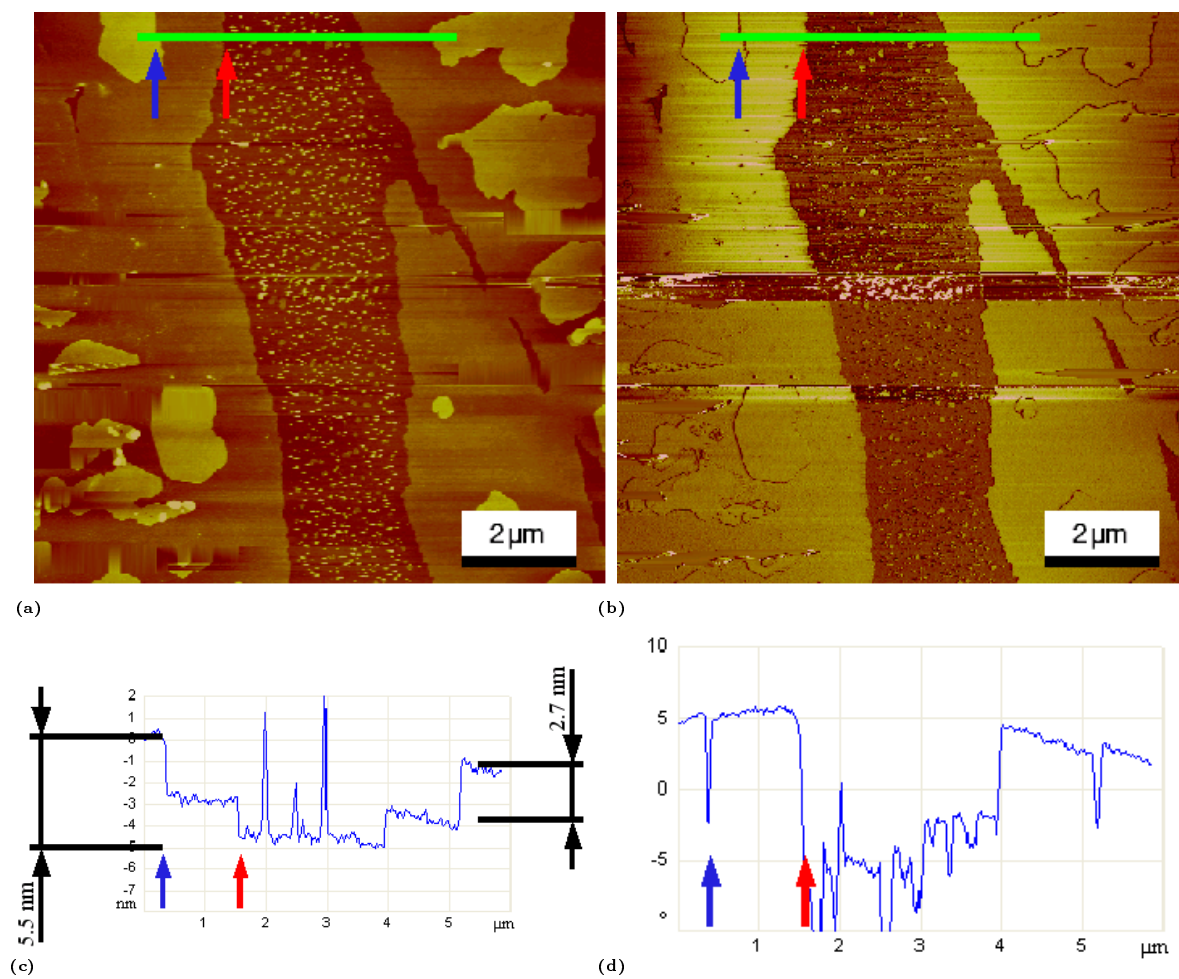
Figure 3.11: Topographic (a) and simultaneously obtained phase (b) image of the stripes. In the corresponding cross section, positions with a topographic but no phase step between two 6P layers (blue arrows) can be distinguished from topographic steps between substrate and film (red arrows).

under 35°, 145°, 215°, and 325° with respect of the principal azimuth of the substrate, the molecules in the crystallites are tilted in the direction of the principle azimuth. The domains in the large stripes are about 300 nm along the [001] orientation and the oxygen rows, whereas they measure only 30 nm perpendicular to the oxygen rows. The long axis of the domains is thus parallel to the stripes.

The formation of this striped phase can be explained by the fact that diffusion along the oxygen rows is much easier than parallel to them. However, in contrast to the RT case presented in the preceding section sticking anisotropy plays practically no role as the molecules are standing nearly upright on the substrate surface (tilted by 17° with respect to the surface normal). This however, might not be true for the small crystallites in the trenches. From the more detailed images shown in figure 3.12 one can see that the crystallites are oriented preferentially along [1$\bar{1}$0]. This can be the result of a slight difference in sticking probability. With the molecules tilted in [001] direction it is easy to see that incorporation is easier on the facets pointing in [1$\bar{1}$0]. The fact that the large islands are formed by four domains oriented diagonal to the principal azimuth suggests that sticking anisotropy does not play a prominent role here.

One of the consequences of this diffusion anisotropy is the difference in shape between the first layer and the subsequent layers. While the first layer shows the described anisotropic shape, the islands nucleated in the second layer on the stripes are already isotropic and do not show any preferred orientation. This can be understood if one takes into account that these islands do not grow on an anisotropic substrate but on layer of upright standing 6P molecules.

An other consequence of this anisotropic diffusion is the fact that the boundary between the two stripes is different along [001] and [1$\bar{1}$0]. Figure 3.12 shows enlargements of the boundary between the stripes. Figure 3.12a shows the boundary perpendicular to the oxygen rows and therefore perpendicular to the fast diffusion direction. Comparing the shape of this boundary to the one shown in figure 3.12b one easily comes to the conclusion that the former is rougher. This can be quantified in terms of the Minkowski boundary lengths given in table 3.1 [98, 111].

Although the left boundary in figure 3.12b is quite rough the boundary along [1$\bar{1}$0] is still 10% longer and 26% longer than the right boundary in figure 3.12b. This can not be explained by the fact that the boundary runs under an arbitrary angle through the image. The elongation of a straight line parallel to the direction of the boundary in

Boundary	S
figure 3.12a	$3.59 \cdot 10^{-3}$
figure 3.12b left	$3.27 \cdot 10^{-3}$
figure 3.12b right	$2.84 \cdot 10^{-3}$
vertical line	$1.95 \cdot 10^{-3}$
diagonal line	$2.76 \cdot 10^{-3}$

Table 3.1: Minkowski boundary length for the boundaries in the striped phase. The values for straight lines are given for comparison.
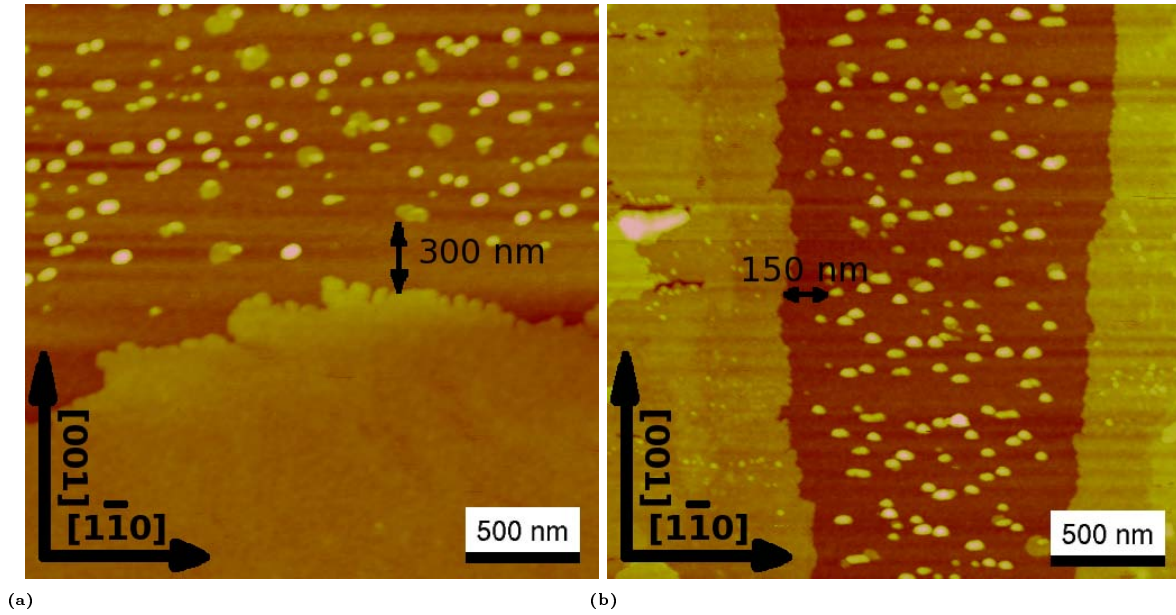
Figure 3.12: Boundary between the continuous stripes and the crystallite covered trenches: (a) perpendicular to the oxygen rows ([1$\bar{1}$0]), (b) parallel to the oxygen rows ([001]). (z-scale: 20 nm)

figure 3.12a compared to a straight line parallel to the right boundary in figure 3.12b is only 2%.

The increased roughness of the boundary perpendicular to the oxygen rows can be explained with the anisotrop diffusion. At edges that run parallel to the oxygen rows, molecules can diffuse back and forth until they find an appropriate position. As soon as the molecule is fixed all other molecules using the same channel on the TiO₂ surface have to line up thus creating a smooth edge.

A further observation is made in figure 3.12. In both images a small stripe is visible where no crystallites can be found. The crystal free area parallel to the oxygen rows has a width of 150 nm while the depleted zone running along the [1$\bar{1}$0] direction is 300 nm wide. This difference can again be explained by the anisotropic diffusion. As molecules can more easily diffuse perpendicular to the terrace edge along [1$\bar{1}$0] a larger capture zone is emptied by the terrace compared to the situation for the boundary parallel to the oxygen rows. Using a method known from Si/Si(001)-(1x2) homoepitaxy [112,113] one can estimate the diffusion anisotropy. The diffusion along [001] is between 4 and 64 times faster than along the [1$\bar{1}$0] direction [108].

3.2 Para-sexiphenyl on mica(001)

3.2.1 Anisotropic growth on mica(001)

This section gives a brief description of previous investigations of films grown by HWE at the Institute of Solid State Physics in Linz. More details can be found in [114,115]. However, the results will be discussed here because of the availability of new additional experiments that allow a more detailed description of the morphology evolution.

Figure 3.13 gives an overview on the change in morphology during the deposition of 6P on mica(001) in an HWE system. The initial stage up to 30 s is characterized by the formation of small uniformly sized crystallites. The evolution of the crystallite size is plotted in figure 3.14a. From the diagram it is clear that the crystallite size increases quickly during the first few seconds and saturates after approximately 30 seconds. This behaviour of the size evolution is typical for a strain controlled growth mechanism [72,116]. When more material is added instead of further increasing the size of existing crystallites a new entity is formed. This results in a nearly linear increase of the crystallite density by a factor of four from $\sim$10 μm^{-1} to $\sim$35 μm^{-1} as shown in figure 3.14b.

After roughly 35 s a critical density of crystallites is reached and suddenly the formation of chains starts. Figure 3.13b and 3.13c shows two snapshots of this intermediate growth stage after 45 s and 55 s respectively. The chains formed are all parallel to each other. Due to the particularities of the mica unit cell only two orientations can be found on the sample (see figure 2.3 on page 18 and [66]).

The evolution of chain size is printed in 3.15a. The length distribution of the chains found in the intermediate stage is analyzed in the histograms shown in figure 3.15b. The increase in chain density is also presented in figure 3.14b. From this diagram one can also see that the formation of chains stops the increase of crystallite density.

Formation of 1D chains

The formation of the 1D chains can be divided into three stages. Initially the surface is covered with small randomly distributed crystallites. From the size evolution one can conclude these crystallites are most likely strain controlled [72,116]. With ongoing deposition the density of crystallites increases until a critical density is reached.

The roughness of a clean mica(001) surface is 0.1 nm. However, the roughness of the surface that is not covered with chains or crystallites after 6P deposition is 0.5 nm. This increase in surface roughness is the result of an additional closed layer of 6P on the sample surface. TDS, carried out by P. Frank, on samples grown under similar conditions confirms this assumption. Figure 3.16 shows the obtained desorption spectra for different nominal film thicknesses. For small coverages (curves a) and b)) a desorption peak is found at 550 K. This peak saturates at mean coverage of about 0.2 nm to 0.3 nm. Taking into account the Van der Waals dimension of 6P of 0.35x0.67x2.85 nm^3 [9], this coverage corresponds to 1 ML of rather strongly bound flat lying molecules. For higher coverages (curves c) and d)) a second peak arises. This peak at 480 K does not sat-
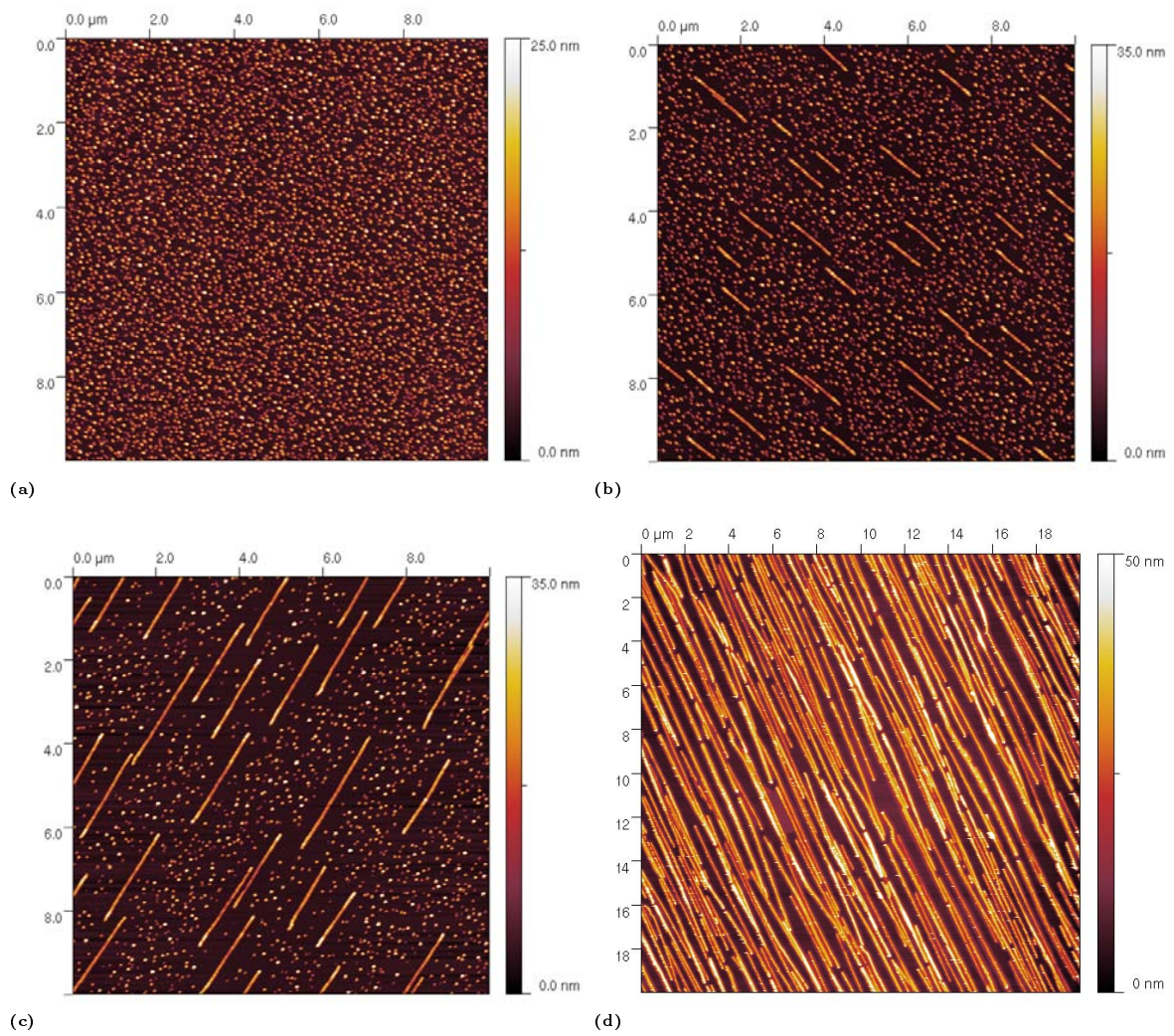
Figure 3.13: Growth stages of 6P on mica(001). Morphology after (a) 30 s, (b) 45 s, (c) 55 s, and final growth stage (d) after 6 min of 6P deposition. Note different z-scales for the images and the larger scan size in (d).
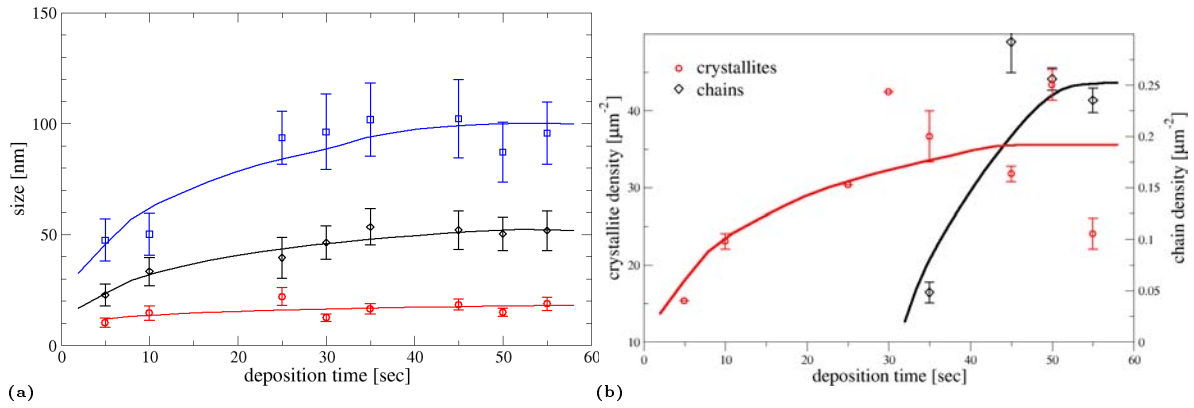
Figure 3.14: Evolution of feature size and density for HWE grown 6P on mica(001). (a) change of crystallite size with ongoing deposition. (b) change of feature density with ongoing deposition.
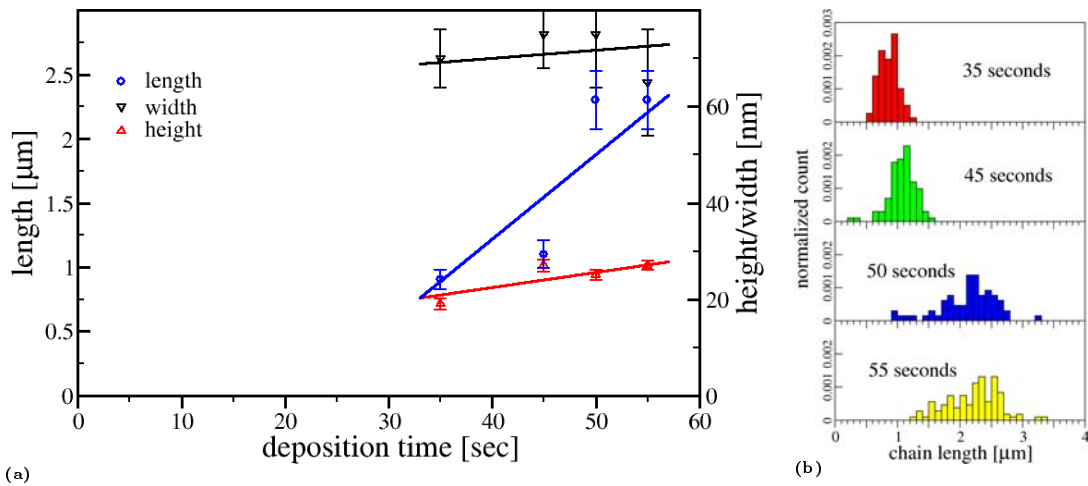

Figure 3.15: Evolution of chain size and density (a) and histograms for chain length distribution in the intermediate growth stage (b).

urate. The common initial slope and the sharp drop at the trailing edge of the peak is a clear indication for zeroth order desorption. This desorption can be attributed to molecules coming from the crystallites and chains sitting on top of the 1 ML thick wetting layer of lying molecules. These molecules are also lying but are weaker bound. This combination of wetting layer plus 3D islands is known as SK growth mode. [69, 115]

Careful analysis of the images from the intermediate growth stage shows that the chains are surrounded by a denuded zone. In figure 3.17a, such a denuded zone is drawn around one chain. In the lower left of the image a rectangle of the same size is drawn in an undisturbed region of the sample. The number of crystallites found in the lower left rectangle is sufficient to form a chain with the – for this film thickness typical – length of 1 μm. The 3D representation of an individual chain shown in figure 3.17b shows the internal structure of the chain.

The formation of the chains is the result of a spontaneous rearrangement process of the crystallites. The process is triggered when the strain fields of the individual crystallites start to overlap at the critical density. The release of the strain in the wetting layer leads to the formation of different domains. The created domain boundaries are straight lines in the direction of the chains in the ordered wetting layer. These can now act as nucleation centers where the crystallites do not repel any more but attach and from chains. The uniform length distribution for low coverages is a result of the reduction of crystallite density through the formation of a sufficient long chain. When more 6P is deposited new crystallites form until the critical density is reached again and either a new chain forms or an existing chain grows in length. Coalescence of
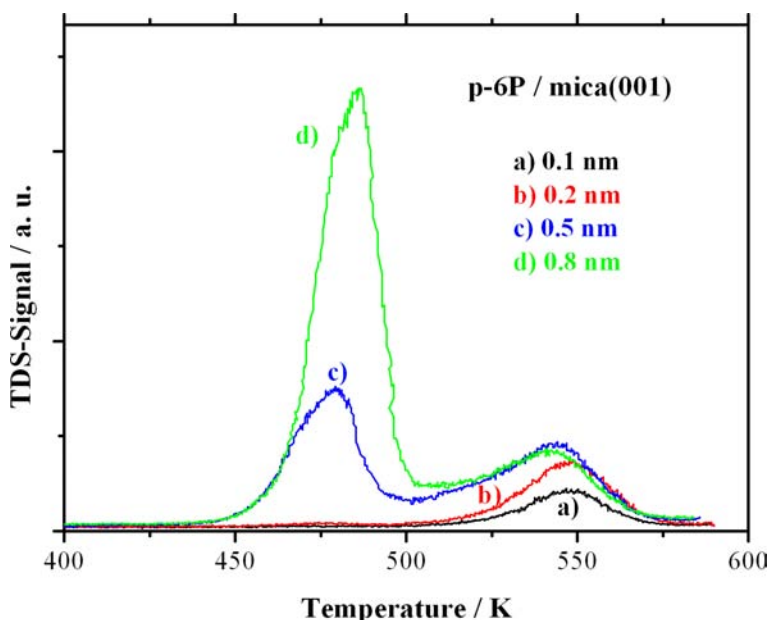
Figure 3.16: Thermal desorption spectra for 6P on mica(001). The adsorption temperature was 360 K, and the heating rate during desorption 1 K/s. The mean thickness of the individual films as measured by QCM technique is indicated. From [115]

existing chains with other chains at higher coverages leads to a broadening of the chain length distribution. The uniform width and height of the chains is a result of the strain controlled growth of the crystallites. An annealing experiment described in [114, 115] gives further evidence for this scenario.

It is obvious to look for an explanation for the chain direction that lies in the nature of the substrate. Campbell et al. [67, 68] show that immediately after cleavage one can find 1 Å high steps most likely coming from K^+ ion domains on the surface. This domains exhibit straight edges and could therefore in principle act as guides for the chain formation. However, no preferred orientation is given and the stability of such a domain is less than ≈ 10 min, which is shorter than the typical transfer time. A more obvious explanation is given by structural investigations of 6P on mica(001). Plank et al. [48, 66] show that 6P grown on mica(001) has a strong epitaxial relationship to the substrate. The same three epitaxial relationships are identified for both the freestanding crystallites and the crystallites forming the chains. However, regarding the orientation of the molecules on the surface they differ only slightly. All the molecules are oriented more or less parallel to each other and parallel to the substrate. Together with the strong sticking anisotropy this leads to the fact that the easy growth directions of a 6P crystallite are in a plane perpendicular to the surface. The molecules prefer to attach with their π-orbital overlapping as much as possible. Therefore, the crystallites growth predominantly in the plane of the herringbone layer but much slower perpendicular to it. The final direction of the chain is determined by the direction of the domain boundaries in the wetting layer, which is perpendicular to the molecular orientation.

(a)   (b)
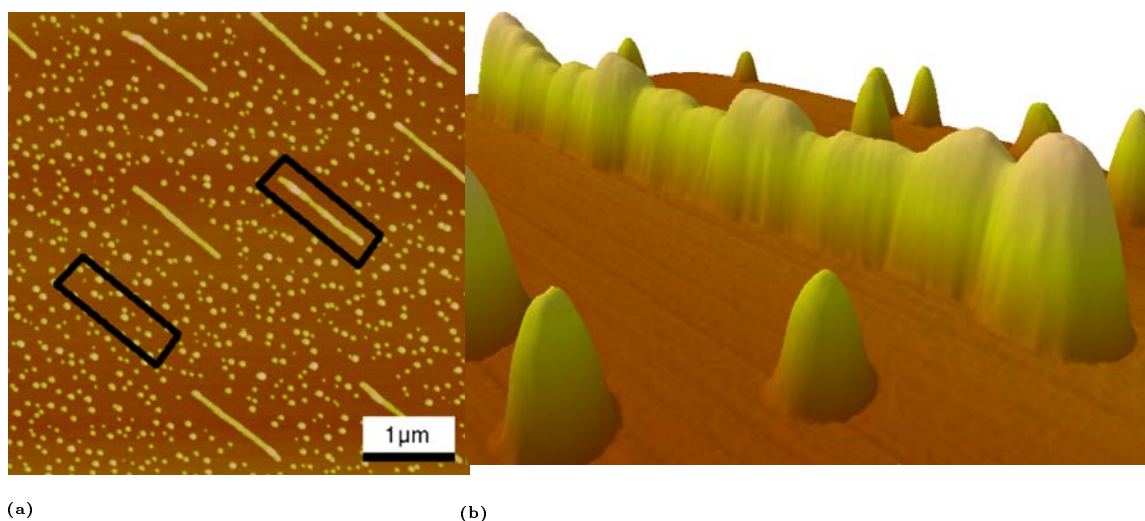
Figure 3.17: The chains are formed by a rearrangement process of individual crystallites into chains. (a) The amount of material in the lower left rectangle is sufficient to form a chain similar to the one in the upper right rectangle. (b) 3D representation of a single 6P chain revealing the internal structure of the chain.

3.2.2 Influence of the growth method

Figure 3.18 presents an overview of the morphology of 6P grown on mica(001) by OMBE [117]. AFM images for four different film thicknesses all grown at 90 °C are presented, namely 1 nm (3.18a), 2 nm (3.18b), 4 nm (3.18c), and 6 nm (3.18d). The substrates where cleaved under ambient conditions and than transfered immediately into the UHV chamber to reduce contamination. It has been tried to stay close to the procedure used for the HWE prepared films, however due to the more complex setup in a UHV OMBE system longer transition times are unavoidable. Before deposition, the samples where heated to 200 °C for 60 min at a base pressure of the chamber of $5 \cdot 10^{-10}$ mbar. This cleaning step is expected to remove airborne contaminations from the sample surface. However, traces of carbon, carbon oxides, and hydrocarbons are left on the sample surface after this treatment [69,118].

The films are characterized by a coexistence of small crystallites and kinked needles. With increasing film thickness their length and density on the surface increases while their width and height stay nearly constant.

Figure 3.19 shows the evolution of chain size with increasing film thickness. In figure 3.19a the average chain length, width, and height are plotted versus the film thickness. While the first increases dramatically from 160 nm to nearly 2 μm the height stays at it's initial value of roughly 30 nm. Also, the chain width only increases slightly from 55 nm, for the 1 nm thick film, to 150 nm for the 6 nm film. Figure 3.19b presents the evolution of the chain length distribution with increasing coverage. With ongoing deposition and therefore longer chains, a significant broadening of the chain length distribution can be observed. The characteristic parameters of the Gaussians used to create the lines to guide the eye are given in table 3.2. Its clear that OMBE can reproduce the main characteristic of the chain formation observed in HWE growth presented in the preceding section.

One of the obvious difference is the fact that the OMBE grown chains are formed by long and straight segments. Very small pieces of these segments are also forming the chains found in HWE growth, however the segments in OMBE grown films are much longer. Figure 3.20 shows a 2 μm AFM image of a 4 nm thick film (from the same sample as figure 3.18c) and three cross sections along segments of one chain. The chains are not straight but consist of a number of long straight and smooth segments

film	μ	σ
	nm	nm
1 nm	35	3
2 nm	740	60
4 nm	400	120
6 nm	1900	330

Table 3.2: Parameters for the Gaussians to fit the chain length distributions presented in fig. 3.19b. The raw data was obtained from the films presented in fig. 3.18
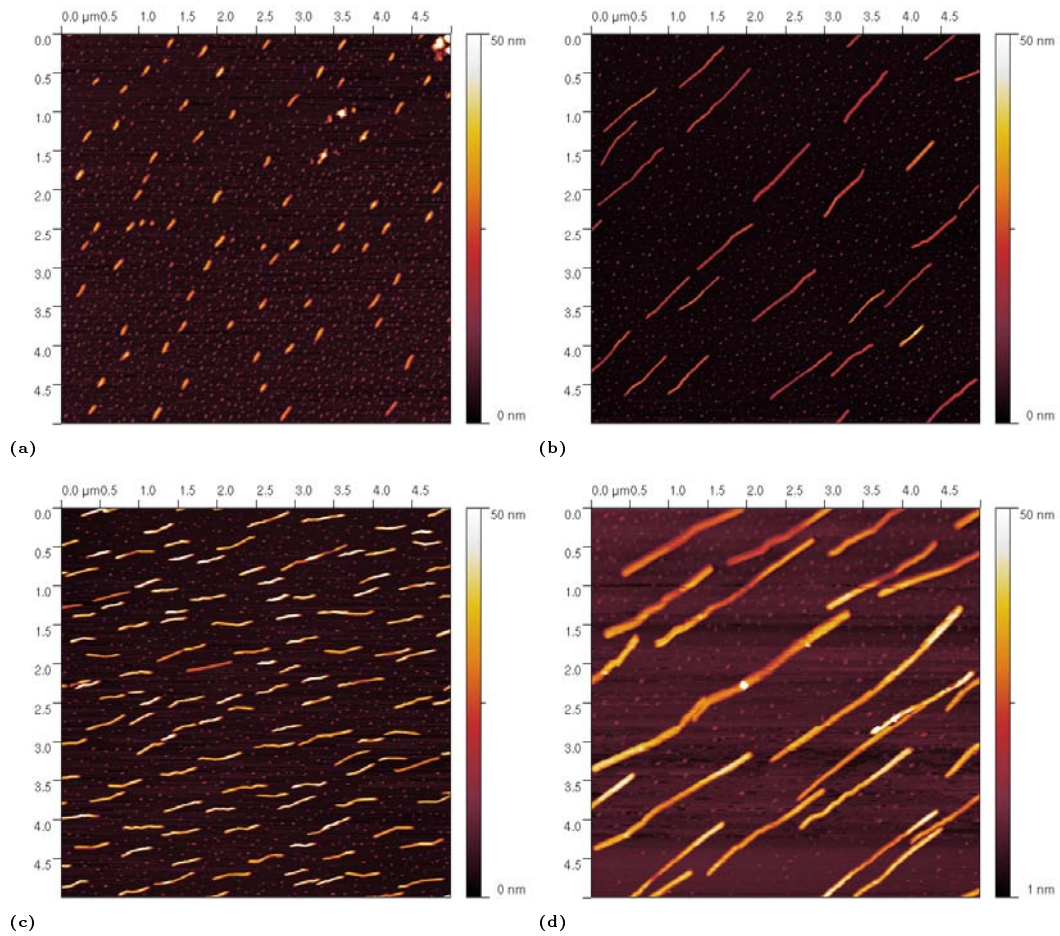
Figure 3.18: 6P films on mica(001) grown by OMBE at 90 °C after a preheating step at 200 °C for 60 min The film thicknesses are: 1 nm for (a), 2 nm for (b), 4 nm for (c), and 6 nm for (d).

that are tilted with respect to each other. This can lead to either zig-zag chains or chains that slowly turn in one direction. By carefully analyzing the direction of the individual segments three dominant directions separated by about 18°could be identified. Furthermore, from the cross sections it is clear that the individual segments show no internal structure. Very long straight OMBE grown 6P needles without an internal grain structure observable by AFM have also been reported from other groups [119].

This is different from the films grown by HWE (see section 3.2.1), where straighter chains with a pronounced internal structure are found. However, figure 3.21 shows a 2.5 µm AFM image of a 1 nm thick 6P thin film grown on mica(001) at room temperature in a different UHV system. Here, the well know coexistence of chains and crystallites is clearly visible. The detailed processes leading to chains formed by small crystallites as presented in this work or uniform more single crystalline needles (especially those shown by Balzer and coworkers) is not clear. Nevertheless the following tendencies can be observed:
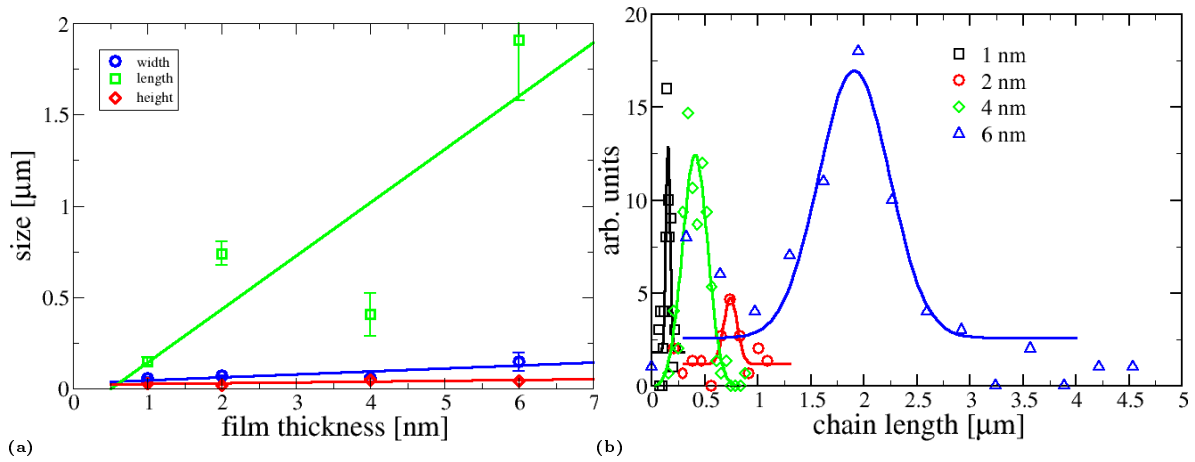
Figure 3.19: (a) Evolution of chain length, width and height with film thickness in OMBE grown 6P films presented in figure 3.18. The chain length increases while chain height and width change only slightly. (b) the corresponding chain length histograms for the investigated films.
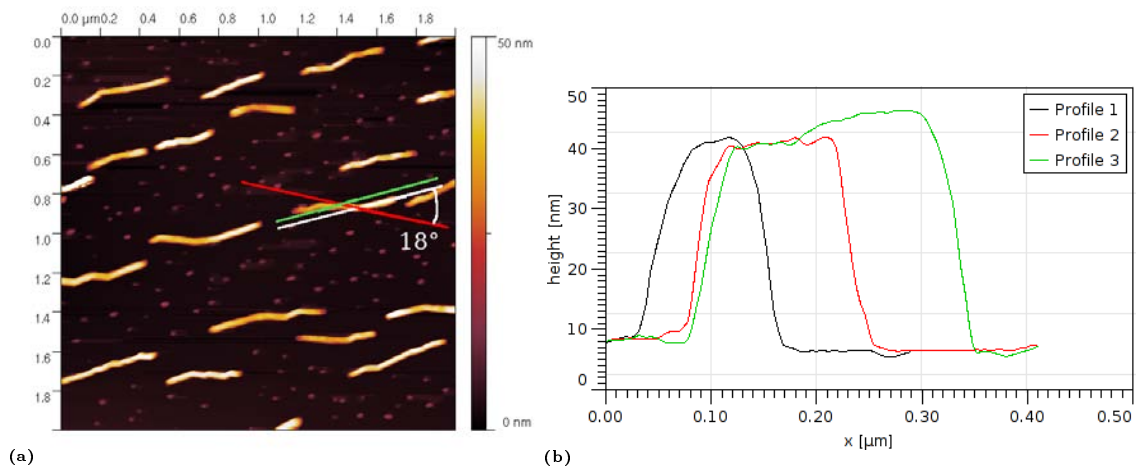
Figure 3.20: Section analysis of a 4 nm thick 6P film grown at 90 °C by OMBE. (a) 1 µm by 1 µm AFM image. (b) cross sections along the lines marked in (a).

- cleaner growth conditions (as in OMBE) promote the growth of single crystalline needles or needles formed by only a few segments.

- HV growth conditions (as in HWE) lead to more segmented needles and ultimately to the observed crystallites chains.

The AFM images suggest that the kinked chains are composed of larger crystallites than the straight HWE grown ones. This is confirmed by time resolved PL investigations carried out by A. Kadashchuk. Figure 3.22 shows steady state PL obtained at 80 K and 293 K. Both spectra are characterized by a main band at 399 nm and vibronic progressions at 420 nm and 445 nm. The broad structureless band at around 480 nm observed earlier [120] is missing. Together with time resolved data presented there, this band can be interpreted as a result of structural defects. The absence of this band here, confirms the high quality of the OMBE grown chains.

3.2.3 Influence of the growth temperature

To investigate the influence of growth temperature on the film morphology a number of samples has been grown. The films were prepared at different growth temperatures and thicknesses in different UHV systems.

Figure 3.23a shows a 2 nm thick 6P film grown at 200 °C. The mica sample was cleaved under ambient conditions and than subject to a 60 min preheating step at 200 °C to remove airborne contaminations. The inset shows a 2 nm film grown at 90 °C discussed earlier (see section 3.2.2 on page 57 and figure 3.18). Figure 3.23b shows the distribution of chain length, height, and width. Comparing these results with the films presented in sec. 3.2.2 on page 57 the consequence of an increased growth temperature is obvious. The chain width changes only within the error bars from 70 nm to 60 nm.

(a)   (b)
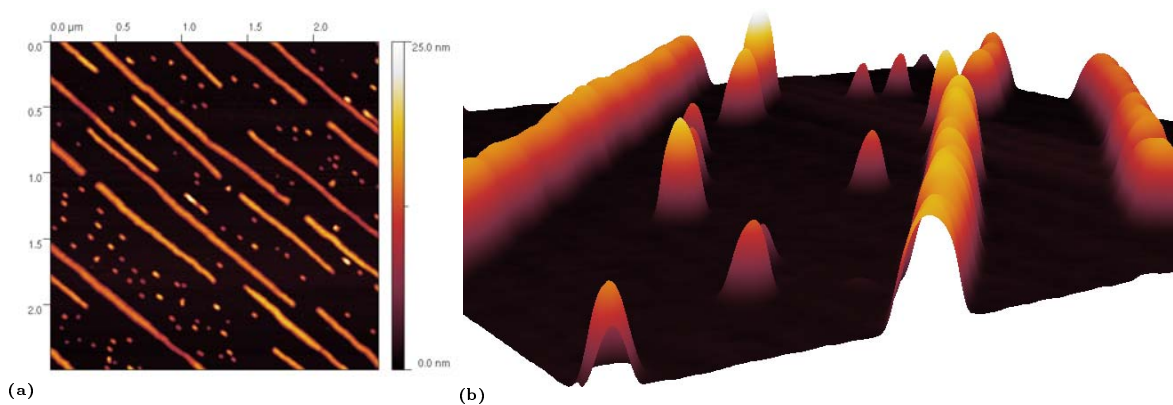
Figure 3.21: Chains and crystallites in OMBE 6P films. 1 nm thick 6P film grown at room temperature under UHV conditions. (a) overview of the morphology. (b) 1 μm by 1 μm 3D representation of the same film showing the individual crystallites as well as an internal structure similar to the one observed in HWE grown films. (z-scale: 25 nm)
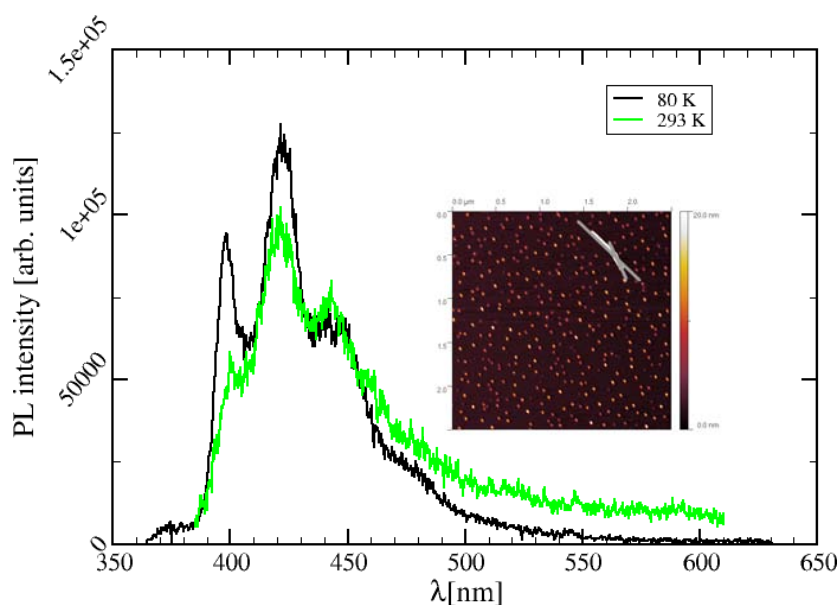
Figure 3.22: Steady state PL spectra obtained from an OMBE grown 6P film at 80 K and 293 K. The 10 nm thick film was grown at 130 °C. The inset displays the corresponding morphology. Measurement performed by A. Kadashchuk.

However, the change in height and length of the chains is dramatic. While the length of the chains is reduced from 740 nm to 220 nm the height increases from 18 nm to 45 nm. Surprisingly, the film grown at 200 °C exhibits a higher crystallite density ($125\ \mu m^{-2}$ at 200 °C versus $90\ \mu m^{-2}$ at 90 °C).

The UHV system in Leoben does not allow cooling of the samples. To access this interesting part of the growth a series of 6P thin films was grown in an UHV system of the Institute of Solid State Physics at the Graz University of Technology. Details on the used vacuum system can be found in [9]. Figure 3.24 shows the obtained film
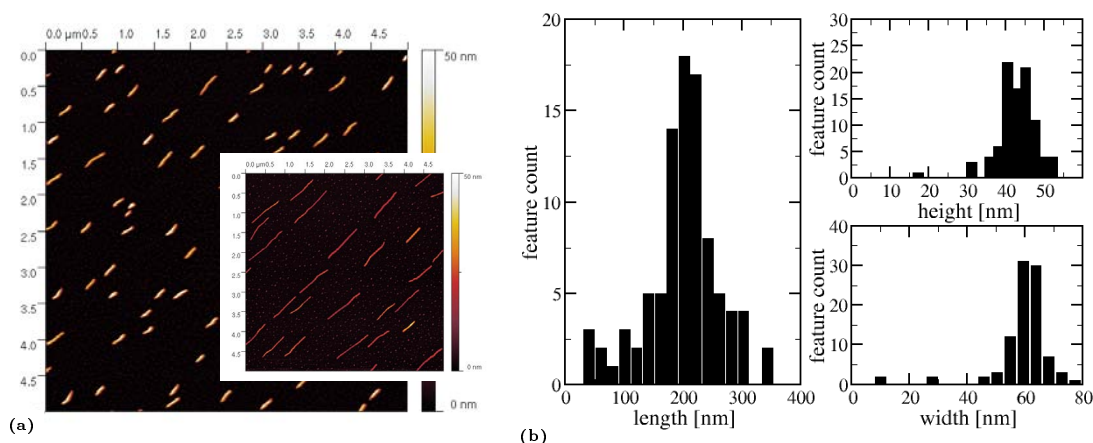
Figure 3.23: (a) 2 nm thick 6P film grown at 200 °C. The inset shows a 2 nm thick 6P film grown at 90 °C. (b) chain size distribution for the film presented in (a).

morphologies. The films were grown at $-160\,°C$, $90\,°C$ and $200\,°C$. The film thickness is 7 nm in all cases.

The film grown at the lowest temperature ($-160\,°C$ see fig. 3.24a) shows a fine grained structure. The grains are elongated along the vertical direction of the image. A grain analysis a described in section 2.4.2 gives an average grain dimension of 100 nm x 200 nm. The rms-roughness of the film is 5.9 nm. The elongation is the result of the usually observed anisotropy in 6P growth. Even at such low temperatures the driving force to align the molecules with their π-systems parallel is strong enough to allow the formation of crystallites with an aspect ratio of 2. Increasing the temperature to $90\,°C$, a morphology comparable to the one presented earlier is achieved (see figure 3.18). Figure 3.24b shows the resulting morphology. The width of the chains is around 80 nm, the height is 35 nm and the length between $1\,\mu m$ to $1.5\,\mu m$. From the FFT presented in fig. 2.13a a typical chain to chain distance of 140 nm can be calculated. Increasing the growth temperature up to $200\,°C$ results in a morphology as presented in fig. 3.24c. The 6P chains are 100 nm wide, 70 nm high, and several μm long. A reliable value for the length can not be given because some of the chains already start to coalesce. For the same reason the value given below for the chain density is only a rough estimate. In general the increased mobility at higher temperatures allows the molecules two avoid the unfavorable substrate. The result is an increase in chain height and a reduction of the feature density from $200\,\mu m^{-2}$ for the low temperature film to $10\,\mu m^{-2}$ for the room temperature film and $2.5\,\mu m^{-2}$ for the high temperature film. This temperature induced change of morphology is quantitatively resembles the one observed for HWE grown 6P thin films for temperatures between $90\,°C$ and $240\,°C$ [121].

The results obtained for films grown by the Graz group and the results measured for films grown in the UHV system at the Institute of Physics, University of Leoben are comparable. Typical growth system depended influences like residual gases that act as contaminations or effects due to geometric peculiarities can therefore be excluded as the reason for the observed behaviour. In fact, the formation of chains composed of individual crystallites seems to be *the* typical morphology for this film substrate combination.

3.2.4 Influence of surface modification

The growth of 6P on mica(001) is to a great extend controlled by the strong surface dipole field that interacts with the large π-electron system of the 6P molecule. Two different approaches have been chosen to reduce this interaction between the substrate and the film. Two attempts have been made to control the growth. First, via addition of a surfactant and later on also ion bombardment has been used to change the surface of the substrate in a way that allows the growth of 6P without a strong film substrate interaction. This part of the investigation was motivated by the fact that for high quality mica surfaces the sample has to be cleaved under ambient conditions. UHV cleaving is not reliable enough to achieve a reproducible surface with large terraces. However, during the ex situ cleaving contamination is unavoidable and the influence of different transfer strategies is unclear.
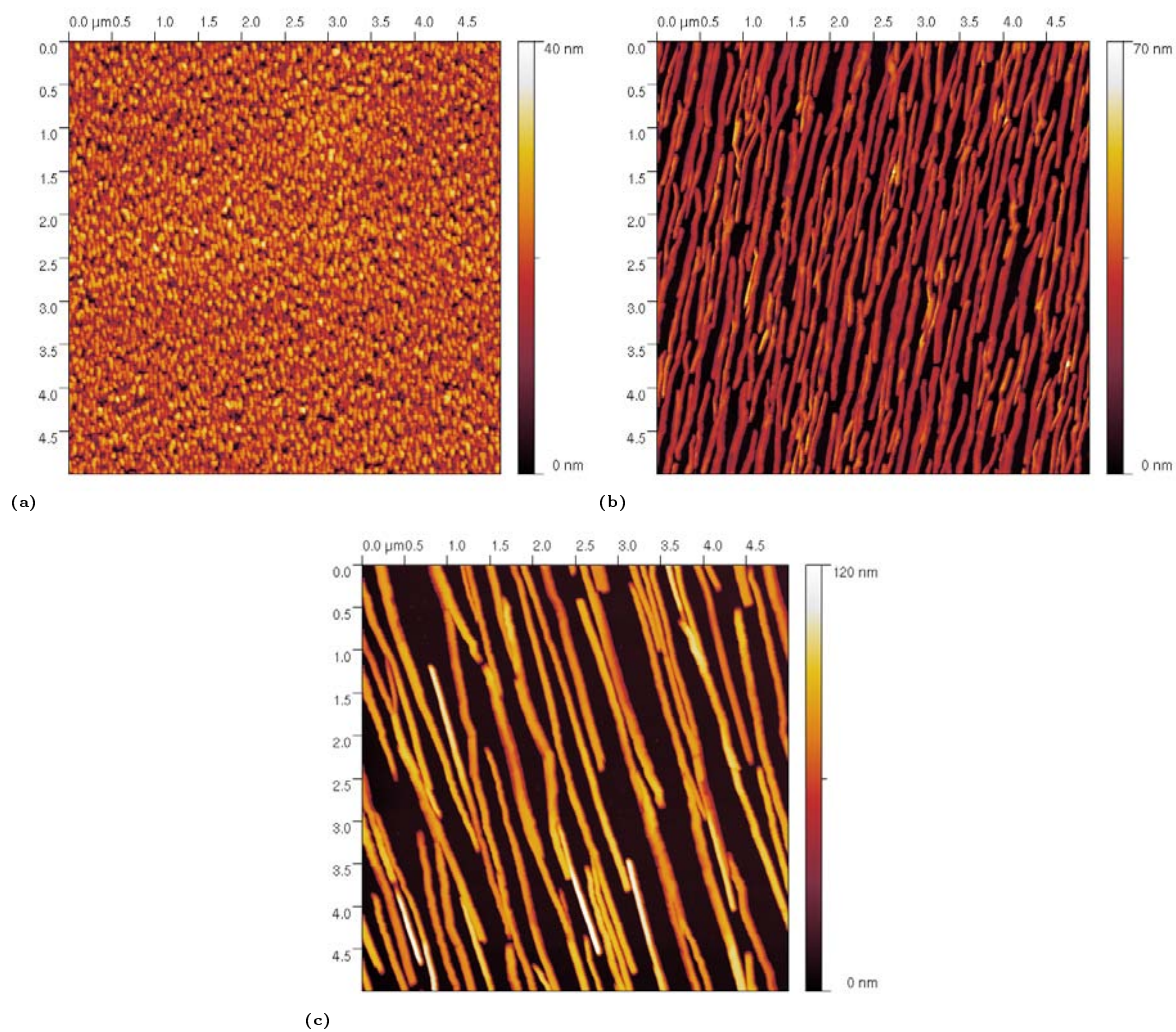
Figure 3.24: 7 nm thick 6P films grown at (a) $-160\,°$C, (b) $90\,°$C, and (c) $200\,°$C. The series demonstrates the change in morphology with increasing growth temperature from a granular morphology (a) into the typical morphology characterized by needles (b) and (c). From (b) to (c) the chain density is reduced by a factor of 5 while the chain height is increased due to the higher mobility.

Modification by surfactants

The samples in the previous sections and the following sections were all cleaved under ambient conditions and then transfered quickly into the HV/UHV chambers for growth. Quickly in this context means that the time between cleaving and start of the pumping system was between 10 min and 20 min. Figure 3.25 presents a series of AFM images obtained from contaminated samples. After cleavage the samples were stored under clean ambient conditions for times between 48 h and 60 h [117].

After insertion into the UHV system the samples were subject to a preheating step for 5 min at 300 °C. 6P films were then grown at room temperature with a growth rate of 1 nm/min to the desired thickness of 2 nm (fig.3.25a), 10 nm (fig. 3.25b), and 15 nm (fig. 3.25c). The result of the long exposure to ambient conditions is obvious. In addition to the well known parallel running chains, laterally extended islands are formed. A cross sectional analysis reveals a height of these islands of 2.6 nm. This corresponds well to the length of an individual 6P molecule of 2.7 nm. The behaviour of the crystallite chains with increasing film thickness is similar to the results obtained earlier (see sections 3.2.1 and 3.2.2).

To confirm the observations regarding the molecular orientation the samples were investigated with x-ray diffraction. Figure 3.26 shows the result of a specular scan obtained at the G2 beam line at the CHESS, Cornell University, Ithaca, USA. The measurement taken from the sample shown in figure 3.25c shows the $6P(11\bar{1})$ peak originating from molecules with their long axis parallel to the surface. Using the Scherer equation

$$D = \frac{\lambda}{\beta \cos \Theta} \tag{3.1}$$

one can calculate the minimum crystallite size in the growth direction D, using the FWHM of the peak β, the cosine of the half of the diffraction angle Θ, and the wavelength λ. The resulting minimum size in vertical direction of 10 nm is in excellent agreement with the chain height measured by AFM. Figure 3.27 shows two cross sections obtained from the same sample. While the average chain height is 16 nm the minimum chain size is only 12 nm. Figure 3.27c clearly shows the internal structure described in detail in section 3.2.1.

Figure 3.28 shows the specular scan of a 10 nm thick film (see figure 3.25b for the morphology). The shoulder at $\Theta = 17.512°$ corresponds to the $6P(006)$ peak of sexiphenyl indicating upright standing molecules. The large peak to the left corresponds to mica.

For further understanding of the process, two samples were cleaved under ambient conditions and stored for 2 weeks. Figures 3.29a and 3.29c show the film morphology after a 5 min cleaning step at 300 °C and 500 °C respectively and evaporation of a 1.3 nm thick 6P film at room temperature. Two features can be observed immediately

1. large flat terraces of uniform height

2. small circular features of different size
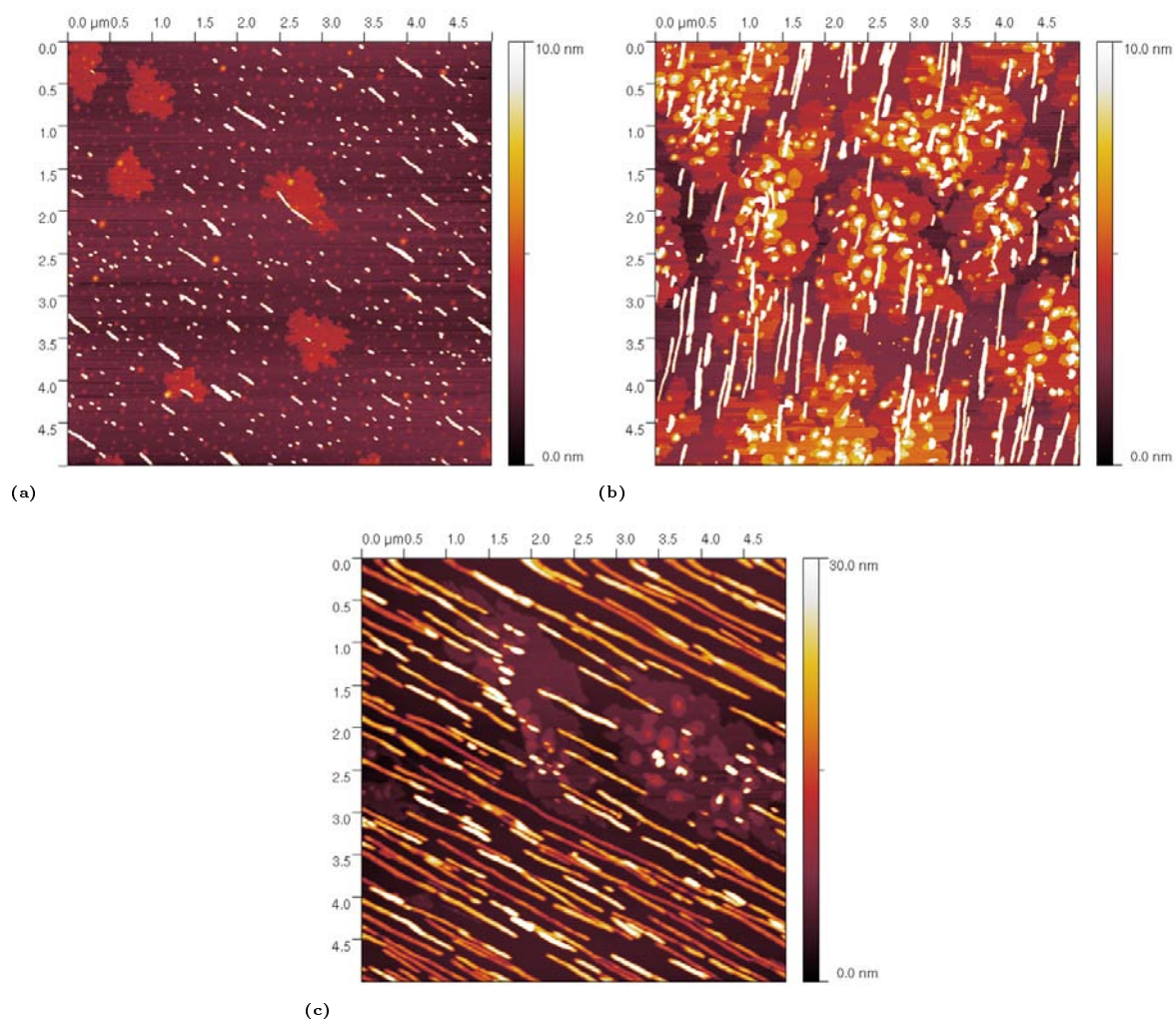
Figure 3.25: Morphology of 6P films grown on mica after extended exposure to ambient conditions. (a) 2 nm thick 6P film grown after 48 h of exposure. (b) 10 nm thick 6P film after 48 h of exposure. (c) 15 nm thick 6P film grown after 60 h of exposure to ambient conditions.
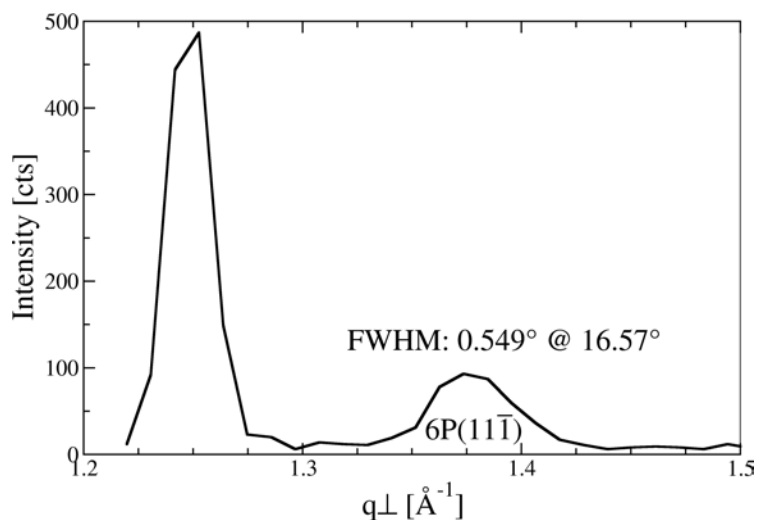
Figure 3.26: Specular scan of a 15 nm 6P film grown on contaminated mica. The large peak on the left comes from the mica(004) reflex. The peak labeled *6P(11$\bar{1}$)* shows that the chains are formed from lying down molecules. The data was obtained with synchrotron radiation.

By careful examination of the topography image one can see that the 6P island actually grows over the circular bumps. A cross section through the large terraces in fig. 3.29c (presented in figure 3.30) reveals that

1. The step height is 2.6 nm.

   - The island is therefore formed by upright standing molecules.

2. Only the islands give a phase contrast while the circular structures don't.

   - The islands are formed by 6P.
   - The circular structures have the same viscoelastic properties as the rest of the surface and are therefore mica.

Figure 3.29b presents the simultaneously recorded friction force image (FFM or LFM mode) to the topography image presented in fig. 3.29a. Just as in the phase image, contrast is only achieved between the 6P island and the rest of the surface. The circular bumps have the same friction properties as their surrounding. The circular bumps are the result of the high temperature preheating step. Natural muscovite like the one used in this investigation can contain up to 4.5% of water [122–124]. When the sample is heated to high temperatures the water segregates between the layers and by its hydrostatic pressure forms the typical bubble shape by pressing up the topmost layers. This process is temperature dependent as the sample heated up to 300 °C (fig. 3.29a) exhibits smaller circular features than the one heated up to 500 °C (fig. 3.29c).
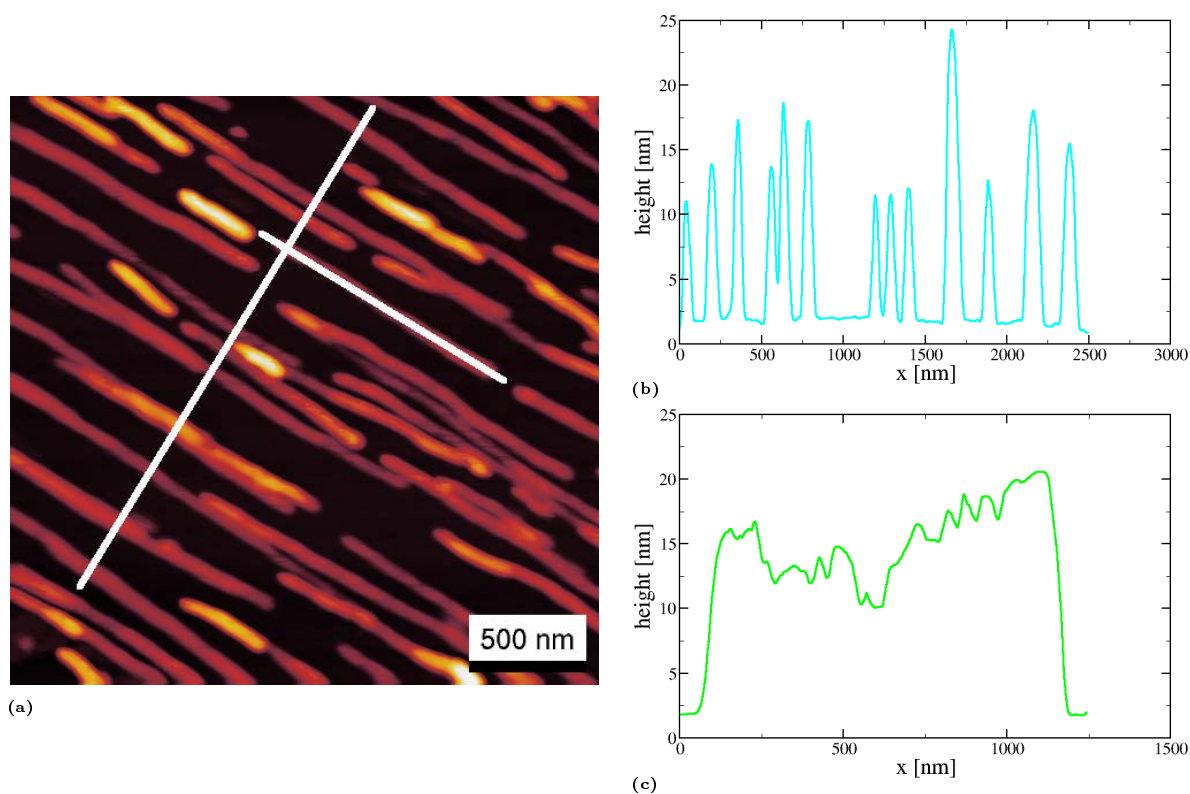
Figure 3.27: Cross sectional analysis of the chain morphology in 6P films grown on contaminated mica. (a) shows a larger scale image of the morphology and the position of the cross sections shown in (b) (perpendicular to the chains) and (c) (parallel to the chains).

From the phase image and the independent results obtained by FFM one can state that the 6P islands grow directly on the mica(001) surface without a wetting layer. However, AFM is a surface sensitive method and one can not completely exclude the existence of a wetting layer.

Therefore, TDS was used to proof this scenario. The group of A. Winkler carried out a number of TDS experiments on samples with different C-coverage. Figure 3.31a shows 4 different TDS spectra obtained from 6P films grown on mica samples with different carbon pre coverage. For morphological characterisation a 0.35 nm thick 6P is grown at room temperature. This film thickness is equivalent to one monolayer of flat lying molecules.

Curve (a) in fig. 3.31a is obtained from a freshly cleaved mica sample without additional carbon. However, there is about half of the saturation concentration of carbon present on the surface. Exposure to water and the carbonaceous atmosphere during the cleavage step are responsible for this carbon layer [118]. The spectrum has two peaks β and α for the wettinglayer and the beginning multilayer. This sample corresponds to samples prepared in a way used for the rest of the investigations. As shown in section 3.2.1 this wetting layer is present when the typical chain formation takes
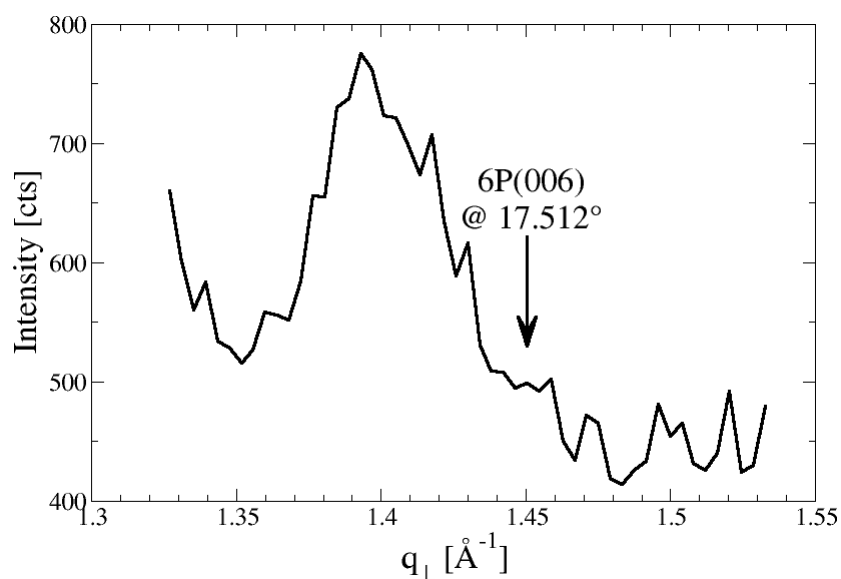
Figure 3.28: Specular scan of a 10 nm thick 6P film grown on contaminated mica. The shoulder at $\Theta = 17.512°$ corresponds to the 6P(006) peak. The large peak to the left is assigned to mica.

place. However, increasing the carbon concentration on the surface (curves (b)-(d)) suppresses the formation of the monolayer. In TDS, this shows up by the vanishing β peak. Finally, only the multilayer peak remains (d). This drastic change in desorption kinetics must be the result of a change in growth mode from SK to a different mode. Figure 3.31b shows the corresponding topography in a 3D representation. After deposition of a saturation layer of carbon, a 1 nm thick 6P film has been deposited at room temperature. The morphology is characterized by 2 ML high islands with an average diameter of 480 nm $\pm$ 80 nm for the first layer and 150 nm $\pm$ 60 nm for the second layer. The height of the first layer is 2.65 nm. From the cross section presented in figure 3.32a one can see that the second layer shows two different heights. The height distribution for an individual grain shown in fig. 3.32b reveals that indeed there are two different heights for the second layer of 2.2 nm and 2.6 nm. While the second value fits to the expected height for a layer formed by upright standing molecules, two possible configurations could explain the reduced height of the inner part of the top layer:

1. This part of the second layer is formed by degraded molecules consisting of only 5 rings. Assuming the same crystallographic structure this would result in a layer height of roughly 2.2 nm.

2. The molecules in the inner part of the top layer have a different tilt angle. The resulting tilt angle would be 33° instead of 17°.

From the existing data no conclusion can be given yet which scenario is the correct one, although the second one seems more likely.
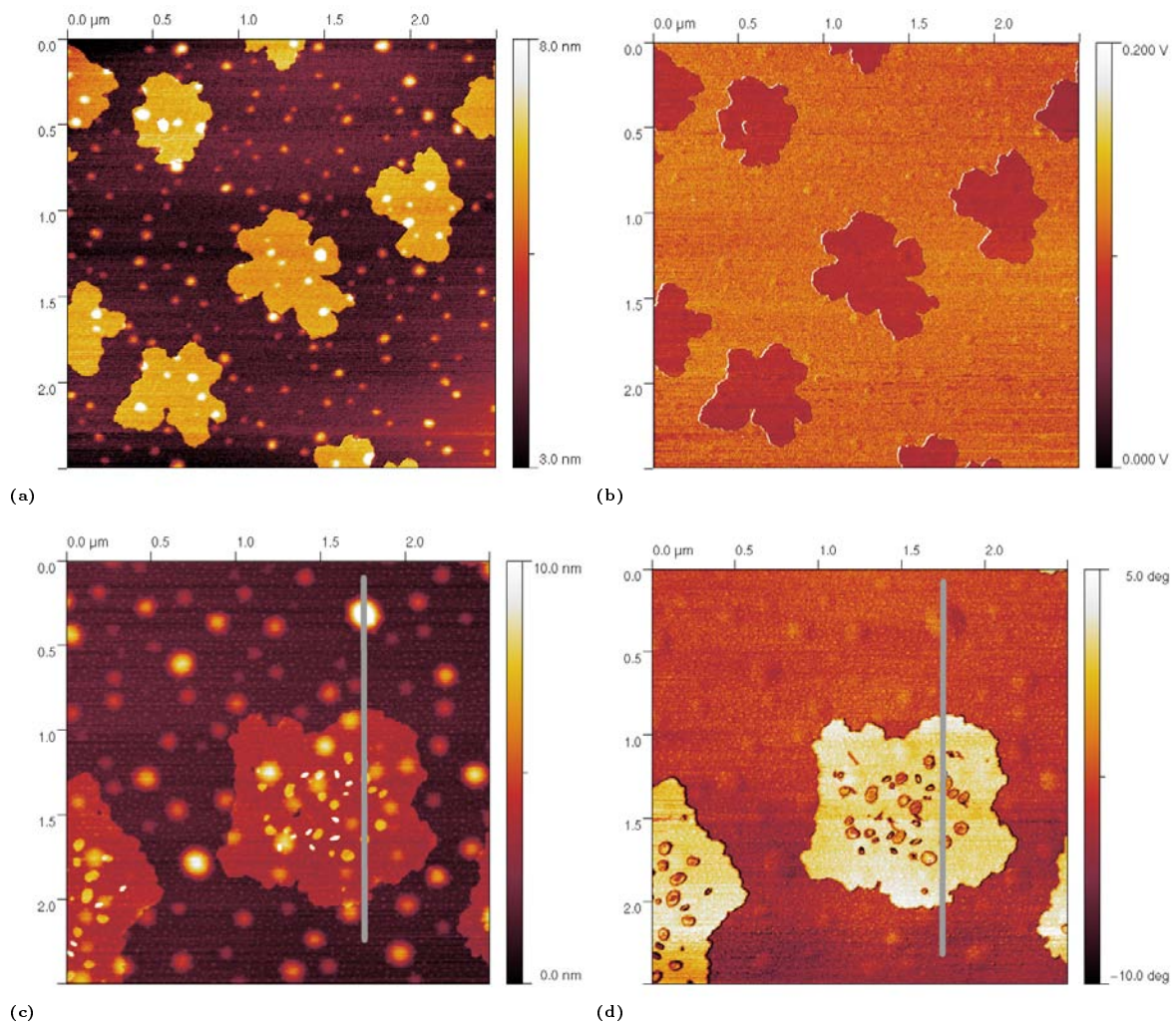
Figure 3.29: 1.3 nm thick 6P film formed by upright molecules on mica(001) grown at RT. (a) and (b) contact mode height image and friction image. This film was cleaned at 300 °C for 5 min. (c) and (d) tapping mode height and corresponding phase contrast image of he film cleaned at 500 min for 5 min.
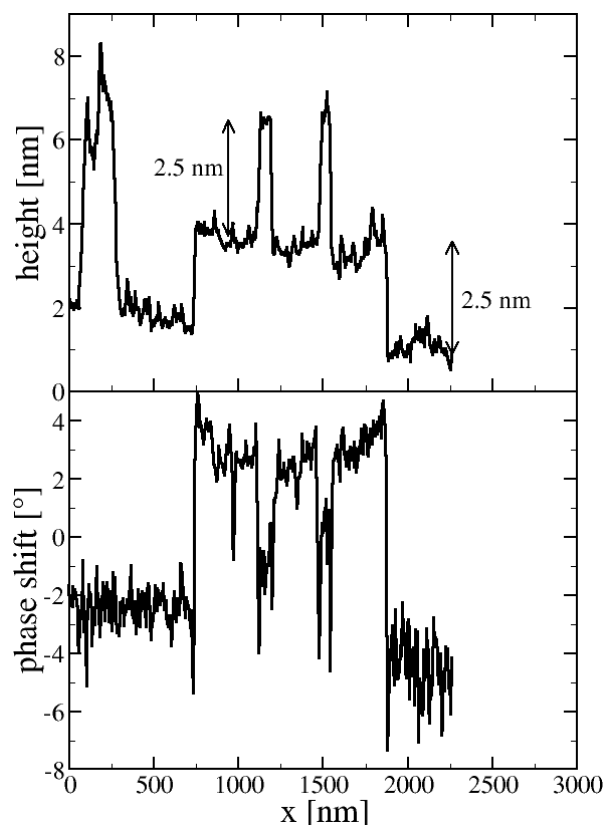
Figure 3.30: Cross sections through the large terrace in fig. 3.29c (top) and 3.29d (bottom). Phase contrast is only achieved from the terrace not from the circular structures.

Modification by pre ion bombardment of the mica substrate

Figure 3.33 shows the morphology of a 1 nm thick 6P film grown on ion bombarded mica at room temperature. The sample was bombarded with 500 eV Ar^+ ions for 300 s. About 1 µm large islands with an irregular shape are formed on the surface. The rms-roughness of the sample surface is 1 nm±0.1 nm. In contrast to the film grown on a carbon contaminated sample surface one can notice two main differences.

Also the nominal film thickness is the same as for the film presented in figure 3.31b there is nearly no second layer nucleation visible. All islands seem to be formed by one monolayer of upright standing 6P molecules. The coverage of the first layer is 50%. The second layer only covers 0.1% of the surface.

Figure 3.34 gives an overview about the morphology when the film thickness is increased. The samples were prepared under the same conditions as the one presented in figure 3.33.

Figure 3.34a shows a 4 nm thick 6P film. Up to 6 layers can be counted but in general there is one nearly closed layer (99.5% coverage) covered by a second layer (84.2% coverage) followed by isolated mounds of one or two layers in height (26.5%
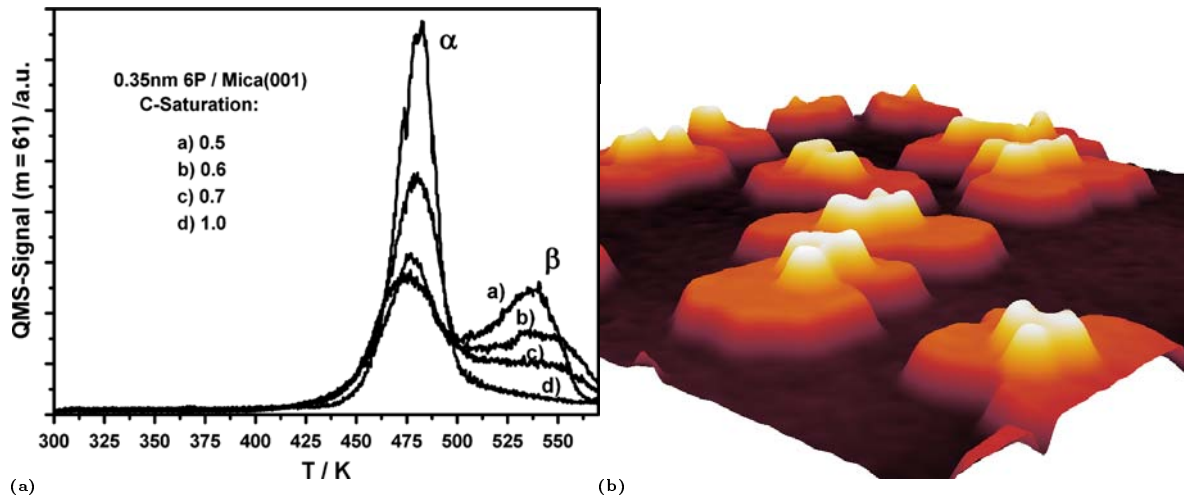
Figure 3.31: (a) TDS spectra from partially C-covered mica samples. The 0.35 nm thick 6P film was grown at room temperature. The wettinglayer peak (β) disappears with increasing carbon pre coverage and only the multilayer peak (α) is left. [69] (b) 3D representation of a 1 nm thick 6P film grown on mica after deposition of $\Theta = 1.0$ carbon (curve (d)). The image size is 2.5 µm by 2.5 µm and the z-scale 6 nm. Individual layers with a height of 2.6 nm are visible.
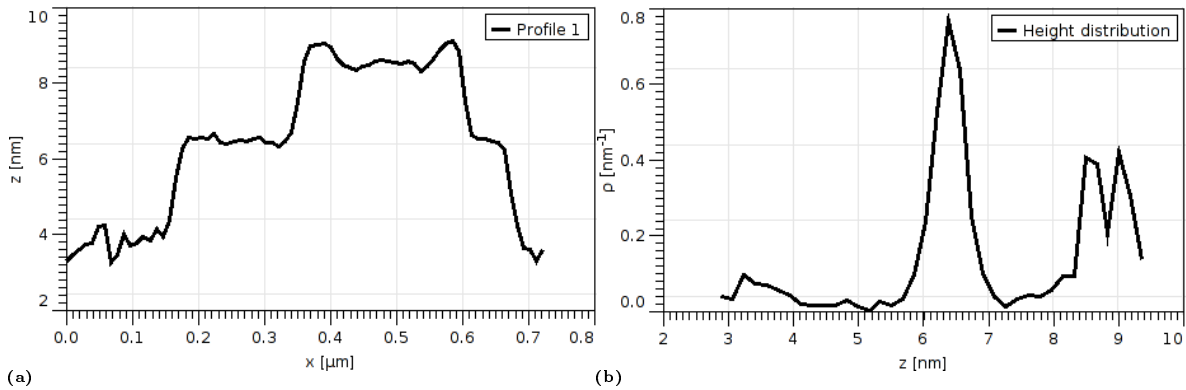
Figure 3.32: Height analysis of a single island from fig. 3.31b. (a) Cross section through an individual island. The height of the first layer and the two different heights of the second layer are visible. (b) Height distribution for the same island. Four peaks can be identified from left to right. First a small contribution from the substrate (3.4 nm, not representative due to the lack of sufficient statistics), the first layer (6.4 nm) and two peaks at 8.1 nm and 9.0 nm from the second layer.
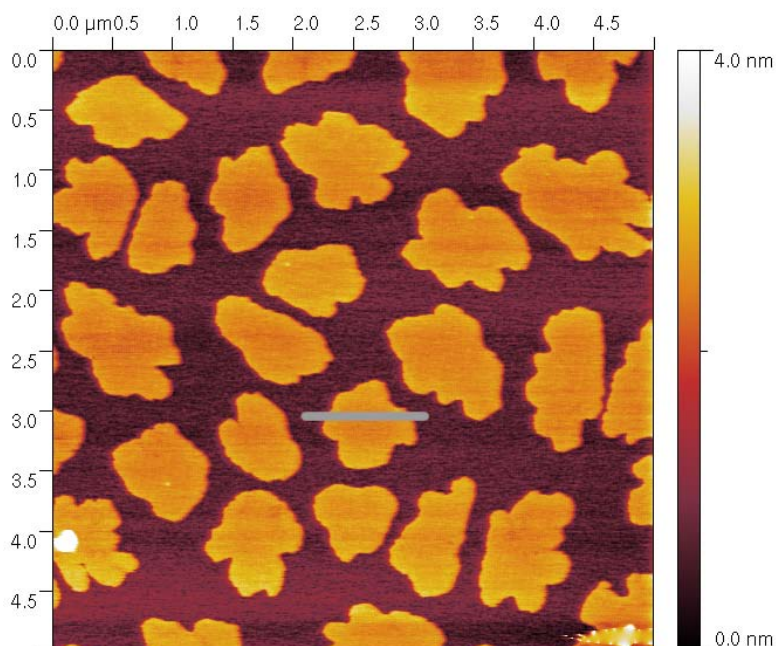
Figure 3.33: 5 μm by 5 μm AFM image of a 1 nm thick 6P film grown on sputtered mica.

and 9.3% coverage respectively). The first layer is not closed completely, but has some small holes in between the different mounds revealing the underlying substrate. (In figure 3.34a the substrate is colored in green.)

The described mounds are accompanied by small elongated crystallites that show no terrace structure. They have an average length of 200 nm±90 nm, a width of 120 nm±40nm and a height of 50 nm±20nm. These crystallites cover about 5% of the surface. From their shape we conclude that they are formed from lying molecules.

Figure 3.34b shows a 10 nm thick 6P film. Several layers (up to 7) can be counted and a clear tendency to a polygonal shape with a preferred angle of ∼120° between adjacent sides is observable. The orientation of the individual polygonal shaped mounds relative to each other seems random. In addition to the mounds formed by upright standing molecules, an increasing fraction (∼7.5%) of the surface is covered by small 6P needles. Although they occasionally connect two mounds usually every mound seems to have its own needles. Needles on different mounds lack a common orientation as no direction is given by the substrate. The needles have a length between 100 nm and 1 μm with an average value of 300 nm±230 nm. Their average width is 80 nm±40 nm and their height is 70 nm±30 nm.

Figure 3.34c shows the morphology of a 30 nm thick 6P film. The polygonal shape of the mounds becomes more pronounced but also the surface fraction covered by 6P
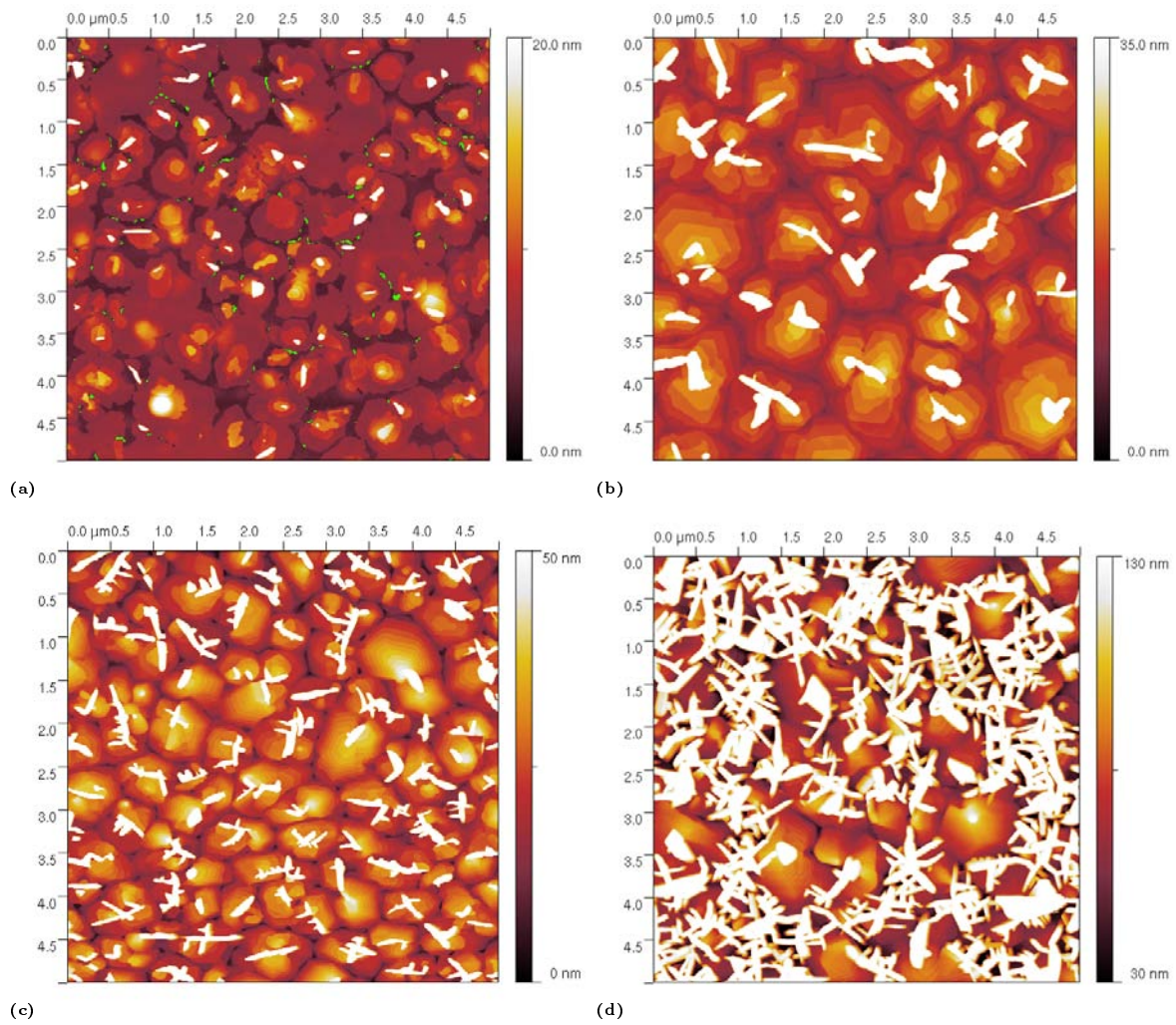
Figure 3.34: Series of AFM images showing the evolution of the film morphology with increasing film thickness. All films were grown at RT on ion bombarded mica(001). (a) 4 nm, (b) 10 nm, (c) 30 nm, and (d) 100 nm film thickness.

needles increases. Again neither of these two structures exhibits a preferred orientation. The needles have roughly the same length distribution as in the previous sample with an average of 330 nm±250 nm. The width changed slightly to 100 nm±50 nm and also the height increased to 110 nm±20 nm. However, their number increased significantly as they now cover 15% of the surface.

Figure 3.34d finally shows the thickest film in this growth series with a film thickness of 100 nm. About half of the surface is now covered by a network of 6P needles. Their width is about 100 nm±50 nm and the height obtained from cross sections is 130 nm±30nm. As the chains start to coalesce the length is hard to estimate but it is in the range between 100 nm and 1 µm. Although the needle fraction has increased dramatically the mounds continued to grow in height and a high number (more than 20) of terraces can be counted.

The needles are most likely formed from lying down molecules as they show the same morphology and features already known for needles or chains on other samples. This speculation is supported by the fact the needles only occur on the thicker films. On the first sample (see figure 3.33) no needles can be found. The formation of these needles requires an ordered substrate. However, the mica surface is disordered due to the preceding ion bombardment. When the film thickness increases and ordered mounds of upright standing 6P form they in turn act as the ordered substrate necessary for the formation of 6P needles. The needles are branched but show only a limited number of angles between the individual branches located on one mound. The most commonly observed angles are 18°, 90°, and 120°. Also combinations of the three are typical for 6P(see the structural and real space information in [53, 109, 125] and many others).

To investigate the morphology of the mounds the needles had to be removed from the images using the following method:

1. Mark all needles with a height thresholding algorithm.

2. Remove the selected parts of the surface with a Laplace filter using the unmasked area as a virtual source.

3. Calculate all further data for both the corrected and the uncorrected.

The last step allows to judge how strong the procedure disturbed the data.

Figure 3.35 shows the result of such a data manipulation. Although some fragments of the chains remain, the surface is now dominated by the mounds. One can also see that this process does not disturb the morphology of the mounds.

Figure 3.36 shows the characteristic shape of the mounds. The polygonal shape is clearly visible. The cross section shows a very unique shape. It is a sequence of steps, each the height of one monolayer, but the overall shape of the line is characterized by a large slope at the beginning that gradually decreases towards the top of the mound. This leads to the deep trenches between the different mounds, also visible in figure 3.36 and figures 3.34b to 3.34d. To obtain an average shape of the mounds the following procedure is used [28, 42, 126]:
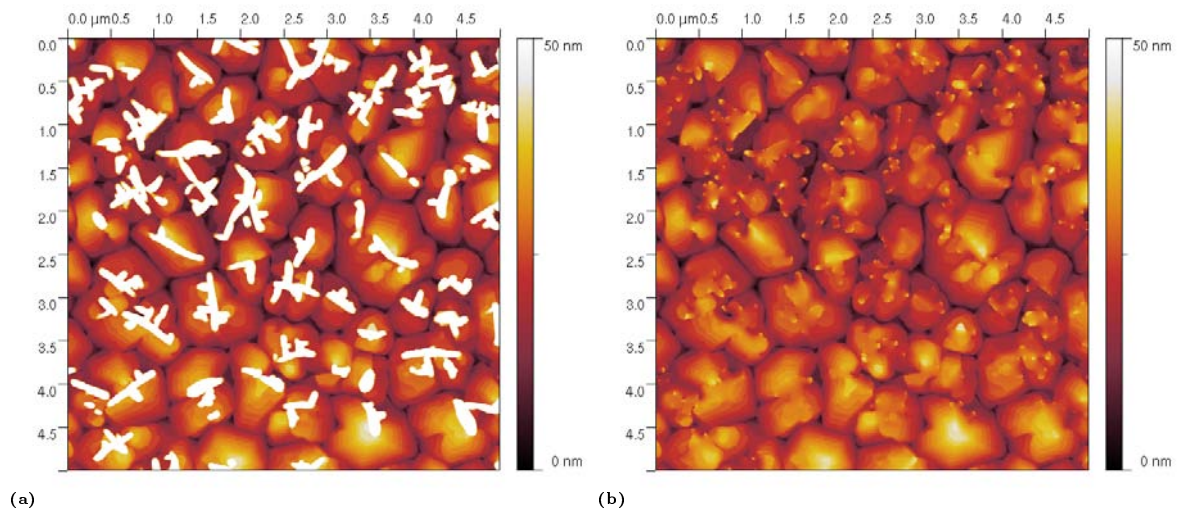
Figure 3.35: Illustration of the procedure to remove the needles. 5 μm by 5 μm AFM image of a 30 nm thick 6P film before (a) and after (b) removal of the needles using the procedure described on on the preceding page.
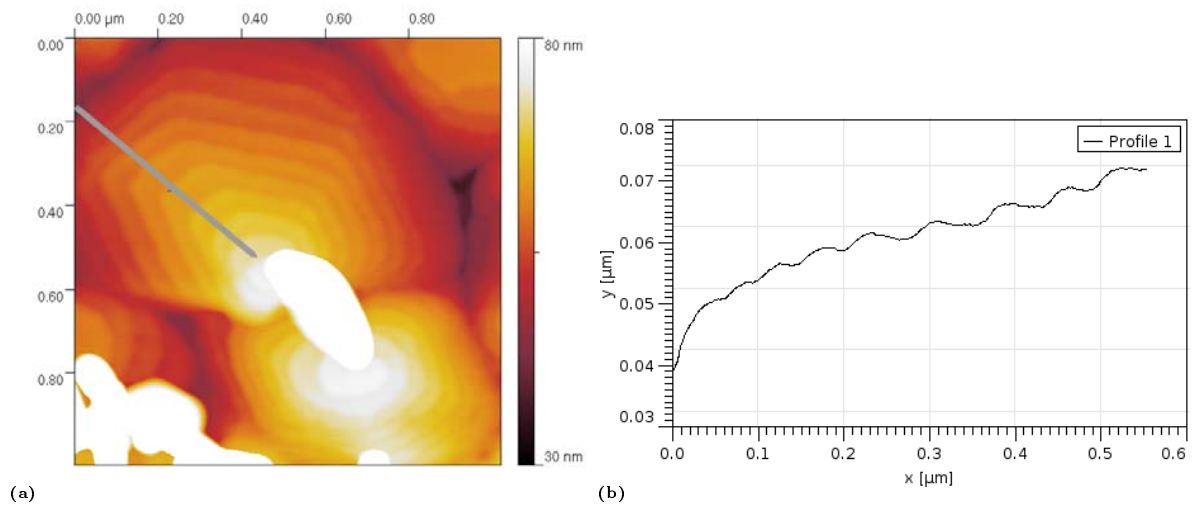
Figure 3.36: A typical mound in a 30 nm thick 6P film. A small needle is sitting on top of the mound. (b) shows the cross section marked in (a). One can see the characteristic lateral shape of the mound, characterized by a deep trench separating it from the neighboring mounds.

1. If necessary the needles are removed following the procedure introduced above.

2. The total area of each terrace is calculated. This includes the visible part but also the part covered by the next layer.

3. The square root of the area is defined as the equivalent radius of the layer.

4. The radius of several grains is normalized.

5. The arbitrary layer number is plotted versus the normalized grain radii.

Figure 3.37 shows the result obtained from 5 different grains in a 30 nm thick 6P film. The shape is characterized by the following features.

1. 2.6 nm±0.3 nm step height between the individual layers

2. A non-uniform slope

3. Deep trenches at the bottom

4. A flat top

Figure 3.38 shows the result of the same analysis for the 10 nm and 100 nm thick films. The shape found in these films is similar to the one described above. From the shape one can draw the following conclusions

1. The uncovered areas of the terraces become smaller towards the bottom.
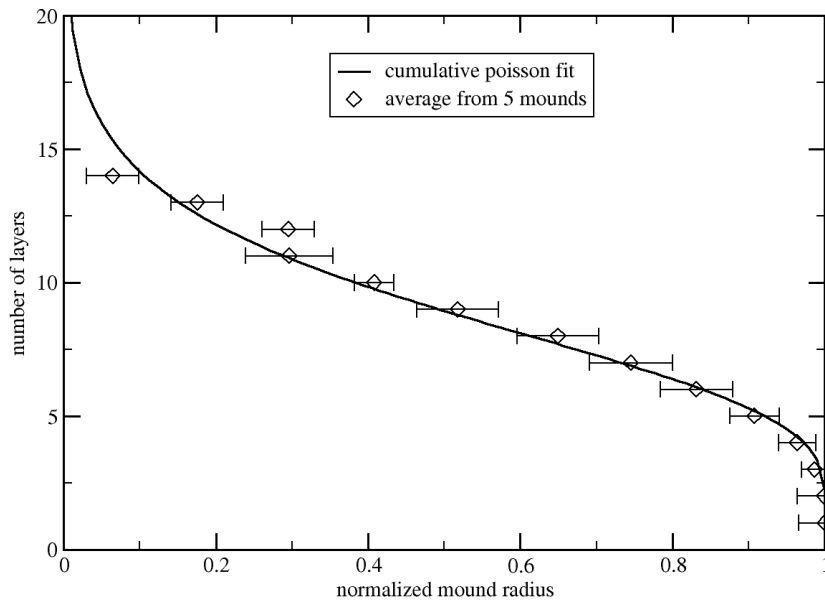
Figure 3.37: Shape analysis for mounds in a 30 nm thick 6P film.
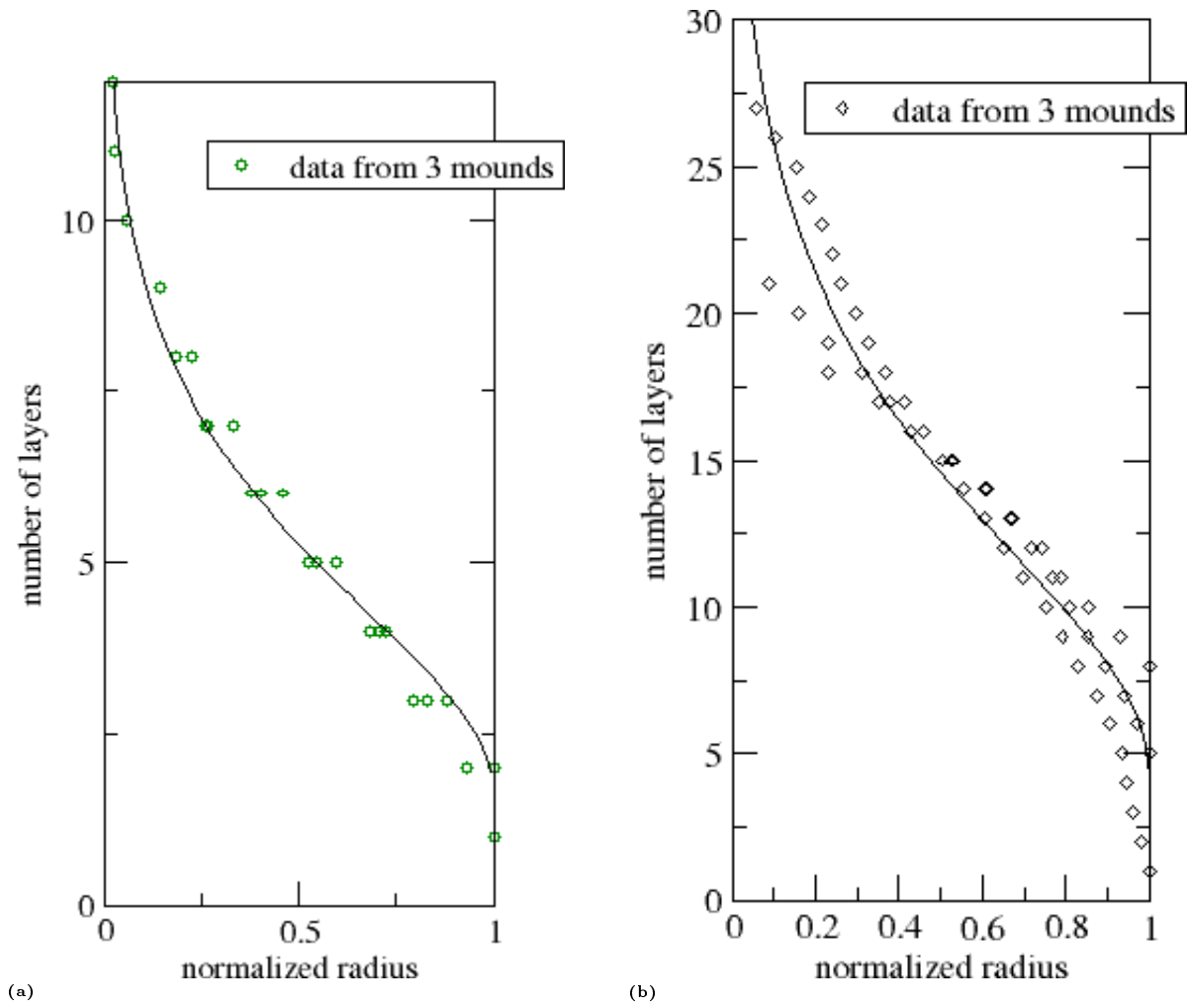
Figure 3.38: Mound shape analysis for a 10 nm (a) and a 100 nm (b) thick 6P film.

2. The probability for a molecule to land on a lower terrace is smaller compared to landing on a higher terrace.

This points towards the Zeno-effect described in section 1.2.2. Indeed the data points can be fitted (solid line in fig. 3.37 and 3.38) by a cumulative Poisson Distribution.

We can calculate the relevant roughness parameters for the films from the HHCF and by fitting with equation 2.10. This allows to check the predictions made by the Zeno model for the following roughness parameters: σ root mean square roughness, ζ system correlation length, α Hurst parameter, and λ Mound separation.

We will first discuss the two most important parameters σ and λ because they will allow us to judge if we indeed have have a morphology that can be explained by the Zeno Model.

Figure 3.39a shows the evolution of the rms-roughness with ongoing deposition. Here, σ is plotted versus the film thickness in ML. If we fit the data (ignoring the data for the film with a thickness below 1 ML) we obtain a value for the growth exponent β of 0.48 which is in perfect agreement with the predictions of the Zeno Model. As shown earlier, the Zeno Model predicts an evolution of σ following a power law with an exponent of 1/2. In the graph, the fit (solid line) and the prediction of the Zeno Model (dashed line) are drawn. The first data point is not included in this and the following fits as no mounds have formed so far. A further reason is given on 85pp.

Figure 3.39b shows the evolution of the mound separation λ with ongoing deposition. Again we can use a power law to fit this data and obtain an dynamic growth exponent $1/z$ of -0.01. Within the error of the estimation this means that the mound separation does not change and $1/z = 0$. This is one of the predictions made by the Zeno model.

(a) (b)
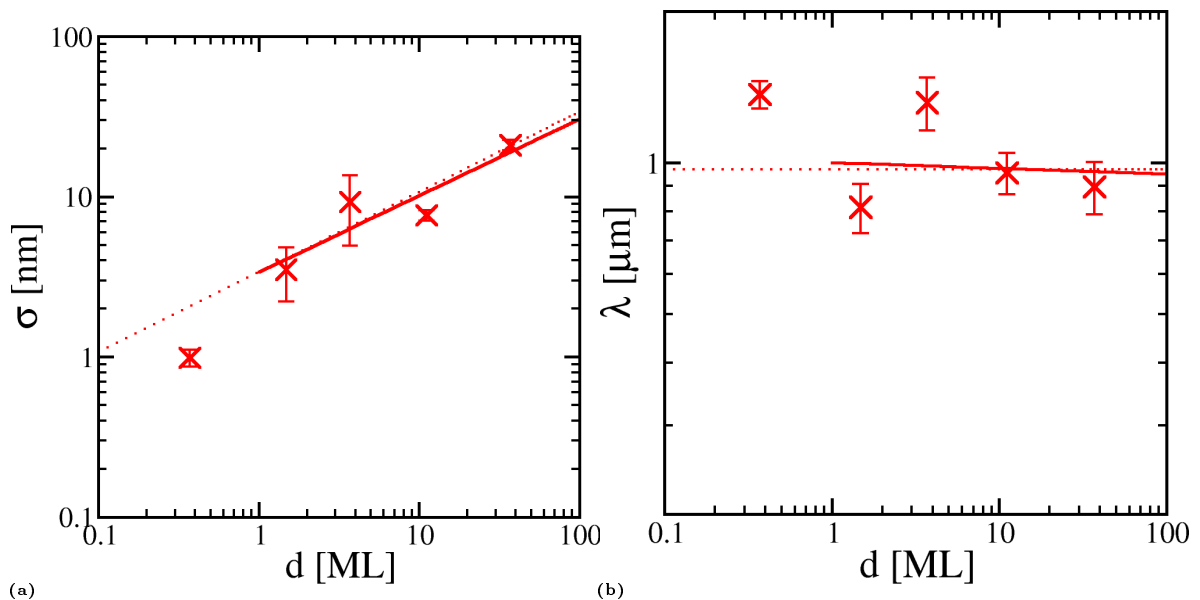
Figure 3.39: Vertical (a) and lateral (b) roughness evolution of 6P on sputtered mica.

A consequence of the Zeno Model is that there is practically no mass transport between individual mounds. Therefore the distance between the mounds is fixed after the initial nucleation on the substrate.

The two remaining parameters α and ζ are plotted in figure 3.40. Figure 3.40a shows that the Hurst parameter α has values very close to 0.5 for all film thicknesses. This is a consequence of the cumulative Poisson distribution like lateral shape of the mounds. The theoretical form of the mounds is characterized by very pronounced peaks at the top and deep trenches at the bottom. Such a surface profile leads to an exponential surface height distribution where the majority of all height values in concentrated in a center region of the surface height distribution. Such a surface is described by a Hurst paramter of 1/2. However, in a real film the top is truncated, but the deep trenches will still lead to an exponential height distribution. The system correlation length ζ is a measure for the randomness of the mound separation λ. With ongoing deposition, the footprint of the mounds does not change as mass transport between the mounds seems to be suppressed. However, when more layers are grown the mound shape gets more regular and the mound tip seems to center above the mound base. This leads to an slight increase in the order parameter ζ shown in figure 3.40b.

As a consequence of the constant mound separation is that the bottom point of the mounds do not move with ongoing deposition. The top edge of the mound moves only vertically but not horizontally, because the top terrace diameter is constant for a given value of the step edge barrier. This leads to the fact that with ongoing deposition the mound slope is increasing continuously. The local mound slope is given by

(a) (b)
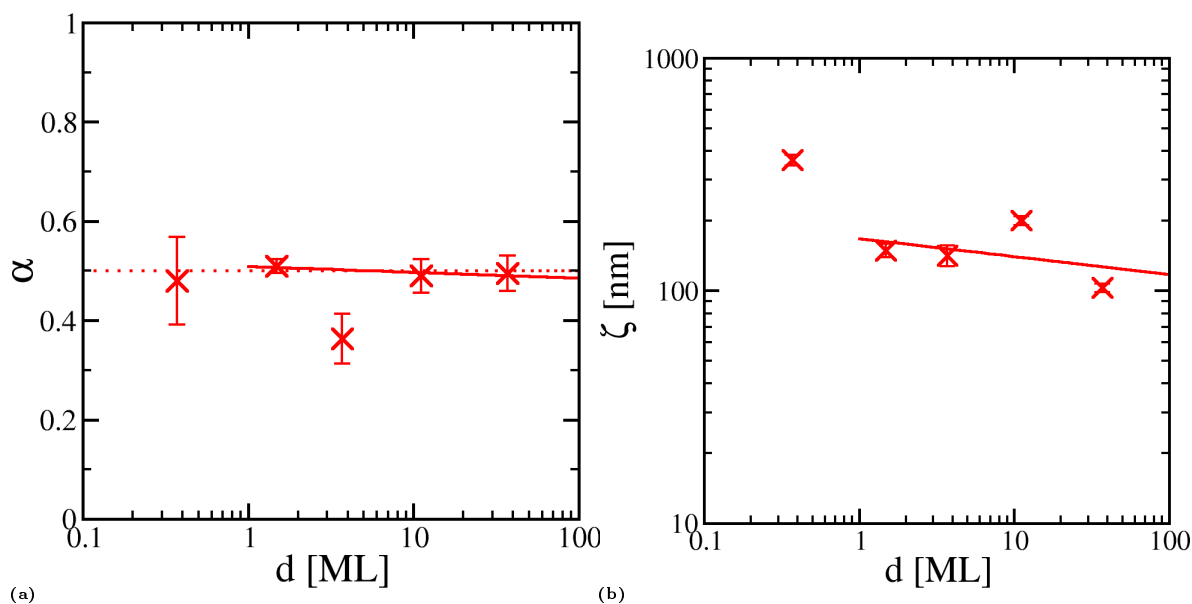
Figure 3.40: Evolution of additional surface parameters. (a) evolution of the Hurst parameter α which is a measure for the jaggedness of the surface. (b) evolution of the system correlation length ζ, a measure for the randomness of the lateral mound separation λ (fig. 3.39b)

$$m^2 = 2\sigma^2 \left(\frac{1}{\zeta^2} + \frac{2\pi^2}{\lambda^2} \right) \tag{3.2}$$

which reduces to

$$m = \frac{\sigma}{\zeta} \tag{3.3}$$

for $\zeta/\lambda \ll 1$ [93, 95]. The result is plotted in figure 3.41.

Figure 3.41 shows the result of equation 3.3. A power law fit ($m = d^n$) to the obtained data points reveals that the slope is increasing with an exponent $n = 0.55$.

The statistical analysis carried out above clearly shows that the growth is following the predictions made by the Zeno Model, we can therefore use the equations (1.20), (1.5), (1.17), and (1.18) given in section 1.2.2 to calculate the Ehrlich-Schwöbel Barrier necessary to obtain the observed mound shape.

The top terrace size used in (1.20) can be obtained by measuring the top terrace diameter ℓ from cross sections which is between 20 nm and 60 nm. $\lambda = 1\ \mu$m is an estimate for the diffusion length used in (1.5). On could argue that the obtained λ value is not obtained from a homoepitaxy experiment but from a heteroepitaxy experiment. In deed the nucleation happens on the ion bombarded mica surface and not on a 6P film. The rest of the growth is then similar to homoepitaxy as 6P grows on already existing terraces of 6P. However, our estimate for λ will result in a minimum diffusion coefficient. If the diffusion coefficient for 6P on 6P would be significantly smaller than the one observed two nuclei would form on top of the first single layer islands. This is not the case as can be seen from two observations:
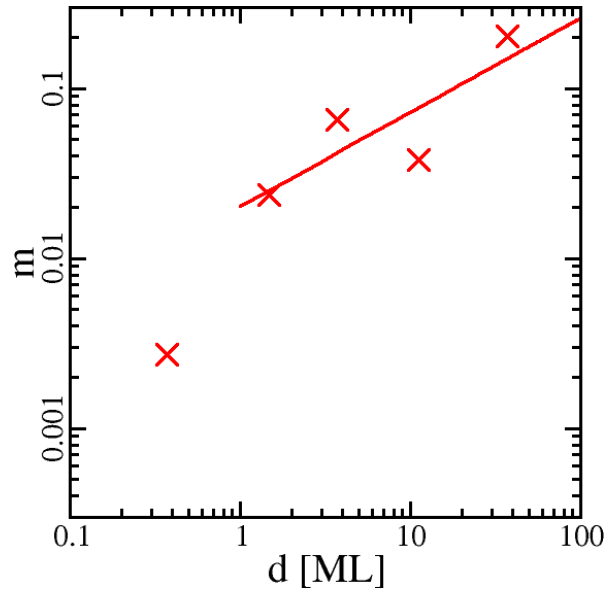
Figure 3.41: Local slope m plotted versus the film thickness in ML.

1. λ is constant throughout the whole experiment so no new mounds are nucleated after the initial nucleation on the mica surface.

2. A significant deviation towards higher coverages for the second and higher layers is not observed for the first 1 nm thick film.

Using the values the ESB for para-Sexiphenyl can then be estimated to be 0.67 eV. The error of $\approx$0.1 eV in this estimation comes mainly from the uncertainty in ℓ which is hard to measure.

This is a very high value for the additional energy barrier an molecules encounters when trying to jump over the terrace edge. However, several arguments can be made to support this finding.

Incorporation from above like downward funneling [127] or a *push out* mechanism where an edge particle is pushed out so that a second on top of the terrace can take its position [23, 128, 129], plays no role in the formation of these mounds. As has been shown by Schinzer et al., these processes that would effectively circumvent the stage of hopping across the edge, would lead to a growth exponent $\beta \approx 0.3$, which is not observed here. Furthermore, it would lead to slope selection instead of the observed continuously increasing local slope m [130].

A low number of kink sites at least for the thicker films can be assumed. At a kink site, the barrier might be expected to be lower than on a flat step. However, if one looks at the sequence of images with increasing film thickness (fig. 3.34) one can see that the terrace edges are getting very smooth already at very low coverage (4 ML see figure 3.34b) which results in high values for the ESB. Two effects lead to the straightening of the step edges.

1. With ongoing deposition the lower lying terraces become smaller.

2. This in turn will reduce the number of molecules landing on a terrace.

3. This will give edge molecules more time to diffuse around the step edge to find an existing kink position instead of forming a new kink dimer.

The smoothing effect on the step edges gets stronger with increasing film thickness and should lead to an increase of step edge barrier with ongoing growth. During the deposition of the first few monolayers a higher kink density will exist and reduce the height of the barrier. This effect has been described already by Kalff and coworkers for Pt homoepitaxy.

However, Pt atoms are zero dimensional particles. For quasi one dimensional molecules the situation is more complicated.

The anisotropy of the building blocks and the possible consequences will be discussed in the following. It will lead to a much more complicated situation than in the classical inorganic picture of the ESB, where just single atoms are the diffusing species.

Different situations can be imagined when a molecule tries to diffuse across the step.

1. The diffusion direction and the long molecular axis are the same.

   - As the molecule will most likely diffuse in a direction parallel to its long molecular axis, it is approaching the step in the correct orientation.
   - When the molecule manages to diffuse over the edge it will be in the correct orientation for incorporation into the layer.
   - In an intermediate stage the molecule is either sticking out over the terrace (assuming it is rigid) or heavily bent.

2. The diffusion direction and the long molecular axis are perpendicular to each other.

   - Assuming that diffusion on the terrace is primarily along the long molecular axis, the molecule has to turn to reach a position where it can move over the edge.
   - After the molecule has overcome the barrier it has to rotate a second time to be incorporated into the terrace.
   - A flexible molecule can *sneak* over the edge without to much bending.

However, in both situations for a rigid molecule approximately half of the bonds between the diffusing molecule and the terrace have to be broken at some point. From experiments it is known that the molecules are very flexible [131], and can therefore partly saturate the broken bonds by bending over the edge and exposing their unsaturated π-electrons to the π-systems of the molecules at the terrace edge.

Preliminary MD calculations performed by P. Puschnig from the Chair for Atomistic Modelling and Design of Materials, University of Leoben, using Brenner's REBO potential [132] for the short-range interactions while the long-range nonbonding van der Waals interactions are characterized by the Lennard-Jones (12,6) potential [133], support these ideas. The binding energy for a single lying 6P molecule on the (001) 6P surface is about 1.27 eV. This is in good agreement with the above statement that half of the bonds have to be broken to diffuse across the terrace edge, and the ESB should therefore be about half of the binding energy. The calculations also revealed a minimum diffusion barrier of 0.11 eV for a molecule diffusing in the direction of its long axis in on a (001) terrace of 6P. It seems most likely that most of the molecules will therefore, arrive in the first of the two above described configurations at the step edge. If a molecule is placed perpendicular to the step edge with approximately half of it sticking out, it will diffuse downwards. When in the starting positions more phenyl rings are still on the top terrace it will lead to a movement back onto the terrace. The energy necessary to put a single 6P molecule in this position is roughly 0.76 eV.

Taking into account the diffusion barrier this results in an ESB of 0.65 eV. However, performing the same optimization for a molecule placed parallel to the step edge results in a lower step edge of only 0.55 eV. Figure 3.42 shows three snapshots taken from the corresponding 10 ps long MD simulation. The problem with this particular pathway across the step edge is that the molecules seem to diffuse mainly in a direction parallel to their long axis. To get into the assumed starting position the molecule has to rotate. Although the barrier is smaller, this process might not be observed because it is unlikely that a molecule can reach the starting position. Currently MD simulations are performed by P. Pusching to investigate this necessary step.

The situation gets more complicated when one also looks at the tilt angle of the molecules in the underlying terrace. As one can see in figure 3.43 it makes a huge difference for the molecule which side of the terrace it encounters when trying to overcome the edge. In figure 3.43 the diffusing molecules are drawn perpendicular to the step edge for better visibility. From the results presented above it is more likely that the molecule is diffusing over the step edge parallel it. When the molecule starts to stick out over the edge (fig. 3.43b) there will be a different energetic situation between the left and the right molecule (fig. 3.43g) this will change the way the molecule moves over the terrace edge (fig. 3.43c-3.43e). It has to be stressed that the energy landscape shown in 3.43g is only a sketch and does not not show the real dimensions neither in length nor in energy. The energy gain for incorporating a molecule into the existing terrace will most likely be equal or similar for left and right edges. However, finally both of the molecules will be incorporated into the top terrace (fig 3.43f).

In a real crystal the situation has to be refined. The 6P mounds have a polygonal shape with 6 sides in average, as a result there will be a number of different steps on a mound. These steps will not only differ in tilt angle but also in the way they are terminated by the herringbone structure of the molecules. The ESB for most of the

(a)   (b)   (c)
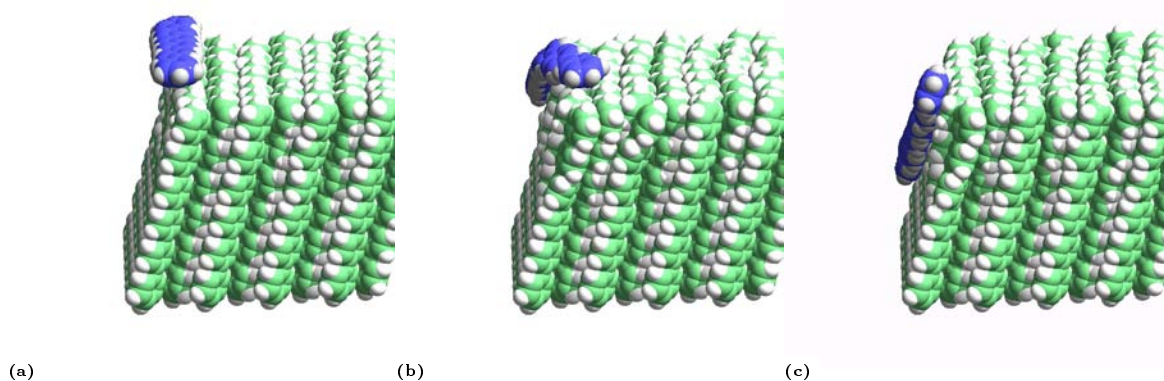
Figure 3.42: 6P molecules diffusing over the step with a starting position parallel to the step edge. (a) molecule in its starting position for the simulation parallel to the step edge. (b) *sneaking* over the edge, and (c) the molecule has overcome the edge and is finding its final position. (Courtesy of P. Pusching)
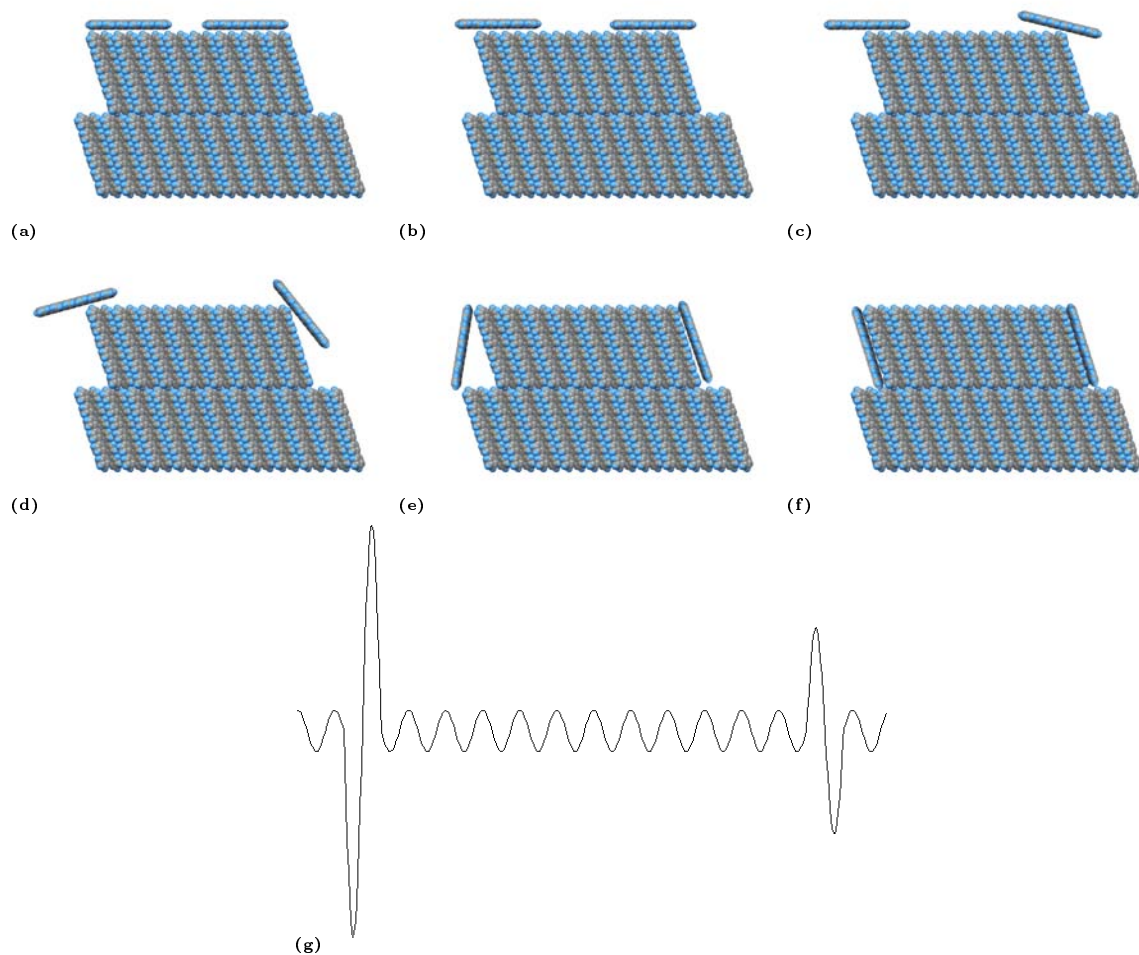
Figure 3.43: (a)-(f) sequence of sketches showing two individual 6P molecules moving over forward and backward tilted edges onto a lower terrace. (g) Principle energy landscape for molecules diffusing from the shown top terrace to the lower one. Due to the different orientation of the slab molecules with respect to the edge different energy barriers are encountered by the molecules.

steps will be between the two drawn extremes from figure 3.43.

The initial step in mound formation needs further attention. A cross section through one of the islands in the 1 nm thick film (shown in figure 3.44a) reveals a different height (2.0 nm±0.15 nm) as expected one for a tilt of 17°(2.7 nm). Figure 3.44b shows the height histogram which yields the same average film thickness of 1.98 nm±0.27 nm for the islands. As a collective degradation of 6P to 4P (with a length of approximately 18 nm) is a very unlikely scenario, a different tilt angle for the molecules is a much more realistic reason for the difference. A tilt of the long molecular axis with respect to the surface normal of 46° would explain the reduced island height.

A similar situation is found for the 4 nm thick film. In figure 3.45 the height distribution for image 3.34a is shown. Fitting the individual peaks with Gauss shapes shows that the layer separation increases with increasing mound height. While the first monolayer has a height of 2.33 nm this value increases and reaches the value expected for 17° tilted molecules of 2.7 nm in the bulk 6P configuration. Table 3.3 summarizes the measured height and the resulting tilt angle of the molecules. The difference between the two values given for the first monolayer is most likely related to the fact that they are obtained from two different samples with different coverages. This in addition to the uncertainty of the growth process can explain the difference.

Figure 3.46 displays the situation. The orientation of the molecules in the first layers are influenced by the substrate while layers further away from the mica surface feel less influence. As a result the molecules close to the interface have to find a position between satisfying the constrains given by the molecule substrate interaction and the molecule molecule interaction also present in the bulk phase. However, molecules in a layer separated further from the substrate can find their optimum position similar to the bulk phase. A similar phenomenon has been observed for the growth of copper-phthalocyanine (Cu-Pc) on highly oriented pyrolytic graphite (HOPG). There the tilt angle of the molecules gradually decreases from 90°(flat lying) in the first monolayer

(a)   (b)
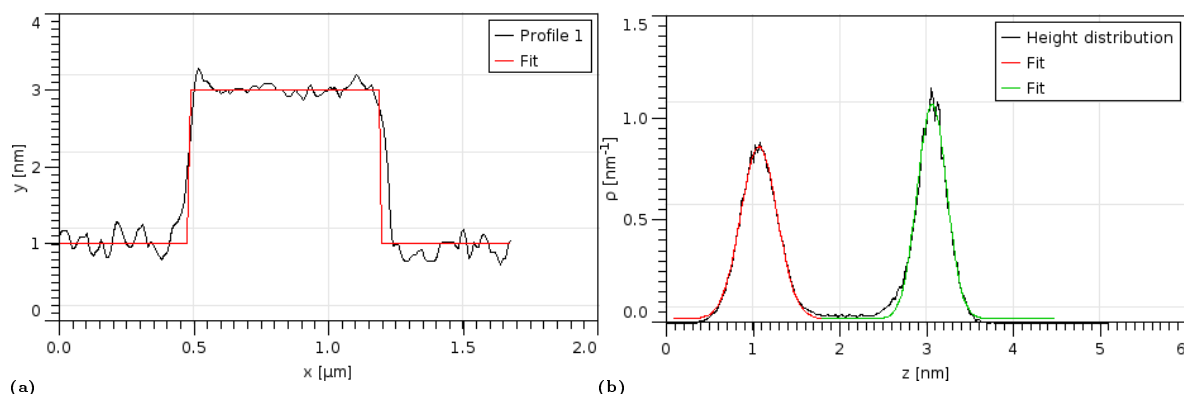
Figure 3.44: Section (a) and height histogram (b) of a 1 nm thick 6P film (see fig. 3.33). The histogram includes the whole picture (32 islands).
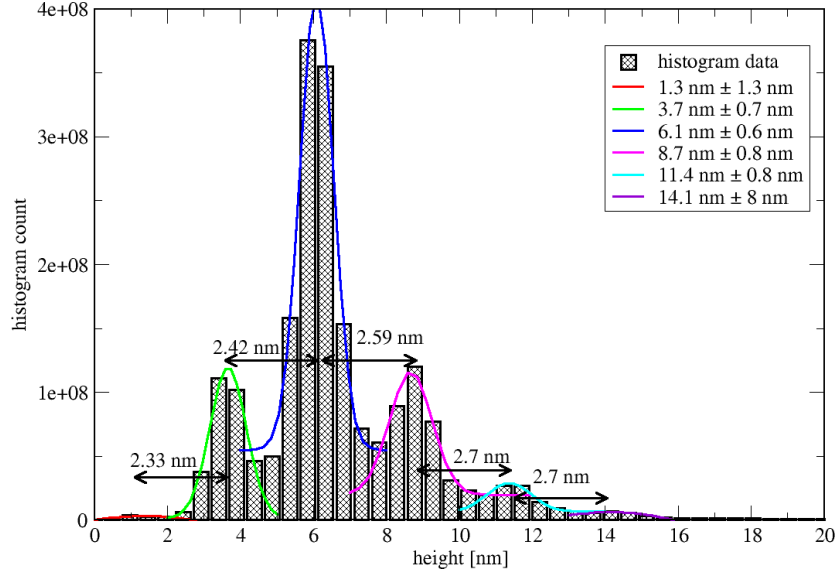
Figure 3.45: Height distribution obtained from a 4 nm thick 6P film on modified mica(001) (see figure 3.34a. The first peak at 1.3 nm originates from the substrate. The following peaks are from the individual 6P layers.

Layer	thickness [nm]	angle	comment
1	2.00±0.1	43°	isolated monolayer islands (fig. 3.33)
1	2.33±0.9	32°	measured at the small holes in the first monolayer
2	2.39±0.4	30°	averaged from three different images
3	2.55±0.5	22°	averaged from three different images
4	2.69±0.6	19°	averaged from three different images
-	2.73	17°	bulk value

Table 3.3: Increase of layer thickness for the first 4 layers as found in the 4 nm thick film and calculated thickness of a layer having the bulk structure. The first value is obtained from a 1 nm thick film where only isolated islands are found.

to smaller values for thicker films [134]. An analogous observation is also reported for Cu-Pc on MoS_2, where the molecules lie flat in the monolayer but are tilted in thicker films by 10°with respect to the substrate surface [135]. A closely related behavior is known from pentacene thin film growth. However, there it is an abrupt transition from an orthorhombic polymorph (the so called thin film phase [136]) to a triclinic one [137]. The transition observed here is a smooth reorientation from a tilt angle of over 40° to 17° for the bulk phase.

A different consequence of the increased tilt angle can be seen by carefully analysing the 1 nm thick film shown in figure 3.33. Assuming the absence of interlayer mass transport due to the existence of the high ESB as has been determined above, a nominal 1 nm thick film would lead to a coverage of 37% for the first monolayer. A part of the molecules should form a second and maybe third layer because of the calculated ESB of 0.67 eV. Surprisingly no third layer was found in this sample and the second layer covers only 0.11% percent of the sample surface. We can use (1.12) to calculate the expected coverage for a 1 nm and 4 nm thick film. h has to be expressed in terms of monolayers and is 0.37 ML and 1.48 ML respectively. The expected coverage in the different layers and the measured values are summarized in table 3.4. It is clear that the lower coverage in the higher layers must be the result of significant interlayer diffusion due to a lower step edge barrier. In addition to the effect of an increased kink density for the first layers, this fact can be explained by the increased tilt angle of the molecules in the first layers.

Due to the higher tilt angle in the first layers, molecules diffusing on them will feel a stronger influence from the $\pi - \pi$ interaction with the molecules terminating the edge. This will lead to a decrease of the ESB and result in the observed more layer by layer growth for the thin films. Figure 3.47 illustrates the situation. Due to the increased tilt of the molecules forming the first layer, a larger force (orange arrows) is acting on the molecule trying to diffuse down compared to a molecule trying to do the same thing in the top most layer with the bulk structure.

We can use (1.6) and (1.7) to get an estimate for the reduced barrier in the first
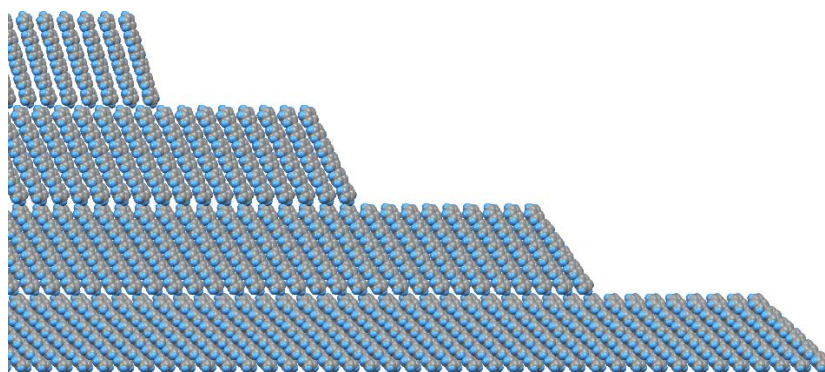
Figure 3.46: Sketch illustrating the gradual increase of the molecular tilt angle in the first few layers.

layer	1 nm thick film		4 nm thick film	
	expected value	measured value	expected value	measured value
1	30.9%	50.0%±2%	75.5%	94.5% ±4%
2	5.3%	0.1%±0.01%	41.8%	84.2%±3%
3	0.6%	0%	16.9%	26.5%±1%
4	0.005%	0%	4.6%	9.3%±0.5%

Table 3.4: Expected and measured coverage for the 1 nm and 4 nm thick 6P film.
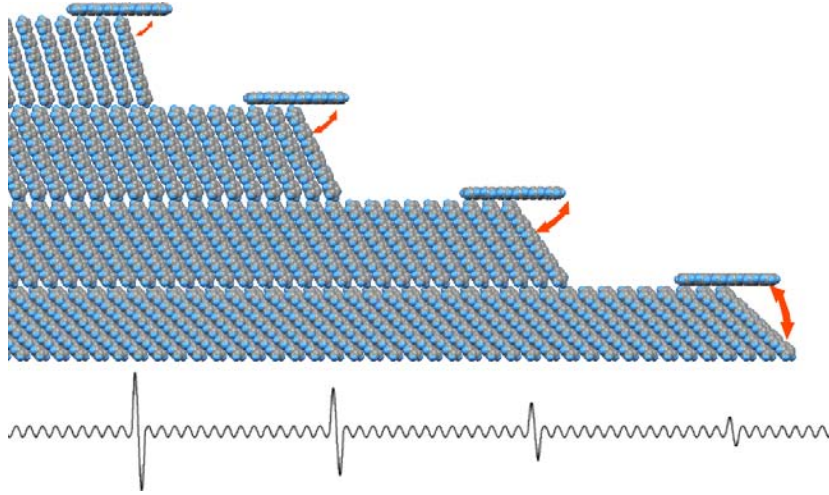
Figure 3.47: 6P island with different tilt angles for the individual layers and molecules trying to diffuse to a lower layer. The energy landscape at the bottom is indicating the level depended ESB. The size of the orange arrows indicates the size of the additional force acting on the molecule due to the $\pi - \pi$ interaction.

monolayer. About 2% of the islands have nucleated a second layer island. The size of the islands measured in terms of their perimeter is 2.566 µm±60 nm or 4276 given in units of edge sites. The area of the islands necessary to determine $\alpha = 0.055$ is 0.36 µm². Using these values, an ESB of 0.26 eV can be estimated for the first monolayer. This is significantly lower than the final value of 0.67 eV and well outside the error of 0.1 eV for the above estimation.

The trend of a lower ESB with increasing tilt angle of the molecules is also verified by MD simulations performed by P. Puschnig. Figure 3.48 shows the calculated ESB for 6P layers with different tilt angles. Although the value are different the trend is reproduced by the simulations.

In section 1.2.2 we assumed that the size of the stable nucleus is in fact 2 ($i^* = 1$). From the presented data no assumptions can be made on the real size of the nucleus. However, for $i^* > 1$ nucleation on the top terrace would be more difficult and the terrace would get bigger before the next layer is nucleated. Therefore, to get the same resulting shape an even higher ESB would be required. Our result can therefore be
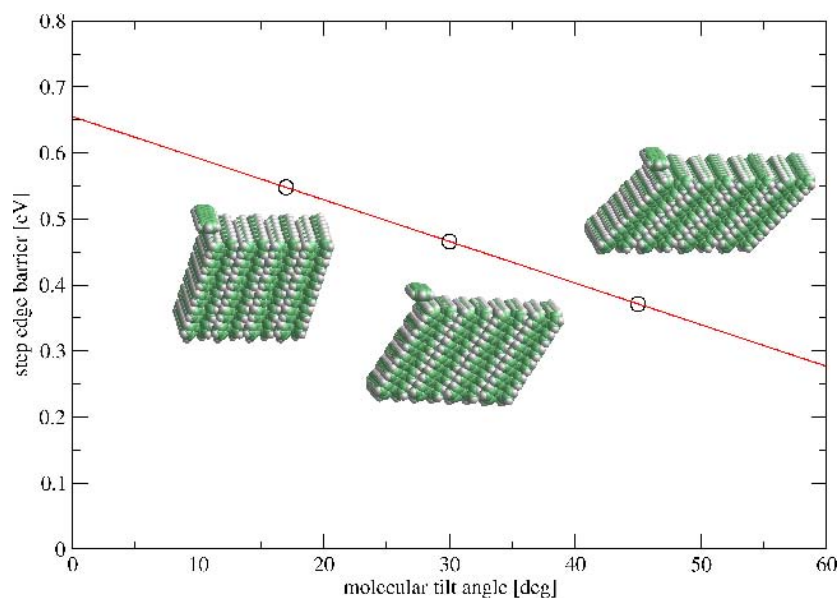
Figure 3.48: MD simulation results for level depended ESB. With increasing tilt angle the step edge barrier decreases. (Courtesy of P. Puschnig)

interpreted as the minimum ESB necessary to obtain the described cross sectional shape of the mounds. New results obtained by M. Campione [138] for sexithiophene (6T) on 6T(100) homoepitaxy reveal a critical nucleus size of 1 ($i^* = 1$) at room temperature. Only for elevated temperatures they find $i^* \geq 3$. Other results obtained for 6T are also in good agreement with the results reported here. Taking into account the similarity of the two molecules the calculated diffusion barrier for 6T on 6T(100) of 0.063 eV [138] is on good agreement with the one obtained in this work for 6P.

Such a level depended Ehrlich-Schwöbel-Barrier, as it is observed here, requires a strong substrate film interaction that is gradually attenuated by the film. Therefore, organic thin films are good candidates for the observation of such a mechanism. For 6P the level depended Ehrlich-Schwöbel-Barrier leads to a transition from a more layer by layer like growth mode to mound growth that can be explained by the Zeno-effect.

3.3 Para-sexiphenyl on amorphous SiO$_2$

The samples used in this section were grown under supervision of Roland Resel by Ondrej Langyel, David Gundlach and Kurt Matoy, Inst. of Semiconductor Physics, TU-Graz and kindly given to us for AFM investigations.

3.3.1 Influence of different growth rates

Figure 3.49 shows the morphology of a 6P thin film grown on SiO$_2$ by physical vapor deposition. The growth temperature was 150 °C and the film thickness is 50 nm. The

growth rate used was 24 nm/min.

Figure 3.49c shows a detailed image. Deep trenches are clearly visible. From figure 3.49d the cross sectional shape and the terraces can be seen. Figure 3.49b shows the evaluation of the relevant roughness parameters using both the well known form of (2.8) and the modified form (2.10) to fit the HHCF. The modified HHCF fits the data perfectly and gives a average mound separation of 875 nm. The shape of these mounds is similar to the ones found on the ion bombarded mica surface, and are the result of the same growth mechanism.

A second film was grown with the same film thickness but a lower evaporation rate. Figure 3.50 displays the resulting morphology when the growth rate is reduced to 2.4 nm/min while all other parameters are held constant. From figure 3.50a as well as from the results obtained by from the HHCF (shown in figure 3.50b) one can easily see that the reduced growth rate leads to a reduction of the mound density as expected from kinetic nucleation theory (see (1.5). The mound separation is increased from 875 nm to 1150 nm, and the rms-roughness is decreased from $\approx$10 nm to $\approx$8 nm for the film with the slower evaporation rate. Figure 3.51 shows a 3D representation of the mound morphology. The typical Poisson shaped mounds formed by terraces of upright standing molecules can be seen.

Using the fundamental relation (1.5) for the nucleation density we can calculate the critical nucleus size for this temperature. In figure 3.52 the nucleation density $N = 1/\lambda^2$ is plotted versus the flux of incoming molecules. The slope of this line gives the exponent $i^*/d(i^* + 2) = 0.25$. $d = 2$ and therefore $i^* = 2$.

Two things have to be kept in mind when considering this result. Unfortunately, only two data points are available for the fit. Nevertheless, the result fits surprisingly good to $i^* = 2$. This is higher than the value that has been assumed for the determination of the second layer nucleation in section 3.2.4 on mica. However, the films there where grown at RT. Increasing the growth temperature by 120 °C requires more bonds to form a stable nucleus. This well known behaviour, has been seen in inorganic epitaxy as well as organic homoepitaxy [138].

We can use this value for i^* in (1.5) and calculate the ESB for 6P thin films grown on SiO$_2$. The values for the top terrace diameter can be extracted from the obtained AFM images. To unambiguously find the top terrace, an edge enhancement filter is used. The size of the top terrace is then easily measured from images like the one shown in figure 3.53.

The diameter of the top terrace is 60 nm±14 nm for the sample with the high evaporation rate and 81 nm±15 nm for the sample with the lower evaporation speed. Together with the measured mound separation we can estimate the ESB to be 0.71 eV±0.07 eV. These result is well inside the error given for the previous analysis for 6P thin films grown on ion bombarded mica(001) surfaces at RT.
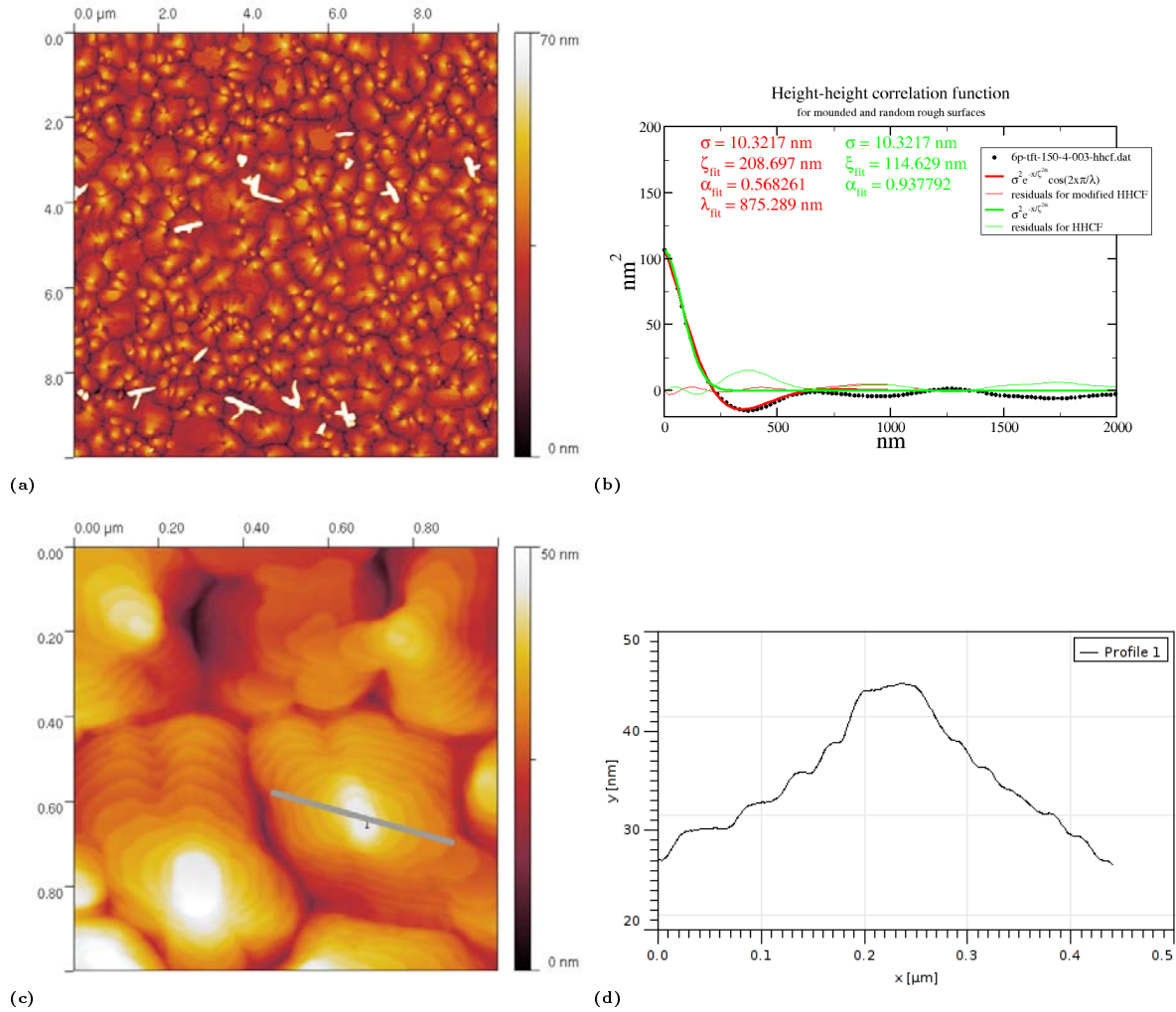
Figure 3.49: (a) morphology of a 50 nm thick 6P film grown at 150 °C on SiO$_2$ with a deposition rate of 24 nm/min. (b) HHCF including fits for a random rough surface and a mounded surface. (c) detailed AFM image of the mounded surface, and (d) cross section showing the cross sectional mound shape.
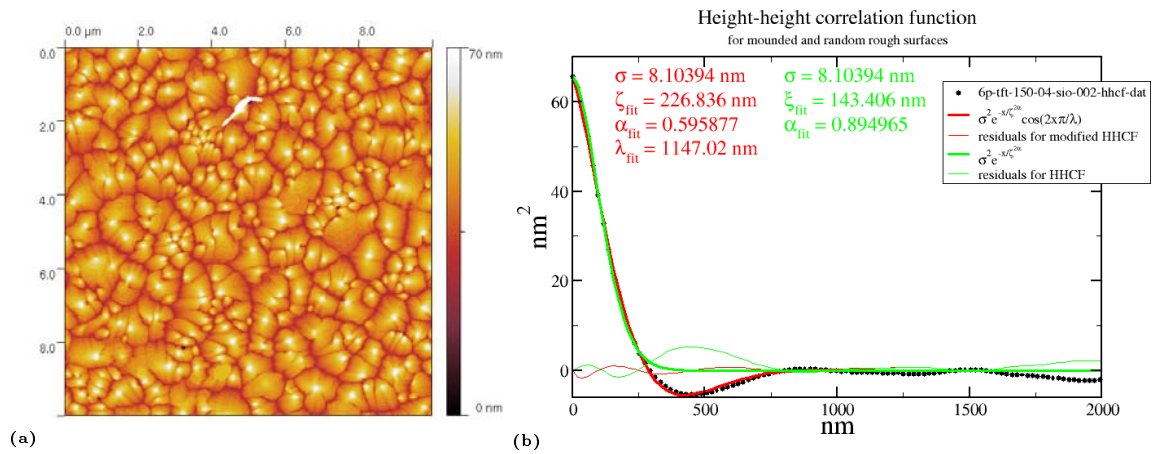
Figure 3.50: (a) morphology of a 50 nm thick 6P film grown at 150 °C on SiO$_2$ with a deposition rate of 2.4 nm/min. (b) HHCF including fits for a random rough surface and a mounded surface.
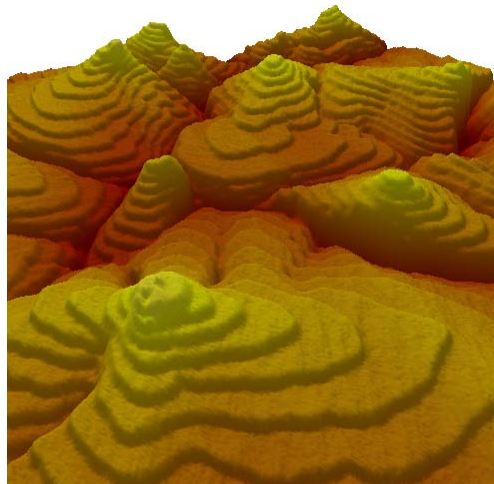
Figure 3.51: 3D representation of the mounded morphology
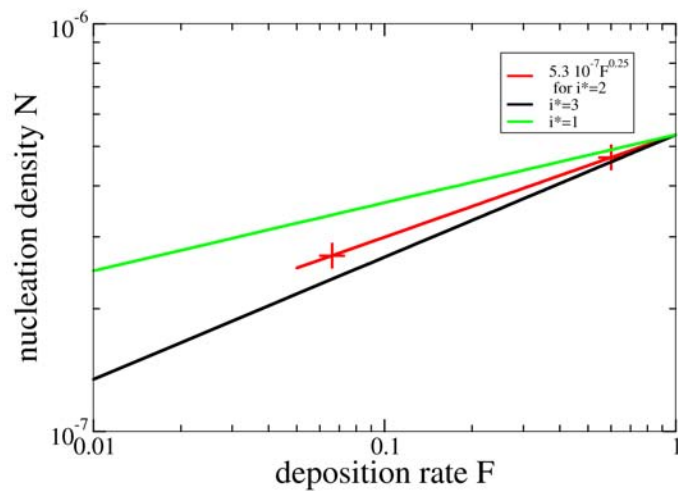
Figure 3.52: Nucleation density N versus flux F of incoming particles in units of molecular adsorption sites. Fits for $i^* = 1, 2,$ and 3 are shown.
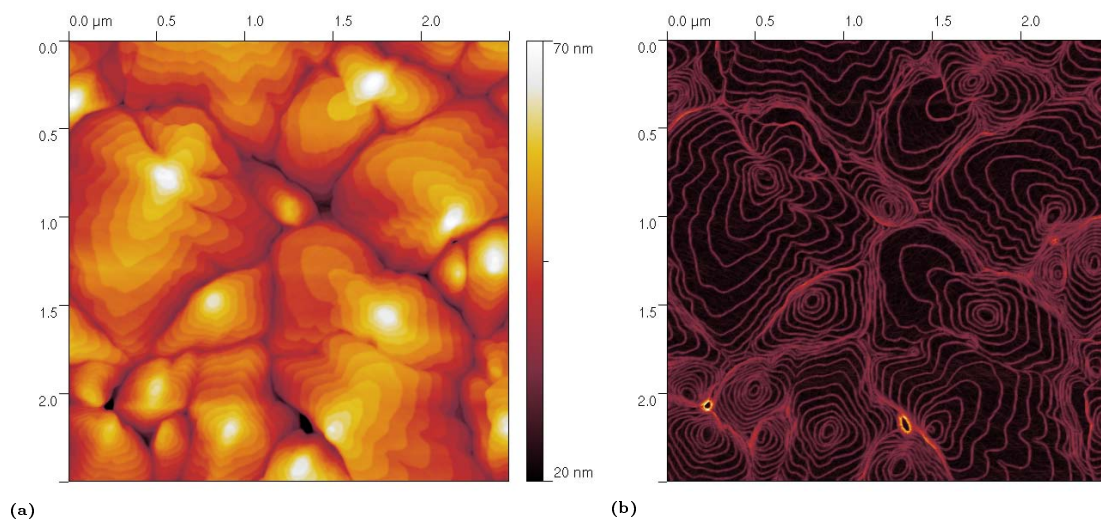
Figure 3.53: Terraces in a 50 nm 6P thin film grown on SiO_2 at 150 °C with a evaporation rate of 2.4 nm/min. (a) morphology and (b) only the edges of the terraces.

3.4 Para-sexiphenyl on Gold(111)

This section will discuss results obtained by AFM for the growth of 6P on the Au(111) surface. The results have been published in [53]. For the effect of carbon pre coverage on the morphology of phenyl thin films grown on gold the reader is referred to the following publication by the auther on quaterphenyl growth [139] as well as additional publications concerning the structure of the grown films [140, 141].

3.4.1 Influence of growth temperature

To understand the changes in morphology when changing the substrate temperature a number of samples were grown at different deposition temperatures. Figure 3.54 gives an overview.

Figure 3.54a shows the morphology of a 100 nm thick 6P film grown at 93 K and measured at RT. The film is characterized by round crystallites. Figure 3.55 shows the result of a watershed grain size analysis. The majority of the crystallites has a mean radius of 24 nm±10 nm. The crystallites show no preferential orientation. This is in full accordance with x-ray investigations that showed that the $\Theta/2\Theta$ scan can be fitted well by a powder pattern. Several distinct peaks corresponding to several different crystallites formed by molecules lying on the surface as well as crystallites with their molecules standing upright can be observed. However, they seem to have no preferential orientation on the surface. All these investigations were carried out at room temperature. A combined TDS and X-ray photoelectron spectroscopy (XPS) investigation, carried out by S. Müllegger, showed that the heating to room temperature will not substantially influence the film morphology. By monitoring the Au $4j$ signal during warm up it could be shown that no substantial reordering takes place up to 350 K [53]. The onset of desorption is at roughly 450 K.

Figure 3.56 shows the watershed analysis done for a 30 nm thick film grown at 300 K. The grain radius distribution is fitted by two Gaussian fits. Comparing the result with figure 3.55b the former small second peak at larger grain radii (42 nm for 93 K) shifts and becomes the dominant feature at 53 nm±24 nm, indicating a profound shift to larger grains for the higher temperature film.

Figure 3.57 shows the result of a 2D FFT of a 10 µm large AFM image obtained from the film grown at 300 K. In contrast to the FFT of the film grown at 93 K (not shown) it is not only characterized by a ring but also by two peaks, indicating a higher order in this direction. Figure 3.57b shows cross sections through the 2D-FFT. While the cross section in the peak direction (black) shows a clear peak the ones obtained for 30°and 90°off this direction do not show any pronounced features. The directions were chosen in such a way that it becomes clear to off the peak direction only a small ring remains. This difference in the morphological order is not surprising as the film grown at the higher temperature also shows a clear orientation relation to the substrate in x-ray investigations. $\Theta/2\Theta$ scan revealed the preferred $(21\bar{3})$ plane to the substrate and aligned with the sixfold symmetric Au(111) surface [78]. However, only one clear pair of peaks is observed in the FFT. The overall shape of the FFT nevertheless is hexagonal

(a)

(b)

(c)

(d)
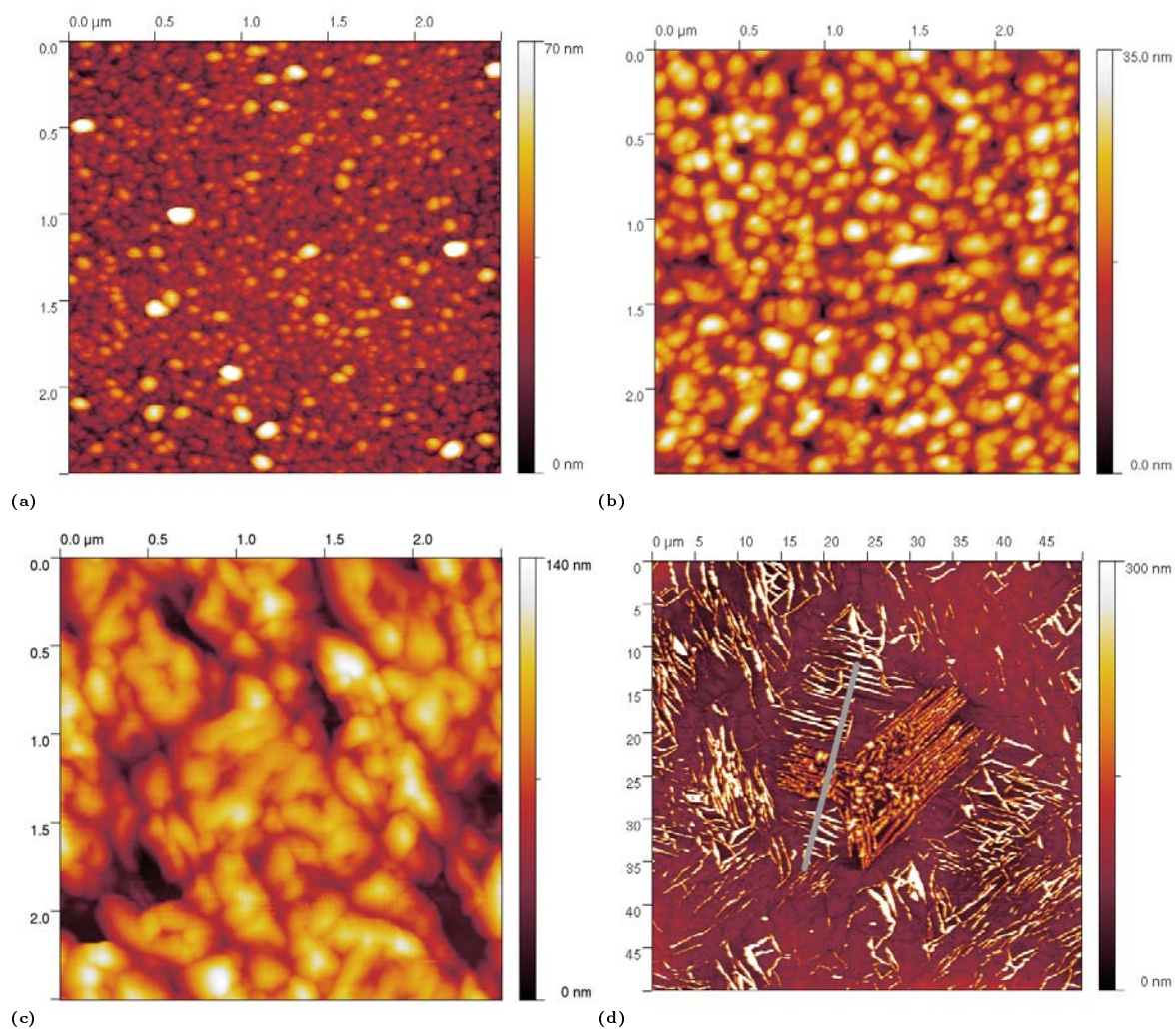
Figure 3.54: Morphology at RT for different 6P films grown at various temperatures on a Au(111) surface. (a) 100 nm grown at 93 K, (b) 30 nm grown at 300 K, (c) 30 nm grown at 330 K, and (d) 30 nm grown at 430 K (20 times larger lateral scale).

(a)

(b)
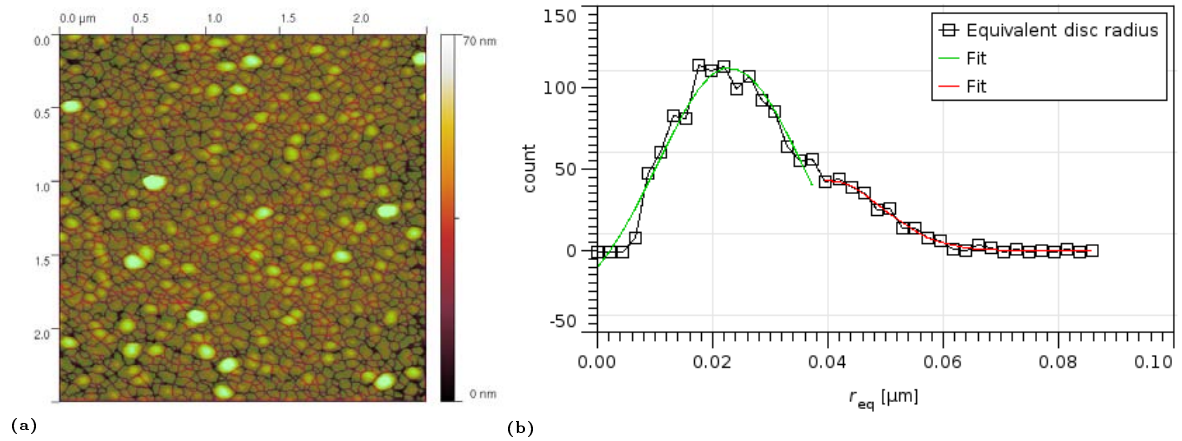
Figure 3.55: (a) watershed mask for 3.54a showing the individual grains and (b) average grain radius. Two Gaussian fits are included at 24 nm±10 nm (green) and 42 nm±10 nm (red).

(a)

(b)
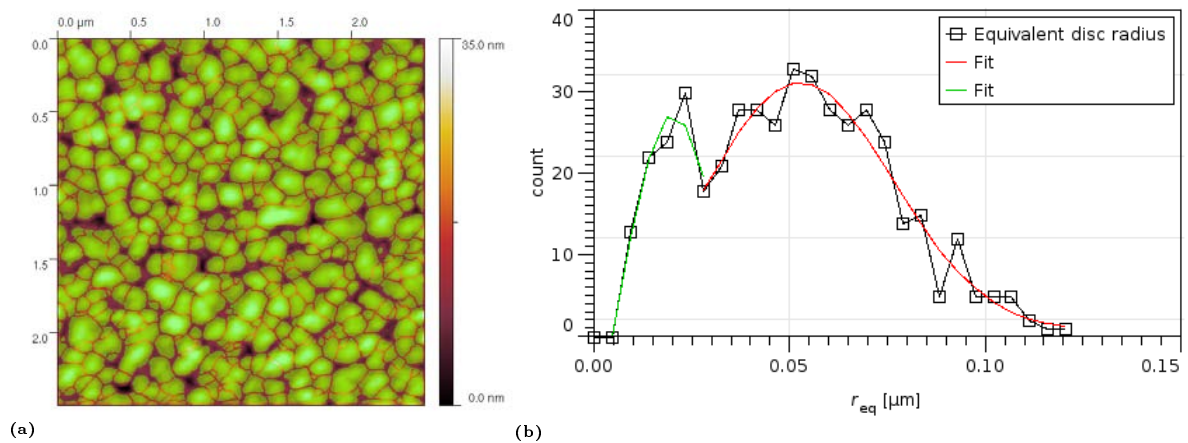
Figure 3.56: (a) watershed mask for 3.54b showing the individual grains and (b) average grain radius. Two Gaussian fits are included at 20 nm±15 nm (green) and 53 nm±24 nm (red).

96

indicating that the morphology indeed is correlated to the underlying surface structure.

Increasing the temperature further by only 30 K to 330 K results in dramatic changes to the morphology. The morphology shown in figure 3.54c is characterized by organic looking patches of weakly oriented 6P crystallites separated by large holes probably reaching down to the substrate. The width of the holes varies but lies between 100 nm and 500 nm. Their length can vary from only a few hundred nm up to several μm. Figure 3.58 gives a larger overview over the morphology observed. The average size of the patches formed by randomly oriented crystallites is about 2 μm. These patches are separated by the holes mentioned above. AFM doesn't give a clear answer to the question what can be found at the bottom of the holes. However, cross sections (not shown) done at the bottom of the holes indicate that they might contain some 6P. A cross section on the Au(111) surface should give a flat structureless line which was not the case. A small part of the surface is covered by a third structure, as can be seen cross section presented in figure 3.58b. It shows two cross sections one through one of the organic looking patches already discussed, and one along one of the randomly placed straight needles. The are formed by larger building blocks and therefore show a smoother cross section. The more important fact however is, that they are strongly oriented in one direction. However, they do not show any packing and can be found in random positions all over the sample. Several of them, oriented from bottom right to top left, can be found in figure 3.58a. The needles are obviously the result of the higher crystallinity also observed by x-ray investigations. $\Theta/2\Theta$ scans show a much clearer $(21\bar{3})$ peak and also the pole figure taken for this plane is clearer compared to the one obtained from the film grown at 300 K [78].

Increasing the temperature further to 430 K results in the expected increase of crystallinity observable by x-ray but also by AFM. As a consequence the size of figure 3.54d had to be chosen 20 times larger than the other images in figure 3.54. Large patches of
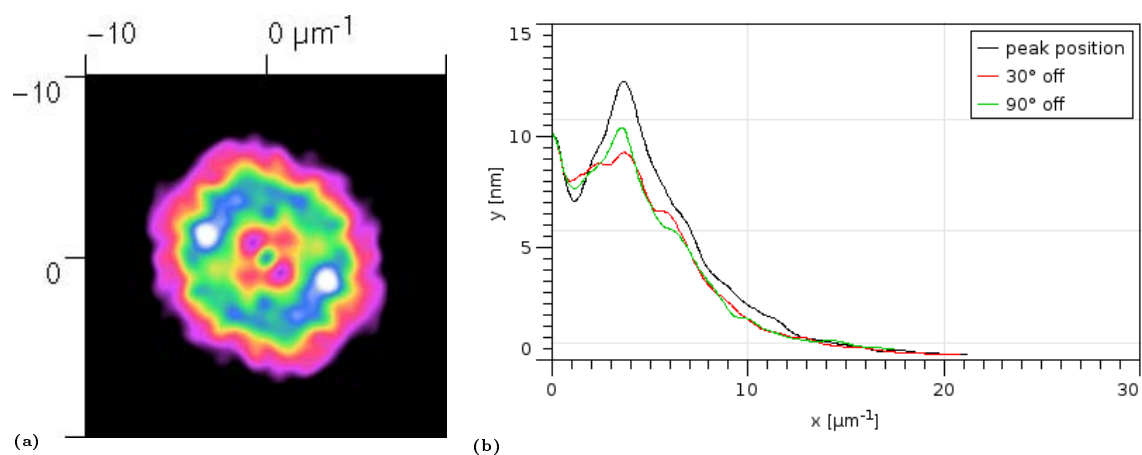
Figure 3.57: (a) 2D FFT of a 10 μm large AFM obtained from a 30 nm thick 6P film grown at 300 K (see figure 3.54b). (b) cross sections through the 2D FFT at the peak position (black), 30°(red), and 90°(green) off.
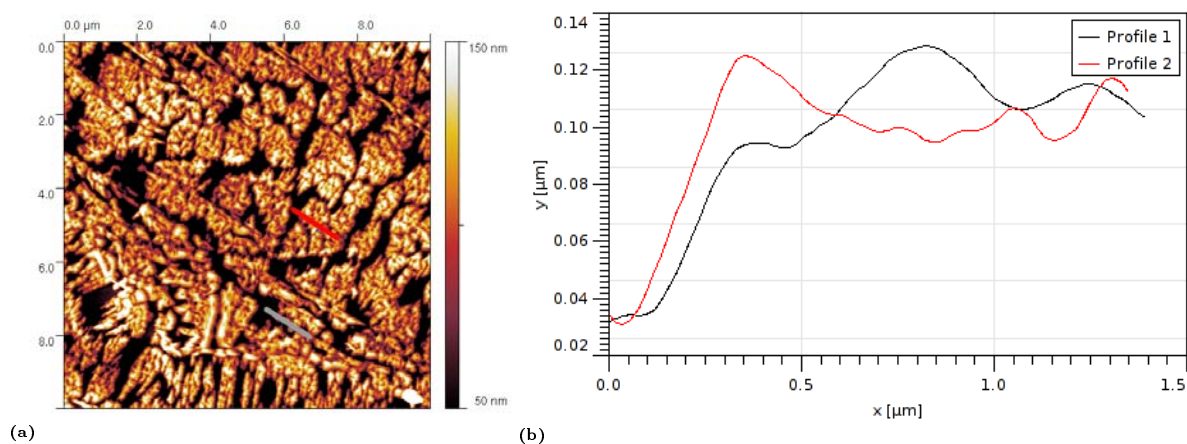
Figure 3.58: 10 µm large AFM image of a 30 nm 6P thin film grown at 330 K on Au(111). 2 µm large patches of small randomly oriented crystallites separated by holes probably filled with 6P. Further more some straight 6P needles formed by larger crystallites can be seen. (b) cross section along a needle (black) and through one of the organic looking patches (red).

parallel oriented 6P needles characterize the surface morphology. The length of the 6P needles is between 1 µm-2 µm up to 15 µm. However, as can be seen from the detailed AFM image in figure 3.59, the needles are neither uniform nor completely straight. They are built from smaller subneedles which are slightly misoriented with respect to each other and are sometimes curved. The angle between the individual parts of a long needle changes. Angles of about 20° and multiples of this value seem to be common. However, the orientation of the subneedles oscillates around a main direction. Although the needles are not straight the 2D FFT presented in figure 3.60b clearly shows the primary sixfold symmetric orientation of the needles induced by the sixfold symmetry of the underlying Gold (111) surface. The height of the needles (between 200 nm and 500 nm) is correlated to the distance between them. Comparing the patch of needles in the center of figure 3.54d with the ones on the rim of the image one can see that in general higher needles are separated further. This is also obvious from the cross section shown in figure 3.60a.

The area between the needles is covered by mounds of upright standing molecules up to 50 nm high. Figure 3.61 shows an enlarged part of the area between the needles and two cross sections. A number of growth mounds can be found on the surface. The cross section shown in figure 3.61b is taken on the upper part of such a mound and shows the 2.7 nm large step height, typical for upright standing molecules. One can clearly see that the shape of these mounds is characterized by steep trenches visible in the cross section shown in figure 3.61c. These steep trenches were already discussed in an sections 1.2.2 and 3.2.4 and are a hint towards a high step edge barrier, inhibiting or at least reducing interlayer transport.

The observed coexistence of mounds formed from upright standing molecules and
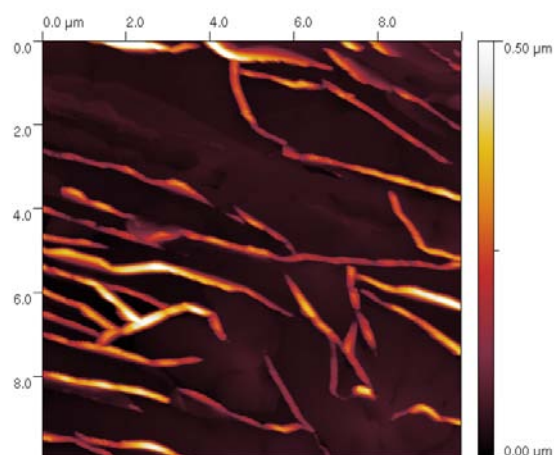
Figure 3.59: 10 µm by 10 µm large AFM image showing the kinked nature of the long 6P needles found at 430 K.

(a)

(b)
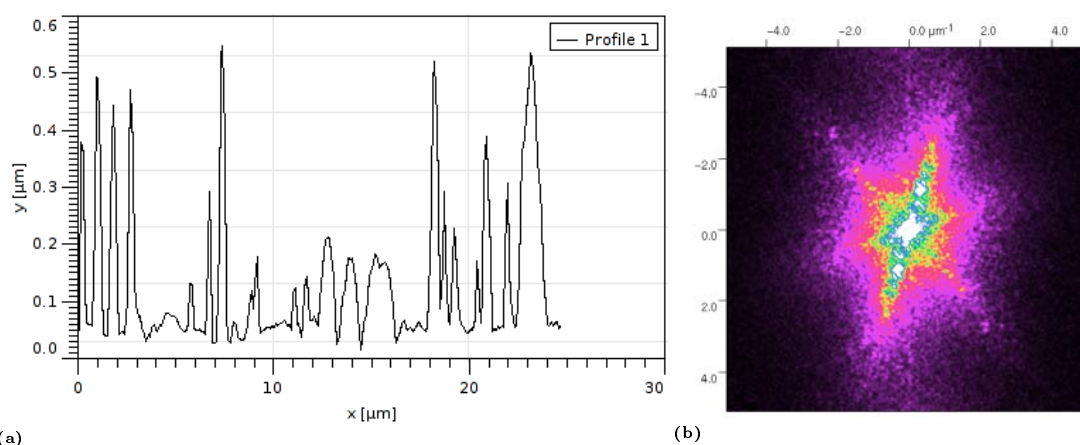
Figure 3.60: (a) cross section through figure 3.54d. (b) 2D FFT of figure 3.54d. A clear six fold symmetric structure can be observed.

needles of lying down molecules is often observed. As the amount of upright standing molecules increases with temperature this can be related to an increased nucleation property of such mounds on an increasing number of defects found on the hotter sample surface.
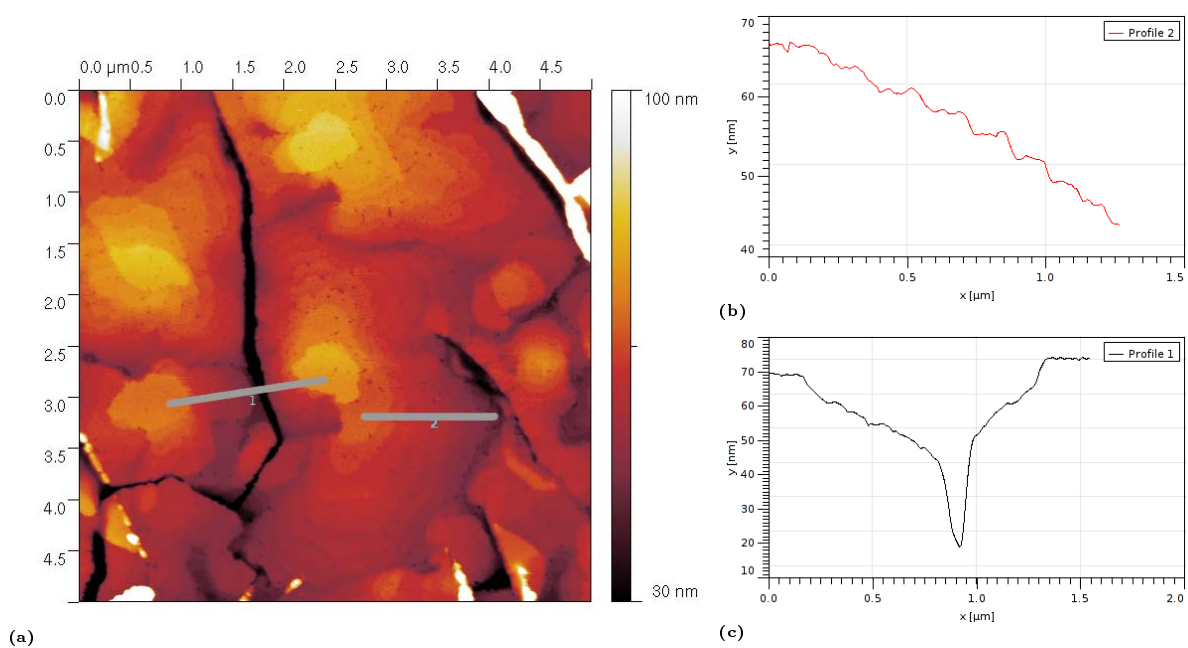
Figure 3.61: (a) AFM image of 30 nm thick 6P film grown at 430 K on Au(111). The area between the needles is covered by mounds formed by upright standing molecules. (b) and (c) show the marked cross sections

4 Discussion

Growth of 6P can be roughly divided into two sections.

- Lying molecules generally lead to the formation of crystallites and large anisotropic needles or chains of crystallites. In many cases these structures grow on a wetting layer also formed by lying molecules.

- Repeated 2D nucleation is the dominant mechanism when upright standing molecules are found on the surface. Depending on the properties of the substrate and film thickness isotropic mound formation or diffusion controlled formation of anisotropic layers occurs.

The reasons and implications of these two growth modes will be discussed separately. Finally some remarks will be given on the transition from the one to the other and how this might be controlled.

4.1 Structures formed by lying molecules

The morphology of 6P thin films formed from lying molecules is characterized by a high degree of anisotropy. On all crystalline substrates investigated formation of anisotropic nanofibers happens. In the following, a number of common properties of the structures are listed:

Anisotropy

Formation of highly anisotropic structures is observed on all three substrates (mica(001), TiO_2(110)-(1x1), and Au(111)). The reason for the pronounced needle or chain shape lies in the anisotropy of the building block. The 6P molecule has its highly reactive π system stretched along the long molecular axis, parallel to the molecular plane. Especially the small end of the molecule – terminated by a single hydrogen – has a very low binding probability. The preferred binding site for a molecule approaching a crystallite is therefore the π terminated crystal facet. A seed formed by lying molecules will therefore grow faster perpendicular to the molecular axis than parallel to it. This will finally lead to the observed anisotropic morphology.

Substrate order

An ordered substrate is necessary for the formation of structures built from lying molecules. However, it is important to remember that also crystalline or polycrystalline films of upright standing molecules can act themselve as the necessary ordered substrate. The exposed (001) plane of the upright standing molecules can act as a highly ordered substrate for the formation of 6P needles. This can be seen in case of 6P on ion bombarded mica. During the initial growth, no needles or chains can be found (see figure. 3.33). However, the µm large islands formed in a later growth stage can now act as a well ordered substrate for the formation of 6P needles (see figure 3.34). An interesting experiment demonstrating the importance of an ordered substrate was carried out with para-quaterphenyl (4P). This molecule – similar to 6P but only made from 4 phenyl rings – has been grown on clean and carbon contaminated Au(111) surfaces. With increasing carbon deposition a loss of the strict alignment of the molecules on the gold substrate is observed. This results in curved instead of straight needles. At the saturation carbon coverage, films of upright standing molecules are formed [139, 141].

Wetting layer

The presence of a wetting layer can change the morphology from a needle like to chain like. In the absence of a wetting layer long crystalline needles are preferred. This can be seen for the growth of 6P on TiO_2 at RT (section 3.1.1 on page 41) or 6P on KCl(001) [109]. Whenever there is a wetting layer present the needles start to segment, like in the case of Au(111) (see section 3.4 on page 94) where a wetting layer is formed [52] or completely turn into the observed chains of crystallites found on freshly cleaved mica(001) (see section 3.2.1 on page 52).

A prototype experiment for the chain formation is the growth of 6P on freshly cleaved mica(001). Two peculiarities lead to formation of the crystallite chains observed for this case:

1. Formation of strain controlled crystallites due to lattice mismatch between the mica substrate and the 6P. This leads to uniform crystallites which all have a similar epitaxial but slightly different alignment with respect to each other [48].

2. The formation of a wetting layer that allows the easy propagation of the strain fields induced by the crystallites [69].

With ongoing deposition the increasing strain in the wetting layer is released by the formation of a defect network and subsequent rearrangement of the crystallites [115].

Substrate induced orientation

Substrate induced orientation of one-dimensional structures is observed for all three cases investigated where a crystalline substrate was used (mica(001), TiO_2(110)-(1x1), and Gold(111)). The 6 fold symmetric Gold(111) surface allows a large number (12 is

common, but the exact number depends on the growth temperature [78]) of different orientations. Using substrates with reduced symmetry like mica(001) and TiO_2(110)-(1x1) leads to the formation of exclusively parallel aligned nanofibers. In the case of mica(001) two orientation of needles are observed. Each single step will turn the orientation forth and back by 120°between the two possible directions. A particularity of the mica unit cell leads to the fact that only two orientations can exist. The third one, that one would expect between them, again rotated by 120°, is missing. For TiO_2(110)-(1x1) the number of needle directions is reduced further to only one single orientation. The bridging oxygen rows on the substrate allow only one alignment for lying molecules.

Aspect ratio of the nanostructures

The aspect ratio can be influenced by changing the deposition conditions. An increase in substrate temperature usually leads to higher but shorter structures. However, by controlling substrate temperature, and deposition rate as well as the presence or absence of a wetting layer, the length of the nanofibers can be changed from sub-μm to millimeter [142].

Substrate temperature

Low temperatures promote the lying orientation and subsequent formation of one-dimensional nanofibers. Although the growth of 6P on mica(001) seems to lead to nanofibers independent of the substrate temperature this is not the case for the more metallic substrates like TiO_2 and Gold. On Gold an increasing number of molecules adopts an upright standing orientation at 160 °C and on TiO_2 all the molecules form upright standing structures at 145 °C. At higher temperatures the molecules can overcome the substrate interaction and present their low energy plane (the [001] plane, terminated by hydrogen atoms) towards the substrate. The temperature must be high enough to allow the reorientation of the molecules. For clean mica(001) the investigated temperature range is to small to overcome the strong dipole-quadrupole interaction, and structures formed by lying molecules are found independent of the growth temperature.

4.2 Structures formed by standing molecules

Two cases should be distinguished for the formation of films formed by upright standing molecules.

1. Standing molecules on ordered substrates

2. Standing molecules on disordered substrates

Symmetry of the substrate

On substrates with reduced symmetry like the $TiO_2(110)$-(1x1) surface, a delicate balance between sticking anisotropy and diffusion anisotropy leads to the formation of large anisotropic structures. Both of these effects are also present at RT were crystallites of lying molecules are formed. When increasing the temperature the molecules can overcome the attraction of the substrate and form stable islands of upright standing molecules. For the incorporation of an additional molecule into an island of upright standing 6P molecules the sticking anisotropy is reduced to almost zero. The shape of the islands is controlled by the diffusion anisotropy, and the observed long oriented stripes of 6P are formed [55, 108].

It is important to note that also for an island of upright standing molecules a small but observable sticking anisotropy exists, as can be seen from the elongated shape of the small crystallites between the stripes. However, this is finally overcome by the diffusion anisotropy and these crystallites disappear [110]. The shape anisotropy is lost for subsequent layers as the second layer of 6P grows on 6P(001) which is of higher symmetry than the underlying $TiO_2(110)$-(1x1) surface.

Recent Reflectance Difference Spectroscopy (RDS) studies showed that for extremely low coverages (up to 1 ML of lying molecules) flat lying molecules are found on the surface [143]. Phase images obtained in this work indicate (figure 3.11 on page 49) no hint for the existence of such a wetting layer in thicker films. Although, phase imaging might not be able to distinguish between a strongly bound layer of lying molecules and the substrate, its capability of detecting the existence of a wetting layer in other systems was demonstrated. For example, no phase contrast was obtained for HWE grown 6P chains on mica(001), were a wetting layer mediates the chain formation. On the other hand a strong phase shift is observed for 6P on KCl(001) were no wetting layer exists [109, 144].

Disordered substrates

On disordered substrates the 6P molecules tend to stand upright. It has been shown that by destroying the structure of the top most surface layer on mica an upright molecular orientation can be adopted.

Mound formation

Mound formation is observed in this investigation for all thick films (>1 ML of upright molecules) of upright standing 6P molecules. This includes ion bombarded mica, Gold(111), and SiO_2 at elevated temperatures. For TiO_2, no thick films were investigated. However, even so large terraces of standing 6P are formed for the first ML. The second, third and fourth layer form long before the first layer has closed. This repeated 2D nucleation is a strong hint for the existence of a step edge barrier.

For the thicker films on ion bombarded mica, the Zeno model was used to calculate the step edge barrier or Ehrlich Schwöbel Barrier of 6P. To the best of our knowledge this is the first time that such an important parameter has been calculated from experimental

data in organic semiconductor thin film growth. The result of 0.67 eV for the additional barrier that a molecule has to overcome is very high compared to the 0.11 eV for the diffusion barrier as calculated by molecular dynamics simulations. However, a high step edge barrier is necessary to obtain mounds with a cross section that can be fitted by a cumulative Poisson distribution. For example the mounds found on Au(111) are separated by 50 nm deep trenches. This requires a very effective suppression of interlayer mass transport.

The strongest argument against the proposed scenario is the formation of 6P needles on the 6P(001) surface. It is important to note that no needles are found directly on the ion bombarded mica surface. Needle formation can only happen on the 6P islands. Furthermore, each needle is confined to one island. Growing onto the neighbouring island is virtually impossible as the neighboring island has a different orientation and would require the needle to curve. Although related events have been observed elsewhere [139] it is a very unlikely and unfavorable event. The lateral size of the needles is therefore limited. Nevertheless, with ongoing deposition a large quantity of molecules does not take part in the mound formation and is incorporated into the needles. This is equivalent to a reduction of the flux of incoming molecules. Reducing the flux F in (1.20) by a factor of 2 has no influence on the result. With other words, to reduce the rate ν' at which a molecule will jump down by a factor of two, the flux must be reduced by six orders of magnitude. However, the flux enters the final calculation twice in a linear fashion. The result is therefore independent of the actual flux as long as the time between two deposition events is larger than the residence time of a particle (lonely adatom model (LAM)) [34].

In principle one could think of a scenario were the chains act as promoters for upward diffusion. Depending on the efficency of this process it would lead to differently shaped islands. The consequence of a strong upward diffusion is a low growth rate for the bottom terraces as the molecules will be transported away from there and to the top. As a result instead of a Poisson shaped cross section a more linear cross section would form. However, for the calculation of the shape only islands without needles on top were used.

Mound formation following the Zeno model was also observed for 6P on SiO_2. In the later system it was also possible to calculate the critical nucleus size. The obtained value of $i^* = 2$ is not contradicting the assumed case of $i^* = 1$ at RT since the growth was performed at elevated temperature (150 °C). Also recent results obtained on the very similar 6T show that the critical nucleus size at RT can be assumed to be one [138].

4.3 Transition from lying to standing molecules

With the exception of SiO_2 it could be shown that upright as well as standing molecules can be grown on the same substrate. To change the orientation of the molecules three different routes can be followed

1. Increasing the temperature turns the molecules into the upright position on the investigated Au and TiO_2 surfaces.

2. The effect of surfactants has been demonstrated on mica(001) surfaces.

3. Destroying the anisotropy of the substrates also leads to upright standing molecules on mica.

The formation of organic semiconductor nanostructures is governed by the reduction of the number of exposed π systems. This can effectively be done by forming a layer of upright standing molecules. However, at low temperatures or when ever there is a strong interaction with the substrate this is impossible. For the investigated cases the following mechanisms are involved in the reorientation of the molecules:

Increasing the growth temperature allows the molecules to overcome the binding with the highly reactive substrate as observed for Au [53, 78] and TiO$_2$ [55, 108].

Reduced dipole quadrupole interaction can be observed when a surfactant is used on mica(001) [69, 117].

Reduced alignment between the molecules – usually enforced by the substrate anisotropy – also leads to the formation of structures formed by upright molecules [69].

This transition can be abrupt, but is continuous in most cases and leads to the coexistence of both orientations [52, 139, 141].

It is important to realize that the situation during the formation of both types of structures – formed by lying or standing – is the very similar. Diffusion and incorporation of the molecules happens preferentially on the edges of a (001) terrace.

This is obvious in the case of upright standing molecules. In this case the high Ehrlich Schwöbel Barrier hinders interlayer mass transport and growth mounds are formed by repeated nucleation as discussed in the preceding section. This leads to the situation that diffusion along the rim of the island is easy while other diffusion paths are unfavorable (see figure 4.1a). As a result the molecules are mainly incorporated into the π terminated side walls of the island. It is important to understand that – at least up to a certain consideration – the situation for lying down molecules is the same. Again, diffusion and incorporation are preferred at the π terminated facets of the needle (see figure 4.1b). However, one could look at the needle as an upright standing island, with the molecules turned parallel to the substrate. The same fast growth directions will occur and the needle will start to grow vertically and laterally in only one direction. For the needles, the width (the direction parallel to long molecular axis) is the slow growth direction. The same is true for the islands were the molecular axis is vertical to the substrate.
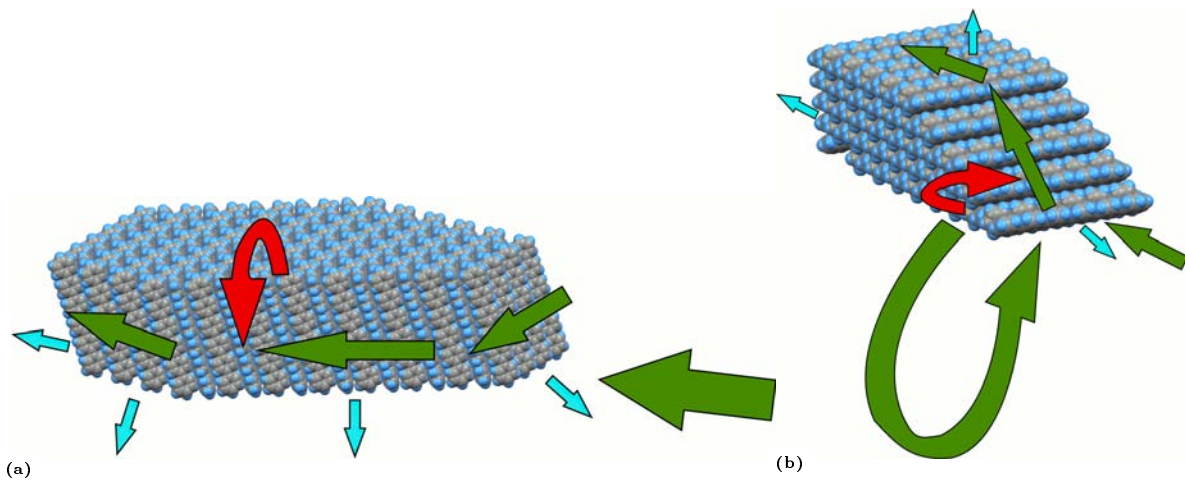
Figure 4.1: Low and high probability diffusion path's for (a) mounds formed by standing molecules and (b) needles formed by lying molecules. Green arrows indicate easy diffusion paths (including diffusion paths without interaction with islands or needles like in the case of the large green path for lying molecules) while red arrows indicate unfavorable paths. The light blue arrows show the resulting fast growth directions.

5 Summary

Analysing the growth of para-sexiphenyl on a variety of ordered and disordered substrates it has been demonstrated in this work that one can follow the general procedures already known from inorganic growth, to describe the growth processes in organic semiconductor thin film growth. However, especially the anisotropy of the building blocks is not covered in classical epitaxial growth theory. In the case of organic molecules this is the most important parameter and in all three investigated cases the anisotropy of the molecule plays an important role for the resulting growth morphologies.

For the case of 6P on $TiO_2(110)$-(1x1) the anisotropy of the building blocks in combination with the substrate anisotropy leads to the formation of oriented 6P needles. Increasing the temperature, diffusion anisotropy induced by the substrate is dominating the growth. However, even at elevated temperatures a sticking anisotropy originating in the crystal structure of the formed 6P film can be observed for the small islands of upright molecules.

In the case of mica(001) the quadrupol moment that is induced by the one dimensional stretched π system orients the molecules on the surface. In the presence of a wetting layer, strain controlled crystallites move as complete entities on the surface and form the one-dimensional crystallite chains.

On anisotropic surfaces the molecules are standing nearly upright and mounds are formed. This circumstance can be explained with the help of a formalism taken from inorganic homoepitaxy. This so called Zeno model allowed for the first time in organic semiconductor thin film growth the calculation of an Ehrlich Schwöbel Barrier. The consequences of the high value for the step edge barrier for the application of organic semiconductors were already discussed. However, although this example shows that one can apply theories established in inorganic epitaxy for the description of organic epitaxy, it has to be emphasized that the underlying details are certainly much more complex in the case of organic thin films. This is clear if one just thinks of the fact that an anisotropic particle like 6P has at least one additional degree of freedom. The step edge barrier is different for molecules approaching the surface with their long axis parallel to the edge than for molecules with their long axis perpendicular to the step edge.

Another consequence of the not zero dimensional nature of the molecules is the possibility for the existence of a level depended step edge barrier. It has been shown in this work, that changes in the molecular tilt angle in the first few layers lead to different values for the Ehrlich Schwöbel Barrier. The change in interaction is related to the different angle between the π-system of the diffusing molecule and the exposed π-system of the molecules forming the step edge. From the results presented in [134] it is furthermore clear that also the electronic properties of the resulting film will be

influenced by such a behaviour.

We have shown that in most cases by carefully selecting the growth conditions one can grow sexi-phenyl thin films formed by upright as well lying down molecules. This is important for future devices since it has been shown that the molecular orientation of the active layer in organic electronics is crucial for optimum device performance.

The formation of highly anisotropic structures, typical for the growth of 6P, might be unfavorable at first glance but opens a wide field of new applications. These nanofibers might act as waveguides that could interconnect different parts of optical relays. As the fibers can also emit light and even show lasing they could be used as highly anisotropic lasers or optical elements in general.

The results obtained on films formed by upright standing molecules show, however, that growing perfect layer by layer films required for high performance electronic devices is at least difficult. Several routes to overcome the mound formation can be thought of. The use of surfactants (which in principle could also act as dopant's at the same time) might be a promising route to control the height of the step edge barrier and allow a net diffusion to the lower terrace and subsequently layer-by-layer growth. A combined self organization and nanostructuring approach could also reduce the problems inherit to mound formation. If one succeeds to grow grains of the size or larger than the typical channel length in a controlled way the film would be single crystalline on the transistor length scale. Hyperthermal beams also show a good potential for the preparation of smooth films of organic semiconductors [145].

Figure 5.1 presents an attempt to compile the results in a condensed form. Them main morphological features and molecular orientation are shown for each investigated surface. The most important growth mechanisms are also assigned. However, only a very crude assignment can be made in such a table, the reader is therefore, refereed to the corresponding sections for details.

	Main morphological feature	Molecular orientation	Sticking anisotropy	Diffusion anisotropy	Ehrlich Schwöbel Barrier	see section
TiO$_2$(110)-(1x1) RT	N	–	✔	✓	✗	3.1.1
TiO$_2$(110)-(1x1) HT	C,2D,(M)	|	✔	✔	✗	3.1.2
mica(001)	C,Ch,N	–	✔	?	✗	3.2.1-3.2.3
mica(001) + carbon	2D	|	?	✗	?	3.2.4
disorderd mica	M(N)	|	?	✗	✔	3.2.4
SiO$_2$	M(N)	|	?	✗	✔	3.3
Au(111) LT	C(N)	–	✓	✗	✗	3.4.1
Au(111) HT	NM	–|	✓	✗	✔	3.4.1

Table 5.1: Summary of the results. Morphology: C...crystals, N...needles, Ch...crystallite chains, $2D$...2D nucleation, M...mounds $()$...morphology in addition to the major feature. 6P orientation: –...lying, |...upright. ✔...main mechanism, ✓...also relevant, ✗...plays no role, $?$...role unclear.

List of Acronyms

6P   **para-sexiphenyl:** Organic semiconductor consisting out of six phenyl rings connected by single bonds, 4, 15

6T   **sexithiophene:**, 88

AFM   **Atomic Force Microscopy:** a very high-resolution type of scanning probe microscope. The main part of the AFM is a micronscale cantilever with a sharp tip (probe) at its end that is used to scan the specimen surface, 24

Cu-Pc   **copper-phthalocyanine:** is a copper substituted phthalocyanine. The copper is located in the center of the molecular plane., 85

ESB   **Ehrlich-Schwöbel-Barrier:** An additional diffusion energy barrier that a particle has to overcome when it tries to jump to a lower lying terrace, 10, 81, 87, 90

FFM   **Friction Force Microscopy:** Contact mode AFM method that allows to identify areas with different friction, 26, 66

FFT   **Fast Fourier Transformation:**, 32

FM   **Frank-van der Merwe:** or layer by layer growth. Named after Frank and van der Merwe, 7

FWHM   **Full Width at Half Maximum:**, 34

HDF   **Height difference function:** some times also height-height correlation function, 29

HHCF   **Height height correlation function:** sometimes also auto-covariance function, 29

HOMO   **highest occupied molecular orbital:** corresponds to the valence band in inorganic semiconductors (see also LUMO), 2

HOPG   **highly oriented pyrolytic graphite:**, 85

List of Figures

List of Tables

References

[1] Schwoerer, M. and Wolf, H. C. *Organische Molekulare Festkörper – Einführung in die Physik von π-Systemen.* Wiley-VCH, Weinheim, (2005).

[2] Kini, A., Geiser, U., Wang, H., Carlson, K., Williams, J., Kwok, W., Vandervoort, K., Thompson, J., Stupka, D., Jung, D., and Whangbo, M.-H. *Inorg. Chem.* **29**(14), 2555–2557 (1990).

[3] Bao, Z., Feng, Y., Dodabalapur, A., Raju, V., and Lovinger, A. *Chem. Mater.* **9**(6), 1299–1301 (1997).

[4] Rogers, J., Bao, Z., Makhija, A., and Braun, P. *Adv. Mater.* **11**(9), 741–745 (1999).

[5] Kawase, T., Shimoda, T., Newsome, C., Sirringhaus, H., and Friend, R. *Thin Solid Films* **438-439**, 279–287 (2003).

[6] Sirringhaus, H., Kawase, T., Friend, R., Shimoda, T., Inbasekaran, M., Wu, W., and Woo, E. *Science* **290**(5499), 2123–2126 (2000).

[7] Brütting, W., editor. *Physics of Organic Semiconductors.* Wiley-VCH, Weinheim, (2005).

[8] Koller, G., Berkebile, S., Oehzelt, M., Puschnig, P., Ambrosch-Draxl, C., Netzer, F., and Ramsey, M. *Science* **317**(5836), 351–355 (2007).

[9] Müllegger, S. *Adsorption and Thin Film Growth of Oligo-phenylenes on gold surfaces.* PhD thesis, Graz University of Technology, Graz, Austria (2005).

[10] Reese, C. and Bao, Z. *Materials Today* **10**(3), 20–27 March (2007).

[11] Niko, A., Meghdadi, F., Ambrosch-Draxl, C., Vogl, P., and Leising, G. *Synth. Met.* **76**, 177–179 January (1996).

[12] Ambrosch-Draxl, C., Puschnig, P., Resel, R., and Leising, G. *Synth. Met.* **101**(1), 673–674 (1999).

[13] Schroeder, P., Nelson, M., Parkinson, B., and Schlaf, R. *Surf. Sci.* **459**(3), 349–364 (2000).

[14] Puschnig, P., Ambrosch-Draxl, C., Resel, R., and Leising, G. *Synth. Met.* **101**(1), 671–672 (1999).

[15] Yanagi, H., Okamoto, S., and Mikami, T. *Synth. Met.* **91**, 91–93 December (1997).

[16] Zojer, E., Koch, N., Puschnig, P., Meghdadi, F., Niko, A., Resel, R., Ambrosch-Draxl, C., Knupfer, M., Fink, J., Bredas, J., and Leising, G. *Phys. Rev. B: Condens. Matter Mater. Phys.* **61**(24), 16538–16549 (2000).

[17] Mikami, T. and Yanagi, H. *Appl. Phys. Lett.* **73**(5), 563–565 (1998).

[18] Balzer, F., Bordo, V., Simonsen, A., and Rubahn, H.-G. *Phys. Rev. B: Condens. Matter Mater. Phys.* **67**(11), 1154081–1154088 (2003).

[19] Quochi, F., Andreev, A., Cordella, F., Orru, R., Mura, A., Bongiovanni, G., Hoppe, H., Sitter, H., and Sariciftci, N. S. *J. Lumin.* **112**, 321–324 April (2005).

[20] Singh, T., Hernandez-Sosa, G., Neugebauer, H., Andreev, A., Sitter, H., and Sariciftci, N. *Phys. Status Solidi B* **243**(13), 3329–3332 (2006).

[21] Yanagi, H., Ohara, T., and Morikawa, T. *Adv. Mater.* **13**(19), 1452–1455 (2001).

[22] Herman, M. A. and Sitter, H. *Molecular Beam Epitaxy*, volume 7 of *Springer Series in Materials Science*. Springer Verlag, Berlin-Heidelberg, (1989).

[23] Markov, I. V. *Crystal Growth for Beginners*. World Scientific, New Jersey, 2nd edition, (2003).

[24] Schreiber, F. *Phys. Status Solidi A* **201**(6), 1037–1054 (2004).

[25] Grünbaum, E. and Matthews, W. *Phys. Stat. Sol.* **9**, 731 (1965).

[26] Markov, I. and Stoyanov, S. *Contemp. Phys.* **28**, 267 (1987).

[27] Castellano, C. `http://pil.phys.uniroma1.it/twiki/pub/Pil/IrregularSurfaces/mbe.gif`, Aug (2007).

[28] Michely, T. and Krug, J. *Islands, Mounds and Atoms*, volume 42 of *Springer Series in Surface Science*. Springer-Verlag, Berlin, Heidelberg, (2004).

[29] Aleksandrov, L. N. *Growth of crystalline semiconductor materials on crystal surfaces*. North-Holland Publishing Co, Amsterdam, (1984).

[30] Gilmer, G. *Nucl. Metall* **20**(pt 2), 964–977 (1976).

[31] Patrykiejew, A. and Binder, K. *Surf. Sci.* **273**(3), 413–426 (1992).

[32] Teichert, C., Ammer, C., and Klaua, M. *Phys. Status Solidi A* **146**(1), 223–242 (1994).

[33] Venables, J., Spiller, G., and Hanbücken, M. *Rep. Prog. Phys.* **47**, 399 (1984).

[34] Krug, J., Politi, P., and Michely, T. *Phys. Rev. B: Condens. Matter Mater. Phys.* **61**(20), 14037–14046 (2000).

[35] Tersoff, J., Denier Van Der Gon, A., and Tromp, R. *Phys. Rev. Lett.* **72**(2), 266–269 (1994).

[36] Erhrlich, G. and Hudda, F. G. *J. Chem. Phys.* **44**, 1039 (1966).

[37] Seah, M. P. *Surf. Sci.* **32**, 703 (1972).

[38] Meinel, K., Klaua, M., and Bethge, H. *J. Cryst. Growth* **89**(4), 447–458 July (1988).

[39] Elkinani, I. and Villain, J. *Journal de Physique I* **4(6)**, 949–73 (1994).

[40] Elkinani, I. and Villain, J. *Solid State Commun* **87(2)**, 105–8 (1993).

[41] Krug, J. *Journal of Statistical Physics* **87**(3-4), 505–518 (1997).

[42] Kalff, M., Šmilauer, P., Comsa, G., and Michely, T. *Surf. Sci.* **426**(3), L447–L453 (1999).

[43] Kürpick, U. and Rahman, T. *Phys. Rev. B: Condens. Matter Mater. Phys.* **57**(4), 2482–2492 (1998).

[44] Kalff, M., Comsa, G., and Michely, T. *Phys. Rev. Lett.* **81**(6), 1255–1258 (1998).

[45] Guha, S., Graupner, W., Resel, R., Chandrasekhar, M., Chandrasekhar, H. R., Glaser, R., and Leising, G. *Phys. Rev. Let.* **82**(18), 3625–3628 (1999).

[46] Resel, R., Koch, N., Meghdadi, F., Leising, G., Unzog, W., and Reichmann, K. *Thin Solid Films* **305**(1-2), 232–242 (1997).

[47] Andreev, A., Matt, G., Brabec, C. J., Sitter, H., Badt, D., Seyringer, H., and Sariciftci, N. S. *Adv. Mater.* **12**, 629–633 (2000).

[48] Plank, H., Resel, R., Sitter, H., Andreev, A., Sariciftci, N., Hlawacek, G., Teichert, C., Thierry, A., and Lotz, B. *Thin Solid Films* **443**(1-2), 108–114 (2003).

[49] Quochi, F., Cordella, F., Orrù, R., Communal, J., Verzeroli, P., Mura, A., Bongiovanni, G., Andreev, A., Sitter, H., and Sariciftci, N. *Appl. Phys. Lett.* **84**(22), 4454–4456 (2004).

[50] Resel, R. *Thin Solid Films* **433**, 1–11 (2003).

[51] France, C. B. and Parkinson, B. A. *Appl. Phys. Lett.* **82**(8), 1194–1196 (2003).

[52] Müllegger, S. and Winkler, A. *Surf. Sci.* **600**, 1290–1299 March (2006).

[53] Müllegger, S., Hlawacek, G., Haber, T., Frank, P., Teichert, C., Resel, R., and Winkler, A. *Appl. Phys. A: Mater. Sci. Process.* **87**(1), 103–111 (2007).

[54] Oji, H., Ito, E., Furuta, M., Kajikawa, K., Ishii, H., Ouchi, Y., and Seki, K. *J. Electron Spectrosc. Relat. Phenom.* **101-103**, 517–521 (1999).

[55] Hlawacek, G., Teichert, C., Andreev, A., Sitter, H., Berkebile, S., Koller, G., Ramsey, M., and Resel, R. *Phys. Status Solidi A* **202**(12), 2376–2385 (2005).

[56] Koller, G., Berkebile, S., Krenn, J., Tzvetkov, G., Hlawacek, G., Lengyel, O., Netzer, F., Teichert, C., Resel, R., and Ramsey, M. *Adv. Mater.* **16**(23-24), 2159–2162 (2004).

[57] Ivanco, J., Winter, B., Netzer, F., Ramsey, M., Gregoratti, L., and Kiskinova, M. *Appl. Phys. Lett.* **85**(4), 585–587 (2004).

[58] Koch, N., Yu, L.-M., Parentè, V., Lazzaroni, R., Johnson, R., Leising, G., Pireaux, J.-J., and Brèdas, J.-L. *Synth. Met.* **101**(1-3), 438–439 (1999).

[59] Winter, B., Ivanco, J., Netzer, F. P., Ramsey, M. G., Salzmann, I., and Resel, R. *Langmuir* **20**, 7512–7516 (2004).

[60] Müller, B., Kuhlmann, T., Lischka, K., Schwer, H., Resel, R., and Leising, G. *Surf. Sci.* **418**, 256–266 (1998).

[61] Resel, R., Erlacher, K., Müller, B., Thierry, A., Lotz, B., Kuhlmann, T., Lischka, K., and Leising, G. *Surf. Interface Anal.* **30**(1), 518–521 (2000).

[62] Schürmann, H., Koch, N., Vollmer, A., Schrader, S., and Neumann, M. *Synth. Met.* **111**, 591–594 (2000).

[63] Diebold, U. *Surf. Sci. Rep.* **48**, 53–229 (2003).

[64] Rodriguez, J. `http://www.chemistry.bnl.gov/SciandTech/CRS/researchhighlihts.htm`, Oct. (2007).

[65] Odelius, M., Bernasconi, M., and Parrinello, M. *Phys. Rev. Lett.* **78**(14), 2855–2858 (1997).

[66] Plank, H., Resel, R., Andreev, A., Sariciftci, N. S., and Sitter, H. *J. Cryst. Growth* **237-239**, 2076–2081 (2002).

[67] Bethge, H. In *Kinetics of Ordering and Growth at Surfaces,* Lagally, M., editor, 125–144. Plenum (1990).

[68] Campbell, P. A., Sinnamon, L. J., Thompson, C. E., and Walmsley, D. G. *Surf. Sci.* **410**(2-3), L768–L772 (1998).

[69] Frank, P., Hlawacek, G., Lengyel, O., Satka, A., Teichert, C., Resel, R., and Winkler, A. *Surf. Sci.* **601**(10), 2152–2160 May (2007).

[70] Facsko, S., Dekorsy, T., Koerdt, C., Trappe, C., Kurz, H., Vogt, A., and Hartnagel, H. *Science* **285**(5433), 1551–1553 (1999).

[71] Buzio, R., Toma, A., Chincarini, A., de Mongeot, F. B., Boragno, C., and Valbusa, U. *Surf. Sci.* **601**(13), 2735–2739 July (2007).

[72] Teichert, C. *Phys. Rep.* **365**, 335–432 (2002).

[73] Barth, J., Brune, H., Ertl, G., and Behm, R. *Phys. Rev. B: Condens. Matter Mater. Phys.* **42**(15), 9307–9318 (1990).

[74] Carter, C. B. and Hwang, R. Q. *Phys. Rev. B* **51**(7), 4730–4733 (1995).

[75] Kowalczyk, P., Kozlowski, W., Klusek, Z., Olejniczak, W., and Datta, P. *Appl. Surf. Sci.* **253**(10), 4715–4720 (2007).

[76] France, C., Schroeder, P., Forsythe, J., and Parkinson, B. *Langmuir* **19**(4), 1274–1281 (2003).

[77] Mannsfeld, S., Toerker, M., Schmitz-Hübsch, T., Sellam, F., Fritz, T., and Leo, K. *Org. Elec.* **2**(3-4), 121–134 (2001).

[78] Haber, T., Muellegger, S., Winkler, A., and Resel, R. *Phys. Rev. B: Condens. Matter Mater. Phys.* **74**(4), 045419 (2006).

[79] Fritz, S. E., Kelley, T. W., and Frisbie, C. D. *J. Phys. Chem. B* **109**(21), 10574–10577 Jun (2005).

[80] Lopez-Otero, A. *Thin Solid Films* **49**(1), 3–57 (1978).

[81] Stifter, D. and Sitter, H. *J. Cryst. Growth* **156**(1-2), 79–85 (1995).

[82] Andreev, A., Sitter, H., Sariciftci, N. S., Brabec, C. J., Springholz, G., Hinterhofer, P., Plank, H., Resel, R., Thierry, A., and Lotz, B. *Thin Solid Films* **403-404**, 444–448 (2002).

[83] Binnig, G., Quate, C., and Gerber, C. *Phys. Rev. Lett.* **56(9)**, 930–3 (1986).

[84] Binnig, G., Gerber, C., Stoll, E., Albrecht, T., and Quate, C. *Surf. Sci.* **189-190**, 1–6 (1987).

[85] Devinci, L. http://perso.wanadoo.fr/nanotechnologie/Chapitres/ Microscopes/Page Microscopes.htm.

[86] Mate, C. M., McClelland, G. M., Erlandsson, R., and Chiang, S. *Phys. Rev. Lett.* **59**, 1942–1945 (1987).

[87] Meyer, G. and Amer, N. M. *Appl. Phys. Lett.* **57**, 2089–2091 (1990).

[88] Alexeev, A. M. Technical report, NT-MDT, (2002).

[89] Prater, C. B., Maivald, P. G., Kjoller, K. J., and Heaton, M. G. Application Note AN04, Veeco, (2004).

[90] Magonov, S. N., Elings, V., and Whangbo, M. H. *Surf. Sci.* **375**, L385–L391 (1997).

[91] Wallner, G., Resch, K., Hlawacek, G., Teichert, C., Maier, G., Binder, W., and Gahleitner, M. In *Annual Technical Conference - ANTEC, Conference Proceedings*, volume 1, 1096–1100 (Society of Plastics Engineers, Borealis GmbH, Linz, Austria, 2004).

[92] Fujii, T., Suzuki, M., Miyashita, M., Yamaguchi, M., Onuki, T., Nakamura, H., Matsubara, T., Yamada, H., and Nakayama, M. *J. Vac. Sci. Technol. B* **9**, 666–669 (1991).

[93] Zhao, Y., Wang, G.-C., and Lu, T.-M. *Characterization of amorphous and crystalline rough surface: principles and applications*, volume 37 of *Experimental methodes in the physical sciences*. Academic Press, New York, (2001).

[94] Sinha, S. K., Sirota, E. B., Garoff, S., and Stanley, H. B. *Phys. Rev. B* **38**(4), 2297–2311 (1988).

[95] Zhao, Y.-P., Yang, H.-N., Wang, G.-C., and Lu, T.-M. *Phys. Rev. B: Condens. Matter Mater. Phys.* **57**(3), 1922–1934 (1998).

[96] Malpica, N., De Solórzano, C., Vaquero, J., Santos, A., Vallcorba, I., García-Sagredo, J., and Del Pozo, F. *Cytometry* **28**(4), 289–297 (1997).

[97] Klapetek, P., Oblidal, I., Franta, D., Montaigne-Ramil, A., Bonanni, A., Stifter, D., and Sitter, H. *Acta Physica Slovaca* **53**(3), 223–230 (2003).

[98] Klapetek, P., Necas, D., and Anderson, C. *Gwyddion user guide*, June (2008).

[99] Smilgies, D., Blasini, D., Hotta, S., and Yanagi, H. *J. Synch. Rad.* **12**, 807–811 (2005).

[100] Telieps, W. and Bauer, E. *Ultramicroscopy* **17**(1), 57–65 (1985).

[101] Bauer, E. *Surf. Rev. Lett.* **5**(6), 1275–1286 (1998).

[102] Telieps, W. and Bauer, E. *Surf. Sci.* **162**(1-3), 163–168 October (1985).

[103] Altman, M., Chung, W., and Liu, C. *Surf. Rev. Lett.* **5**(6), 1129–1141 (1998).

[104] Bethge, H. and Klaua, M. *Ultramicroscopy* **11**(2-3), 207–214 (1983).

[105] Rotermund, H., Nettesheim, S., von Oertzen, A., and Ertl, G. *Surf. Sci.* **275**(1-2), L645–L649 (1992).

[106] Bethge, H., Krajewski, T., and Lichtenberger, O. *Ultramicroscopy* **17**(1), 21–30 (1984).

[107] Meyer zu Heringdorf, F.-J., Reuter, M., and Tromp, R. *Appl. Phys. A* **78**, 787–791 (2004).

[108] Berkebile, S., Koller, G., Hlawacek, G., Teichert, C., Netzer, F. P., and Ramsey, M. G. *Surf. Sci.* **600**(24), L313–L317 December (2006).

[109] Andreev, A., Montaigne, A., Hlawacek, G., Sitter, H., and Teichert, C. *J. Vac. Sci. Technol., A* **24**(4), 1660–1663 (2006).

[110] Resel, R., Oehzelt, M., Lengyel, O., Haber, T., Schülli, T., Thierry, A., Hlawacek, G., Teichert, C., Berkebile, S., Koller, G., and Ramsey, M. *Surf. Sci.* **600**(19), 4645–4649 (2006).

[111] Knüfing, L., Schollmeyer, H., Riegler, H., and Mecke, K. *Langmuir* **21**(3), 992–1000 (2005).

[112] Ebner, C., Park, K.-B., Nielsen, J.-F., and Pelz, J. *Phys. Rev. B* **68**, 245404 (2003).

[113] Mo, Y.-W., Kleiner, J., Webb, M., and Lagally, M. *Surf. Sci.* **268**, 275 (1992).

[114] Hlawacek, G. Master's thesis, Institute of Physics, University of Leoben, Leoben, Austria, (2003).

[115] Teichert, C., Hlawacek, G., Andreev, A. Y., Sitter, H., Frank, P., Winkler, A., and Sariciftci, N. S. *Appl. Phys. A: Mater. Sci. Process.* **82**, 665–669 (2006).

[116] Shchukin, V. A. and Bimberg, D. *Rev. Mod. Phys.* **71**, 1125 (1999).

[117] Hlawacek, G., Shen, Q., Teichert, C., Resel, R., and Smilgies, D. M. *Surf. Sci.* **601**, 2584 (2007).

[118] Poppa, H. and Elliot, A. G. *Surf. Sci.* **24**(1), 149–163 January (1971).

[119] Balzer, F., Kankate, L., Niehus, H., and Rubahn, H.-G. In *Proceedings of SPIE - The International Society for Optical Engineering*, volume 5724, 285–294 (Fysisk Institut, Syddansk Universitet, Odense, Denmark, 2005).

[120] Kadashchuk, A., Andreev, A., Sitter, H., Sariciftci, N., Skryshevski, Y., Piryatinski, Y., Blonsky, I., and Meissner, D. *Adv. Funct. Mater.* **14**(10), 970–978 (2004).

[121] Andreev, A., Sitter, H., Brabec, C., Hinterdorfer, P., Springholz, G., and Sari-ciftci, N. *Synth. Met.* **121**(1-3), 1379–1380 (2001).

[122] Grimshaw, R. W., Sadler, A. G., and Roberts, A. L. *Clay Minerals Bulletin* **5**(28), 110–127 (1962).

[123] Taboadela, M. M. and Ferrandis, V. A. In *The differential thermal investigation of clays*, Mackenzie, R. C., editor, chapter 6, 165–190. Mineralogical Society (1957). fig. VI, 3.

[124] Roy, R. *J. Am. Ceram. Soc.* **32**(6), 202–209 June (1949).

[125] Haber, T., Oehzelt, M., Resel, R., Andreev, A., Thierry, A., Sitter, H., Smilgies, D. M., Schaffer, B., Grogger, W., and Resel et, a. *J. Nanosci. Nanotechnol.* **6**, 698–703 March (2006).

[126] Michely, T., Kalff, M., Krug, J., and Politi, P. *Physikalische Blätter* **55**(11), 53–56 (1999).

[127] Evans, J., Sanders, D., Thiel, P., and DePristo, A. *Phys. Rev. B* **41**(8), 5410–5413 (1990).

[128] Wang, S. C. and Ehrlich, G. *Phys. Rev. Lett.* **67**, 2509 (1991).

[129] Schwoebel, R. J. and Shipsey, E. J. *J. Appl. Phys.* **37**, 3682 (1966).

[130] Schinzer, S., Sokolowski, M., Biehl, M., and Kinzel, W. *Phys. Rev. B: Condens. Matter Mater. Phys.* **60**(4), 2893–2899 (1999).

[131] Koller, G., Surnev, S., Ramsey, M., and Netzer, F. *Surf. Sci.* **559**(2-3), L187 (2004).

[132] Brenner, D. W., Shenderova, O. A., Harrison, J. A., Stuart, S. J., Ni, B., and Sinnot, S. B. *J. Phys.: Condens. Matter* **14**, 783 (2002).

[133] Lenand-Jones, L. E. *Proc. R. Soc. London* **106**(441), 463 (1924).

[134] Yamane, H., Yabuuchi, Y., Fukagawa, H., Kera, S., Okudaira, K. K., and Ueno, N. *J. Appl. Phys.* **99**(9), 093705 (2006).

[135] Okudaira, K. K., Hasegawa, S., Ishii, H., Seki, K., Harada, Y., and Ueno, N. *J. Appl. Phys.* **85**(9), 6453–6461 (1999).

[136] Bouchoms, I. P. M., Schoonveld, W. A., Vrijmoeth, J., and Klapwijk, T. M. *Synth. Met.* **104**(3), 175–178 July (1999).

[137] Drummy, L. and Martin, D. *Adv. Mater.* **17**(7), 903–907 (2005).

[138] Campione, M., Moret, M., and Sassella, A. In *9th European Conference on Surface Crystallography and Dynamics* (Vienna University of Technology, Vienna, 2007).

[139] Hlawacek, G., Teichert, C., Müllegger, S., Resel, R., and Winkler, A. *Synth. Met.* **146**(3), 383–386 (2004).

[140] Müllegger, S., Salzmann, I., Resel, R., Hlawacek, G., Teichert, C., and Winkler, A. *J. Chem. Phys.* **121**, 2272–2277 (2004).

[141] Resel, R., Oehzelt, M., Haber, T., Hlawacek, G., Teichert, C., Müllegger, S., and Winkler, A. *J. Cryst. Growth* **283**(3-4), 397–403 (2005).

[142] Balzer, F., Kintzel Jr., E., Skofronick, J., Safron, S., and Rubahn, H.-G. In *Proceedings of SPIE - The International Society for Optical Engineering*, volume 4800, 216–222 (, Fysisk Institut, Syddansk Universitet, DK-5230 Odense M, Denmark, 2002).

[143] Sun, L., Hohage, M., Zeppenfeld, P., Berkebile, S., Koller, G., Netzer, F., and Ramsey, M. *Appl. Phys. Lett.* **88**(12), 121913 (2006).

[144] Frank, P., Hernandez-Sosa, G., Sitter, H., and Winkler, A. *Thin Solid Films* (2007). accepted.

[145] Casalis, L., Danisman, M., Nickel, B., Bracco, G., Toccoli, T., Iannotta, S., and Scoles, G. *Phys. Rev. Lett.* **90**(20), 2061011–2061014 (2003).

Acknowledgments